MAGNETISM OF THE DILUTE URANIUM COMPOUND SYSTEM $(U_xLa_{1-x})Ru_2Si_2$

by
Kazuhiro MARUMOTO

DISSERTATION IN PHYSICS

OSAKA UNIVERSITY
GRADUATE SCHOOL OF SCIENCE
TOYONAKA OSAKA

JANUARY 1997

Magnetism of the Dilute Uranium Compound System $(U_xLa_{1-x})Ru_2Si_2$

Kazuhiro Marumoto

Magnetism of the Dilute Uranium Compound System $(U_xLa_{1-x})Ru_2Si_2$

Kazuhiro Marumoto

Dissertation in Physics

Osaka University
Graduate School of Science
Toyonaka Osaka

January 1997

Referees : Prof. Y. Miyako
Prof. Y. Ōnuki
Prof. S. Kawarazaki
Prof. S. Miyasita
Prof. K. Kindo

The fear of the Lord is the beginning of wisdom;
a good understanding have all those who practice it.
His praise endures for ever! *Psalms 111:10*

Contents

Abstract 7

1 Introduction 11

2 Physical properties of the strongly correlated electron systems 15
2.1 Kondo-impurity system 15
2.2 Heavy-fermion system 16

3 Structural and magnetic properties of the heavy-fermion compounds 21
3.1 URu_2Si_2 21
3.2 $CeRu_2Si_2$ 27
3.3 $U(Ru_{1-x}Rh_x)_2Si_2$ and $Ce(Ru_{1-x}Rh_x)_2Si_2$ 31

4 Experimental procedures 37
4.1 Sample preparation 37
4.2 Magnetic-susceptibility measurement 39
4.3 Magnetization measurement 41
4.4 Specific-heat measurement 43
4.5 Electrical-resistivity measurement 44
4.6 Hall-effect measurement 44

5 Magnetism of the dilute uranium compound system $(U_xLa_{1-x})Ru_2Si_2$ 51
5.1 Introduction 51
5.2 Experimental results 52
5.2.1 Magnetic susceptibility 52
5.2.2 Magnetization 55
5.2.3 Specific heat 57
5.2.4 Electrical resistivity 61
5.3 Analysis and discussion 63
5.3.1 Crystalline-electric-field splitting 63
5.3.2 Crystalline-electric-field model 67
5.3.3 Kondo model 70
5.4 Conclusion 76

6 Comparative study with the dilute cerium compound system $(Ce_xLa_{1-x})Ru_2Si_2$ 79
6.1 Introduction 79
6.2 Experimental results 79
6.2.1 Magnetic susceptibility 79
6.2.2 Magnetization 83
6.2.3 Specific heat 84

6.3 Analysis and discussion 87
6.4 Conclusion 92

7 Comparative study with the dilute praseodymium compound system $(Pr_xLa_{1-x})Ru_2Si_2$ 95
7.1 Introduction 95
7.2 Experimental results 95
7.2.1 Magnetic susceptibility 95
7.2.2 Magnetization 97
7.2.3 Specific heat 99
7.3 Analysis and discussion 101
7.4 Conclusion 103

8 Transport properties of the lattice uranium compound system $U(Ru_{1-x}Rh_x)_2Si_2$ 107
8.1 Introduction 107
8.2 Experimental results 107
8.2.1 Electrical resistivity 107
8.2.2 Hall effect 110
8.3 Analysis and discussion 111
8.3.1 Electrical resistivity 111
8.3.2 Hall effect 114
8.4 Conclusion 116

Published works 119

Acknowledgments 120

Abstract

URu_2Si_2 is known as one of the most interesting heavy-fermion compounds. The magnetism of URu_2Si_2, however, has not yet been understood completely. One of the complications for understanding the magnetism of URu_2Si_2 is the competition between the Kondo effect and the Ruderman-Kittel-Kasuya-Yosida (RKKY) interaction. In order to clarify this situation experimentally and to understand the role of the uranium crystalline field, we have carried out the magnetic, thermodynamical, and transport measurements on the dilute uranium compound system $(U_xLa_{1-x})Ru_2Si_2$ ($x \leq 0.15$). The experimental data of the magnetic susceptibility and magnetization show a large uniaxial magnetic anisotropy and the single-site screening of the magnetic moment at low temperatures. The specific-heat data show an enhanced γ value of 130 ± 20 mJ/K^2 U mol and a Schottky anomaly at around 25 K. The electrical-resistivity data show a positive T^2 dependence at low temperatures and an increase behavior as temperature increases. We have analyzed the magnetic, thermodynamical, and transport properties by the crystalline-electric-field (CEF) and Kondo models. In the high-temperature region above 100 K, the CEF model is a good picture. It can explain the large uniaxial magnetic anisotropy and the temperature dependence of the susceptibility at high temperatures. The CEF scheme is the non-Kramers doublet ground state and the singlet first excited state with the CEF splitting of 60 ± 6 K. This CEF splitting is determined by the Schottky anomaly in the specific heat. However, the CEF model is not appropriate to explain the experimental data at low temperatures. The magnetic moment at low temperatures is largely suppressed from that calculated by the CEF model and the single-site screening of the magnetic moment can be explained by the Kondo model. The Kondo model shows a good agreement with the experimental data. The Kondo temperature is estimated to be 67 ± 10 K from the specific-heat data by using the $S = 1/2$ Kondo model. The good agreement with the Kondo model means that there is the single-site Kondo screening of the uranium atom and the Fermi-liquid state occurs at low temperatures. The γ value and Schottky anomaly are nearly the same as those observed for URu_2Si_2. From these results, it is suggested that the single-site Kondo screening is important for understanding the Fermi-liquid state in URu_2Si_2.

The measurements on the dilute cerium compound $(Ce_xLa_{1-x})Ru_2Si_2$ ($x \leq 0.10$) have been performed for the comparative study with the dilute uranium system $(U_xLa_{1-x})Ru_2Si_2$. It would be interesting to compare the single-site properties in $(Ce_xLa_{1-x})Ru_2Si_2$ with those in $(U_xLa_{1-x})Ru_2Si_2$ because both $CeRu_2Si_2$ and URu_2Si_2 compounds are heavy-fermion systems with different f electrons. The experimental data of the magnetic susceptibility

and magnetization show a large uniaxial magnetic anisotropy. The specific-heat data show an anomaly of the enhancement of the specific heat at low temperatures. We have analyzed the magnetic and thermodynamical properties by the CEF model. In the high-temperature region above 50 K, the CEF model shows a good agreement with the experimental data. The obtained CEF parameters agree fairly well with those for $CeRu_2Si_2$. However, the low-temperature behavior below about 20 K can not be explained by the CEF model. The magnetic moment is slightly suppressed from the CEF calculation and this may mean that there exist the Kondo screening or an antiferromagnetic correlation. If we analyze the low-temperature properties by the Kondo model, the Kondo temperature T_K of the dilute cerium system is estimated to be lower than 1 K. The change of T_K from 24.4 K of $CeRu_2Si_2$ may be caused by the volume change. From the comparison between the dilute uranium system $(U_xLa_{1-x})Ru_2Si_2$ and the dilute cerium system, it is suggested that the the Kondo temperature of the dilute uranium system, which CEF scheme is the non-Kramers doublet ground state and the singlet first excited state, is less influenced by the volume change than that of the dilute cerium system which CEF scheme is the Kramers doublet ground state.

The measurements on the dilute praseodymium system $(Pr_xLa_{1-x})Ru_2Si_2$ ($x \leq 0.10$) have been performed to compare the single-site properties with those of the dilute uranium system $(U_xLa_{1-x})Ru_2Si_2$. The ground J multiplets of the dilute uranium and praseodymium ions are considered to be the same and the comparison between the dilute praseodymium and uranium systems would be expected to show the difference of the nature between the $4f$ and $5f$ electrons. The study of the dilute praseodymium system would also show the influence of the difference of the f electron number in the dilute praseodymium and cerium systems. The experimental data of the magnetic susceptibility and magnetization show a large uniaxial magnetic anisotropy. The specific-heat data show a Schottky anomaly at around 8 K. We have analyzed the magnetic and thermodynamical properties by the CEF model. The experimental data in the whole measured temperature and magnetic field range are well explained by the singlet-singlet CEF model with the CEF splitting of 20 ± 1 K. This means that the dilute praseodymium system is described as the well localized f electron system. The comparison between the dilute uranium and praseodymium systems suggests that the non-Kramers doublet-singlet CEF splitting, not the singlet-singlet one, is necessary for the Kondo screening as observed for the dilute uranium system.

Rh-doped uranium compound system $U(Ru_{1-x}Rh_x)_2Si_2$ ($0 \leq x \leq 1$) have been studied extensively. The study of this system has indicated that the hybridization effect between the magnetic f and $4d$ conduction electrons is important to characterize the magnetism. However, the transport property of $U(Ru_{1-x}Rh_x)_2Si_2$ has not yet been studied sufficiently. In order to study this system from the viewpoint of the transport phenomenon, the electrical-resistivity and Hall-effect measurements have been performed on the $U(Ru_{1-x}Rh_x)_2Si_2$ ($x \leq 0.03$). The study of the Rh-doping effect to the transport property of $U(Ru_{1-x}Rh_x)_2Si_2$ would be expected to give more information about the phase transition of URu_2Si_2 at T_N. The experimental data of the electrical resistivity show a broad maximum at around 70 K. The anomaly of the resistivity at T_N is weakened as the

Rh concentration increases and seems to be disappeared at $x = 0.04 \sim 0.05$. The data of the Hall coefficient show a relative broad maximum at around 50 K. This maximum increases and shifts slightly to the lower temperature as the Rh concentration increases. The temperature dependence of the Hall coefficient above T_N and the Rh-concentration dependence of the relative broad maximum of the Hall coefficient are qualitatively understood by the extraordinary Hall coefficient derived by the previous studies. The jump in the Hall coefficient decreases dramatically as the Rh concentration increases. This experimental result suggests that the $4d$ bands of Ru or Rh contribute the nesting of the Fermi surface. The jump in the Hall coefficient is qualitatively understood by the change of the ordinary Hall coefficient. From the comparison of the anomaly of the Hall coefficient between Cr and $U(Ru_{1-x}Rh_x)_2Si_2$ at T_N, it is suggested that the nesting bands of $U(Ru_{1-x}Rh_x)_2Si_2$ are electron bands, not the electron and hole bands as in Cr.

Chapter 1

Introduction

The strongly interacting electron systems have been studied for these several decades. The magnetism of transition metals and the Mott transition of transition-metal oxides were studied as a new physics of the electronic correlation by using various experimental methods in 1960s. Effort by theoreticians prompted the development of theoretical treatments of the many-body problem of the electron gas and led to the success of the theory of the BCS-type superconductivity. After that, many studies have been performed on the systems with the electronic correlation, for example, the Kondo impurity system, the heavy-fermion system, and the high-T_c superconducting system. These are generally called as "the strongly correlated electron systems". The normal state of these systems are described by means of a Fermi liquid and these systems are known to have various physical topics.

Several uranium-based heavy-fermion systems have attracted a considerable attention because of their unconventional properties. Many experimental and theoretical studies have been done intensely to clarify the ground state of these systems. In these studies, URu_2Si_2 is one of the most interesting systems, because it exhibits the coexistence of a type-I antiferromagnetic order ($T_N = 17.5$ K) with an unusually small ordered moment ($\sim 0.04\mu_B$) and non-BCS-type superconductivity ($T_c = 1.2$ K) [1, 2, 3, 4]. Much experimental work has been done extensively to understand this system using various measurement techniques [5, 6, 7, 8, 9, 10, 11]. The mechanism of the phase transition at T_N, however, is still controversial. Moreover it has not yet been clarified whether the $5f$ electrons of this system are itinerant or localized. From the viewpoint of the itinerant-electron picture, the weak-antiferromagnetic ordering was ascribed to the formation of a spin-density wave (SDW) of itinerant heavy electrons [12, 13]. From the viewpoint of the localized-electron picture, the magnetic properties have been studied theoretically by the crystalline-electric-field (CEF) model with the singlet ground state [14, 15, 16]. For the phase transition at T_N, the contribution of the quadrupolar coupling between $5f$ electrons of the uranium atoms was suggested by the study of the nonlinear susceptibility [17, 18, 19]. However, it seems that a complete explanation for the experimental results has not yet been given.

One of the complications for understanding the magnetism of URu_2Si_2 is the competition between the Kondo effect and the Ruderman-Kittel-Kasuya-Yosida (RKKY) interaction [20, 21, 22]. In order to clarify this situation experimentally and to understand the role

of the uranium crystalline field, we have here carried out the magnetic measurements on the dilute uranium compound system $(U_xLa_{1-x})Ru_2Si_2$ ($x \leq 0.15$). The analysis of the single-site properties of the uranium atom is important to understand the relation between the heavy-fermion state and the Kondo effect in URu_2Si_2. After identifying the single-site properties on the dilute uranium system, this competition should be analyzed on the samples with more uranium concentration.

The measurements on the dilute cerium compound system $(Ce_xLa_{1-x})Ru_2Si_2$ ($x \leq 0.10$) and the dilute praseodymium compound system $(Pr_xLa_{1-x})Ru_2Si_2$ ($x \leq 0.10$) have been performed for the comparative study with the dilute uranium system $(U_xLa_{1-x})Ru_2Si_2$. $CeRu_2Si_2$ is the typical heavy-fermion system with $4f$ electron. Since the wave function of the $4f$ electron is generally more localized than that of the $5f$ electron, the comparative study between the $4f$ and $5f$ electrons is useful to understand the difference of the f electron character in the formation of the heavy-fermion state. For another comparative study, the influence of the difference of the f electron number is discussed by using the study of $(Pr_xLa_{1-x})Ru_2Si_2$ and $(Ce_xLa_{1-x})Ru_2Si_2$. As explained below in the text, the praseodymium ion in $(Pr_xLa_{1-x})Ru_2Si_2$ has two f electrons, which is the same number as the uranium ion in $(U_xLa_{1-x})Ru_2Si_2$. The dilute praseodymium system $(Pr_xLa_{1-x})Ru_2Si_2$ will be compared with the dilute uranium system using the same ground J multiplet. There is the difference of the f electron number in the dilute praseodymium and cerium systems and the study for the influence of the f electron number will be useful to consider the formation of the heavy-fermion state. The effects from the difference of the extension of wave function and the f electron number will be discussed with the comparison among these dilute f electron compounds.

Rh-doped uranium compound system $U(Ru_{1-x}Rh_x)_2Si_2$ ($0 \leq x \leq 1$) have been studied extensively [9, 17, 19, 20, 21, 23, 24, 25]. The study of this system has indicated that the hybridization effect between the magnetic f and $4d$ conduction electrons is important to characterize the magnetism. However, the transport property of $U(Ru_{1-x}Rh_x)_2Si_2$ has not yet been studied sufficiently. In order to study this system from the viewpoint of the transport phenomenon, the transport measurements have been performed on the heavy-fermion compound system $U(Ru_{1-x}Rh_x)_2Si_2$ ($x \leq 0.03$). The study of the Rh-doping effect to the transport property of $U(Ru_{1-x}Rh_x)_2Si_2$ would be expected to give more information about the phase transition of URu_2Si_2 at T_N.

Bibliography

[1] C. Broholm, J.K. Kjems, W.J.L. Buyers, P. Matthews, T.T.M. Palstra, A.A. Menovsky, and J.A. Mydosh, Phys. Rev. Lett. **58**, 1467 (1987).

[2] E.D. Isaacs, D.B. McWhan, R.N. Kleiman, D.J. Bishop, G.E. Ice, P. Zschack, B.D. Gaulin, T.E. Mason, J.D. Garrett, and W.J.L. Buyers, Phys. Rev. Lett. **65**, 3185 (1990).

[3] T.E. Mason, B.D. Gaulin, J.D. Garrett, Z. Tun, W.J.L. Buyers, and E.D. Isaacs, Phys. Rev. Lett. **65**, 3189 (1990).

[4] C. Broholm, H. Lin, P. Matthews, T.E. Mason, W.J.L. Buyers, M.F. Collins, A.A. Menovsky, J.A. Mydosh, and J.K. Kjems, Phys. Rev. B **43**, 12 809 (1991).

[5] T.T.M. Palstra, A.A. Menovsky, J.van den Berg, A.J. Dirkmaat, P.H. Kes, G.J. Nieuwenhuys, and J.A. Mydosh, Phys. Rev. Lett. **55**, 2727 (1985).

[6] T.T.M. Palstra, A.A. Menovsky, and J.A. Mydosh, Phys. Rev. B **33**, 6527 (1986).

[7] W. Schlabitz, J. Baumann, B. Pollit, U. Rauchschwalbe, H.M. Mayer, U. Ahlheim, and C.D. Bredl, Z. Phys. B **62**, 171 (1986).

[8] B. Renker, F. Gompf, E. Gering, P. Frings, H. Rietshel, R. Felten, F. Steglich, and G. Weber, Physica B **148**, 41 (1987).

[9] Y. Miyako, *Transport and Thermal Properties of f-Electron Systems* (Plenum, New York, 1993) p. 187.

[10] K. Sugiyama, H. Fuke, K. Kindo, K. Shimohata, A.A. Menovsky, J.A. Mydosh, and M. Date, J. Phys. Soc. Jpn. **59**, 3331 (1990).

[11] J. Schoenes, C. Schönenberger, J.J.M. Franse, and A.A. Menovsky, Phys. Rev. B **35**, 5375 (1987).

[12] M.B. Maple, J.W. Chen, Y. Dalichaouch, T. Kohara, C. Rossel, M.S. Torikachvili, M.W. McElfresh, and J.D. Thompson, Phys. Rev. Lett. **56**, 185 (1986).

[13] M.W. McElfrsh, J.D. Thompson, J.O. Willis, M.B. Maple, T. Kohara and M.S. Torikachvili, Phys. Rev. B **35**, 43 (1987).

[14] G.J. Nieuwenhuys, Phys. Rev. B **35**, 5260 (1987).

[15] R. Konno, Prog. Theor. Phys. **89**, 51 (1993).

[16] P. Santini and G. Amoretti, Phys. Rev. Lett. **73**, 1027 (1994).

[17] Y. Miyako, S. Kawarazaki, H. Amitsuka, C.C. Paulsen, and K. Hasselbach, J. Appl. Phys. **70**, 5791 (1991).

[18] A.P. Ramirez, P. Coleman, P. Chandra, E. Bruck, A.A. Menovsky, Z. Fisk, and E. Bucher, Phys. Rev. Lett. **68**, 2680 (1992).

[19] Y. Miyako, H. Amitsuka, S. Kunii, and T. Kasuya, Physica B **186-188**, 236 (1993).

[20] Y. Miyako, T. Kuwai, T. Taniguchi, S. Kawarazaki, H. Amitsuka, C.C. Paulsen, and T. Sakakibara, J. Magn. Magn. Mater. **108**, 190 (1992).

[21] Y. Miyako, H. Amitsuka, S. Kawarazaki, T. Taniguchi, and T. Sikama, *Physical Properties of Actinide and Rare Earth Compounds*, JJAP Series 8, (Jpn. J. Appl. Phys., Tokyo, 1993) p. 230.

[22] J.S. Schilling, Phys. Rev. B **33**, 1667 (1986).

[23] H. Amitsuka, K. Hyomi, T. Nishioka, Y. Miyako, and T. Suzuki, J. Magn. Magn. Mater. **76-77**, 168 (1988).

[24] H. Amitsuka, T. Sakakibara, and Y. Miyako, J. Magn. Magn. Mater. **90-91**, 517 (1990).

[25] S. Kawarazaki, T. Taniguchi, H. Iwabuchi, Y. Miyako, H. Amitsuka, and T. Sakakibara, Phys. Lett. A **160**, 103 (1991).

Chapter 2

Physical properties of the strongly correlated electron systems

Lanthanide (cerium, praseodymium, *etc.*) and actinide (uranium, *etc.*) have f electrons and the wave functions of the f electron are less extended compared to those of, for example, the d electron. Therefore, the wave functions of the f electron have less overlap on each other and the resulting narrow f electron bands make the role of the electron-electron interaction relatively more important in the uranium-based and cerium-based materials.

According to the Fermi-liquid theory, the Fermi-liquid state is derived from the Fermi-gas state by introducing the Coulomb interaction between the Fermi particles. There is the one-to-one correspondence between the Fermi-liquid state and the original Fermi-gas state. The Fermi-liquid state is described as a quasi-particle state which can be identified by the quantum numbers $\boldsymbol{k}$ (wave-number vector) and σ (spin) of the Fermi-gas state. The electronic interaction produces a self energy of the quasi particle and the self energy enhances the effective mass of the quasi particle.

As the examples of the strongly correlated electron systems, the Kondo-impurity system and the heavy-fermion system are explained here.

2.1 Kondo-impurity system

The materials which exhibit the Kondo effect are usually characterized by the $-\ln T$ dependence of their electrical resistivity and by the screening of the localized magnetic moment by conduction electrons in them. The Kondo effect takes place on a single site of the magnetic impurity. The d electron impurity in a noble metal is considered here to give the theoretical explanation of the Kondo effect.

Intra-atomic Coulomb interaction and the hybridization between conduction and magnetic electrons yield the s-d exchange interaction. This interaction is described by the following s-d exchange Hamiltonian

$$H_{s-d} = -2Jv \sum_i \delta(\boldsymbol{r}_i)(\boldsymbol{s}_i \cdot \boldsymbol{S}), \tag{2.1}$$

where J is the exchange interaction, $\boldsymbol{s}_i$ and $\boldsymbol{r}_i$ are the i-th conduction-electron spin vector and coordinates, $\boldsymbol{S}$ is the localized spin vector, and v is the volume per unit-lattice cell. (In the case of the f electron impurity, this interaction is called the s-f exchange interaction.) In order to explain the anomalous logarithmic increase in the resistivity, the scattering of conduction electrons by the magnetic impurity in a non-magnetic host was concerned. This was solved by the perturbation calculation using the s-d exchange interaction [1]. The resistivity can be written as

$$\rho_m = \rho_B \left\{ 1 + 2\frac{J\rho}{N} \ln \frac{kT}{D} \right\}, \tag{2.2}$$

where D is the half width of the conduction band, k is the Boltzmann's constant, ρ is the density of states of conduction electrons, N is the electron number, and ρ_B is the temperature-independent spin-disorder resistivity obtained by the first Born approximation. Equation (2.2) describes the minimum of the electrical resistivity and the logarithmic increase in ρ_m toward lower temperature.

The screening of the localized magnetic moment by conduction electrons takes place in the lower temperature region. As the temperature decreases, the localized spin forms a singlet state by coupling antiferromagnetically with the conduction electron spins, where the localized spin moment is canceled by the conduction electron spin moments. This singlet ground state shows a constant resistivity caused by the impurities, that is called the resistance of the unitarity limit. There is no diverging behavior as seen in the perturbation calculation using the doublet scheme of the localized spin. The binding energy of the singlet is

$$\Delta E = kT_K = D \exp\left[-\frac{N}{\rho |J|} \right], \tag{2.3}$$

where T_K is the Kondo temperature. The Kondo temperature is roughly corresponding to the temperature of the region where the conduction electrons start to screen the localized magnetic moment.

2.2 Heavy-fermion system

The "heavy-fermion system" represents the group of the materials with a large electronic-specific-heat coefficient γ. This coefficient appears in the expression of the specific heat of metal at low temperatures as follows.

$$C = \gamma\, T + \beta\, T^3 + \cdots, \tag{2.4}$$

where $\gamma\, T$ and $\beta\, T^3$ are the contributions of the conduction electron and the lattice to the specific heat, respectively. The value of γ is proportional to the effective mass in the free electron model. Therefore, a large γ value corresponds to a large mass enhancement. This is the reason why this system is called the heavy-fermion system. The heavy-fermion state is realized especially in the f electron compounds where the magnetic ions form a lattice. The lattice f electron system is considered here to explain the heavy-fermion system.

The theoretical explanation for the heavy-fermion system is as follows. The strongly localized f electrons and the conduction electrons in a wide energy band hybridize each other and form a quasi-particle energy band. The electronic correlation, such as the Coulomb repulsion between f electrons, narrows this coherent energy band formed by the hybridization. Such correlation enhances the self energy of the quasi particle, which contributes the enhancement of the electronic-specific-heat coefficient γ.

The physical properties of the heavy-fermion system are as follows. Typical heavy-fermion compounds have a very large electronic-specific-heat coefficient γ which is 100 to 1000 times larger than that of the free electron. The electrical resistivity of some of these compounds increases with decreasing temperature in a certain temperature region like in the Kondo-impurity system. Then the resistivity shows a broad maximum followed by a rapid decrease in the lower-temperature region. In the sufficiently low-temperature region, the resistivity behaves as

$$\rho = \rho_0 + AT^2, \tag{2.5}$$

where ρ_0 is the residual resistivity and A is the coefficient of the T^2 term which is proportional to γ^2. The value of the coefficient A is $10^4 \sim 10^6$ times larger than that of the ordinary metals.

The magnetic susceptibility of these compounds at high temperatures can often be described by the Curie-Weiss law, which indicates an existence of localized magnetic moments. At low temperatures, however, the magnetic susceptibility does not depend on the temperature and exhibits a large Pauli paramagnetism, which means a formation of the Fermi-liquid state. The f electrons in the ground state form the non-magnetic singlet state together with the surrounding f and conduction electrons.

First heavy-fermion compound $CeAl_3$ was found by Andres *et al.* in 1975 [2]. After that, the compounds showing an anomalously large γ value have been found one after another in rare-earth (Ce, Yb, *etc.*) and actinide (U) intermetallic compounds.

As an example of the heavy-fermion system, the cerium intermetallic compound $CeCu_6$ and the related compounds are explained here [3, 4]. $CeCu_6$ crystallizes in the orthorhombic structure and shows a large γ value of 1670 mJ/K^2 mol. Neither superconductivity nor magnetic order takes place down to 18 mK. At high temperatures, the magnetic resistivity behaves as in the Kondo impurity system as shown in Fig. 2.1. However, below about 10 K the resistivity drops rapidly. These features indicate the formation of the Kondo lattice, that is, the heavy-fermion state where the scatterings of conduction electrons by the f electrons are coherent. The resistivity follows a T^2 dependence below 0.1 K and the magnetic susceptibility shows an enhanced Pauli paramagnetism. Lanthanum (La) substitute effect to the cerium (Ce) site have also been studied using the compounds $Ce_xLa_{1-x}Cu_6$ ($0 \leq x \leq 1$). The consecutive change from the Kondo-impurity (incoherent) regime to the Kondo-lattice (coherent) regime is observed with increasing the cerium concentration as shown in Fig. 2.2.

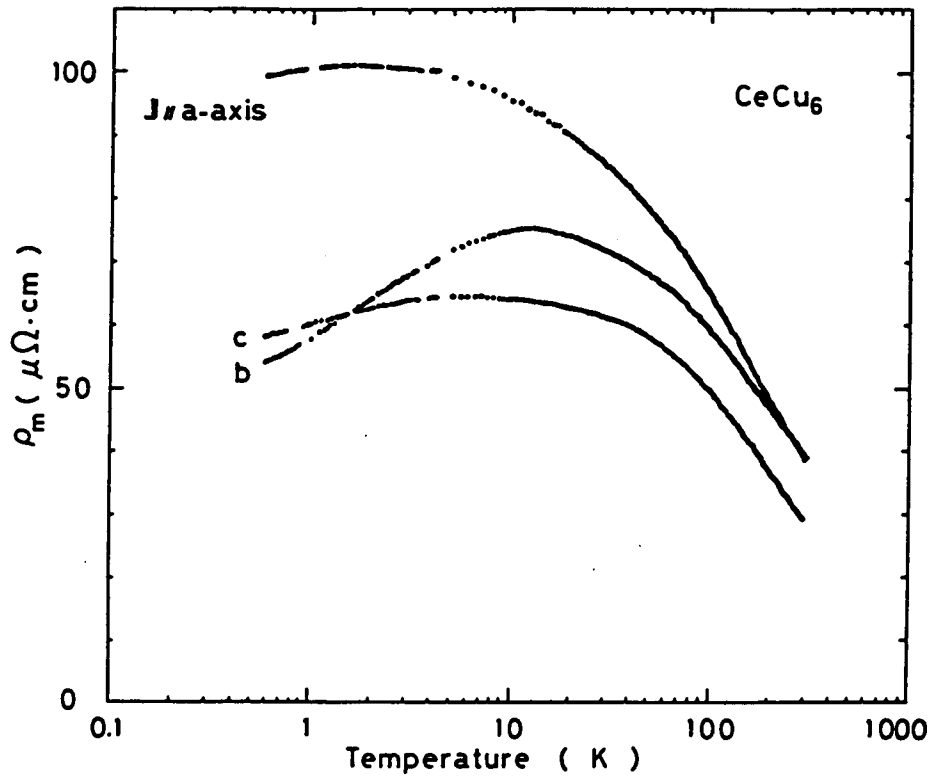

Figure 2.1: *Magnetic resistivity vs lnT in $CeCu_6$ [3].*

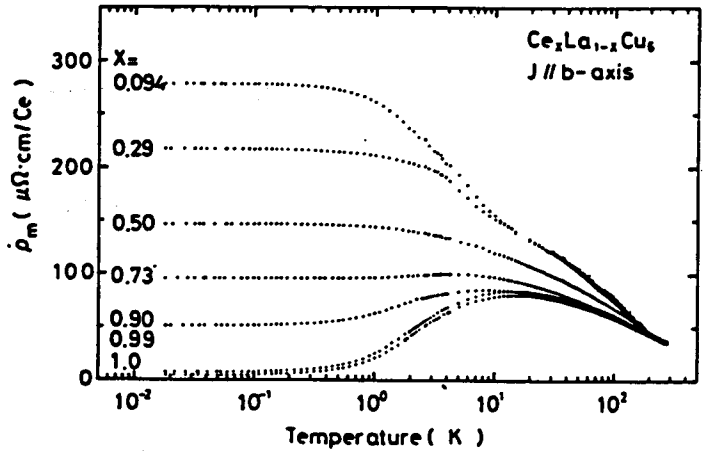

Figure 2.2: *Temperature dependence of the magnetic resistivity per molar cerium in $Ce_xLa_{1-x}Cu_6$ [4].*

Bibliography

[1] J. Kondo, Prog. Theor. Phys. **32**, 37 (1964).

[2] K. Anders, J.E. Graebner, and H.R. Ott, Phys. Rev. Lett. **35**, 1779 (1975).

[3] Y. Ōnuki, Y. Shimizu, and T. Komatsubara, J. Phys. Soc. Jpn. **54**, 304 (1985).

[4] A. Sumiyama, Y. Oda, H. Nagano, Y. Ōnuki, K. Shibutani, and T. Komatsubara, J. Phys. Soc. Jpn. **55**, 1294 (1986).

Chapter 3

Structural and magnetic properties of the heavy-fermion compounds

The structural and magnetic properties of the matrix compounds are shown in this chapter. These are surveyed to know the heavy-fermion system, which is useful to clear the purpose of this study.

3.1 URu_2Si_2

URu_2Si_2 crystallizes in the $ThCr_2Si_2$-type body-centered tetragonal structure (space group I4/mmm) shown in Fig. 3.1. The lattice parameters have been determined as a = 4.1288(88) and c = 9.5701(69) Å at room temperature [1]. As mentioned in the Introduction, this compound is one of the most interesting heavy-fermion system, because it exhibits the coexistence of a type-I antiferromagnetic order (T_N = 17.5 K) with an unusually small ordered moment ($\sim 0.04\mu_B$) and non-BCS-type superconductivity (T_c = 1.2 K).

The magnetic susceptibility of URu_2Si_2 shows a large magnetic anisotropy. The data along the c axis shows a broad maximum around 55 K, below which it decreases and then levels off to a large Pauli-paramagnetic behavior at still lower temperatures, while the data along the a axis is almost independent of the temperature (Fig. 3.2) [2]. The high-temperature data above 150 K along the c axis obeys the Curie-Weiss law with the effective moment $\mu_{eff} = 3.51\mu_B$ and the Curie-Weiss temperature $\Theta = -65$ K. The high-field magnetization measurements up to 60 T have been performed on single crystalline sample (Fig. 3.3) [3]. Three-step metamagnetic transitions have been observed along the c axis with the transition filed 35.8, 36.5, and 39.6 T at 1.3 K, while the magnetization along the a axis remains linear up to 50 T.

The electrical resistivity of URu_2Si_2 is very large and highly anisotropic at high temperatures (Fig. 3.4) [4]. The $d\rho/dT$ in a high-temperature region is negative and this behavior looks like the Kondo effect. The resistivity shows a broad maximum at 75 K and decreases as the temperature decreases. The resistivities along the both axes show a distinct Cr-like anomaly at T_N and a superconducting transition at T_c as shown in Fig. 3.5.

The neutron-scattering measurement of URu_2Si_2 confirmed the existence of an antiferromagnetic structure of small uranium moment of about $0.04\mu_B$ with (100) modulation wave vector, which is coexistent with the superconductivity as shown in Fig. 3.6 [5, 6, 7]. This result is also confirmed by x-ray-resonance magnetic scattering (Fig. 3.7) [8].

The specific heat of URu_2Si_2 shows a sharp anomaly caused by the phase transition at T_N [9, 10, 11]. Above T_N, the experimental data is described by the expression $C = \gamma T + \beta T^3$, with $\gamma = 112$ mJ/K^2 mol and $\beta = 0.382$ mJ/K^4 mol corresponding to a Debye temperature $\theta_D = 294$ K. The temperature dependence below T_N is described by a gap-type function of $\delta C = A\exp(-\Delta/T)$, with $A = 9890$ J/K mol and $\Delta = 129$ K (Fig. 3.8) [9]. The specific heat of the $5f$ electron is obtained by subtracting the lattice contribution which is assumed to be identical to the reference compound $ThRu_2Si_2$. It displays a broad peak with a maximum around 30 K, in addition to the anomaly at T_N (Fig. 3.9) [10]. The total entropy connected with both peaks is extrapolated to about $R\ln 2$, which suggests that the magnetic low-temperature state of URu_2Si_2 is formed by the localized $5f$ electrons, *i.e.*, in a crystal-field doublet ground state. The λ-like anomaly at T_N, which marks the onset of long-range antiferromagnetic order, is associated with an entropy change of only $0.15 \cdot R\ln 2$. A Schottky-type anomaly centered at $T \approx 32$ K can be fitted by a model calculation in terms of a transition between two crystal-field doublets splitted by 75 K (Fig.3.10) [11].

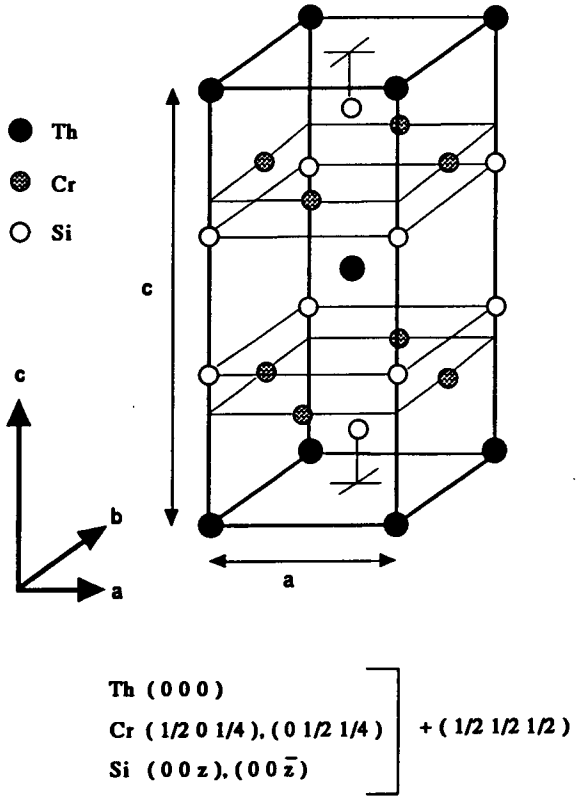

Figure 3.1: *Crystal structure of the $ThCr_2Si_2$-type.*

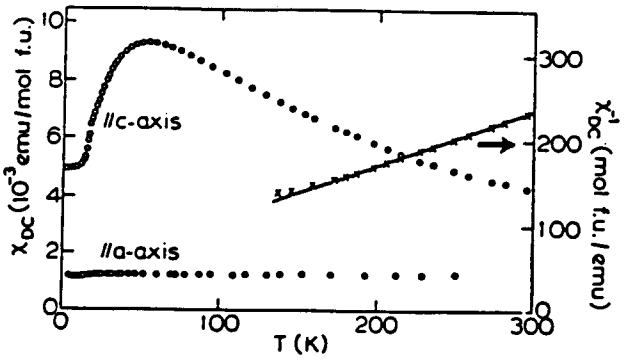

Figure 3.2: *dc susceptibility χ_{dc} and inverse susceptibility of URu_2Si_2, measured in a field of 2 T, parallel to the a and c axes. The crosses represent the inverse susceptibility along the c axis and yield $\Theta = -65$ K [2].*

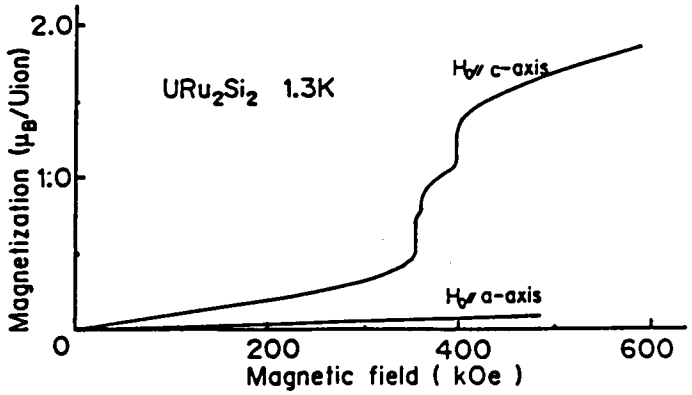

Figure 3.3: *Magnetization curves of URu_2Si_2 along the a and c axes at 1.3 K [3].*

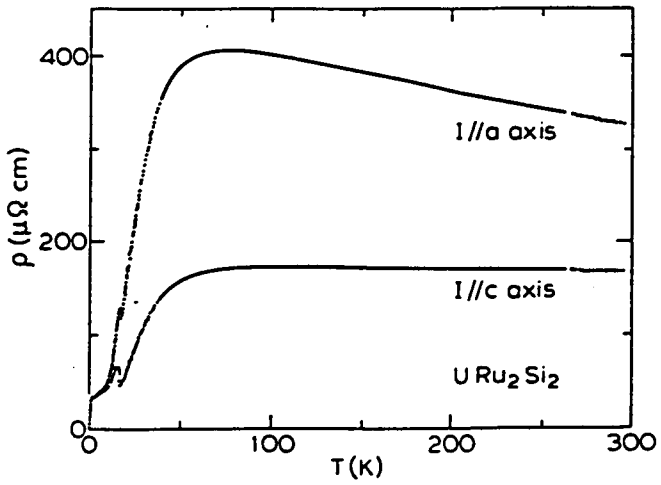

Figure 3.4: *Temperature dependence of the electrical resistivity of unannealed, single crystal URu_2Si_2 parallel to the a and c axes [4].*

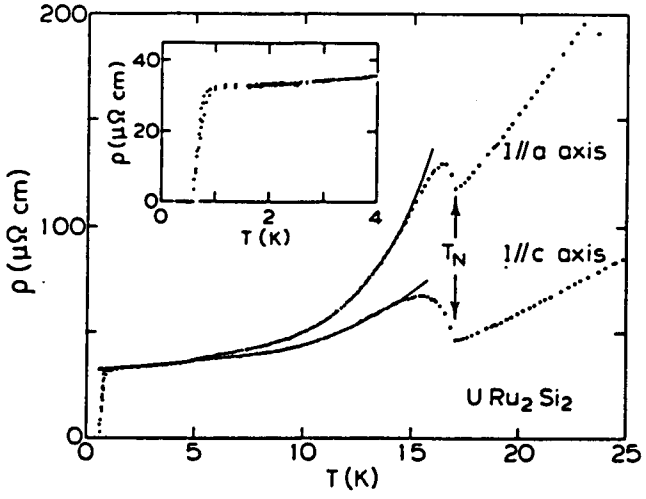

Figure 3.5: *Low-temperature resistivity of single-crystal URu_2Si_2 parallel to the a and c axes, showing the magnetic (T_N) and superconducting (T_c) phase transitions. The inset shows an enlargement of the superconducting phase transition [4].*

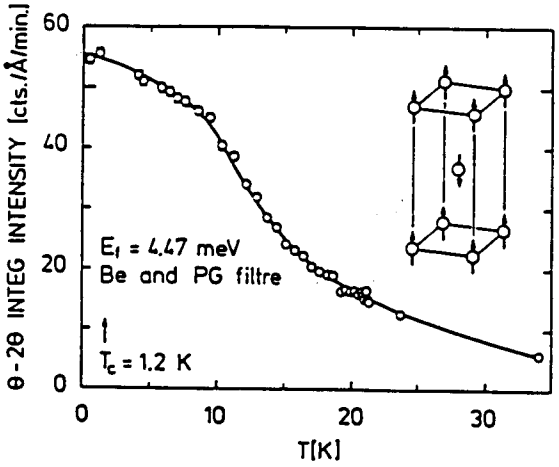

Figure 3.6: *Integrated elastic-magnetic Bragg scattering at (100) as a function of temperature, and the corresponding antiferromagnetic structure [5].*

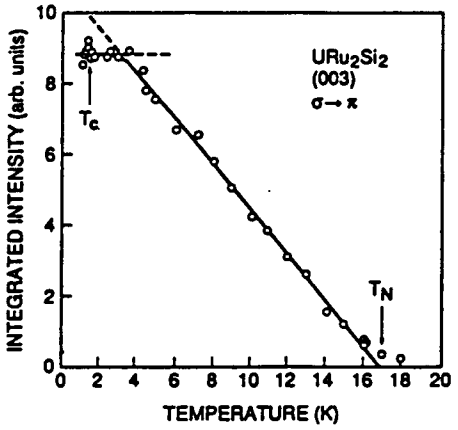

Figure 3.7: *Integrated intensity of the (003) magnetic Bragg reflection vs temperature. Notice the unusually broad linear regime, from T_N to $T_N/6$. The solid line is a guide to the eye. No change in the ordered moment is observed at the superconducting temperature T_c. Saturation corresponds to 8 counts/sec at the Bragg peak [8].*

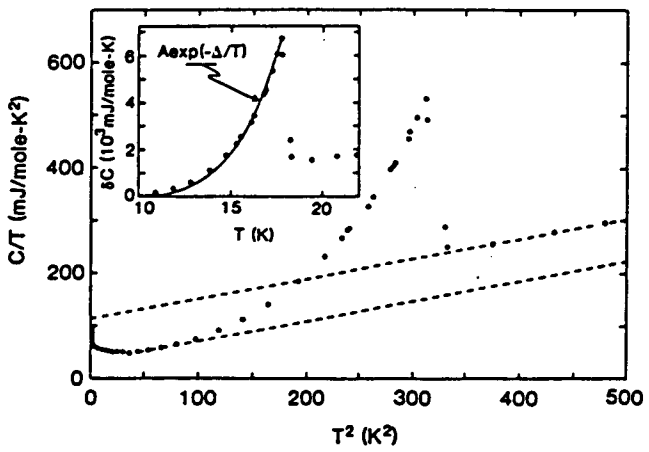

Figure 3.8: *Specific heat C divided by temperature T vs T^2 for URu_2Si_2 between 0.6 and 500 K^2. The meaning of the dashed lines is explained in the text. Inset : Estimated specific heat δC vs T associated with the apparent CDW or SDW transition at ~17.5 K. The solid line represents the function $A\,exp(-\Delta/T)$ with values for A and Δ given in the text [9].*

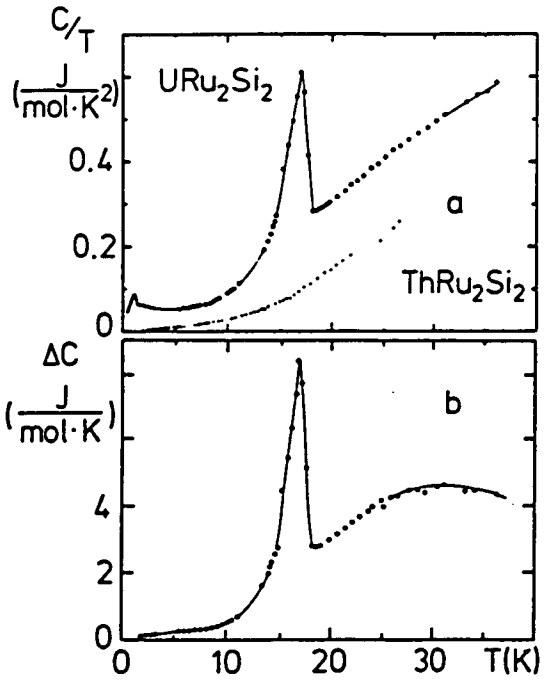

Figure 3.9: a *Specific heat of URu_2Si_2 and $ThRu_2Si_2$, plotted as C/T vs T for $T \leq 40$ K.* b $\Delta C = C(URu_2Si_2) - C(ThRu_2Si_2)$ *vs T [10].*

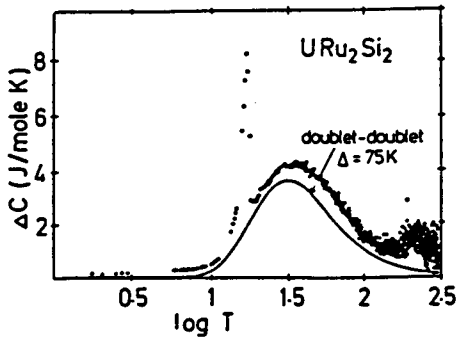

Figure 3.10: *Electronic specific heat $\Delta C(T)$ for URu_2Si_2 [11].*

3.2 $CeRu_2Si_2$

$CeRu_2Si_2$ crystallizes in the $ThCr_2Si_2$-type body-centered tetragonal structure (Fig. 3.1). This compound exhibits a large γ value ($\gamma = 385$ mJ/K^2 mol) characteristic to the heavy-fermion system. Neither long-range magnetic order nor superconductivity has been observed down to 20 mK [12, 13] except for the report of the magnetic ordering by the μSR measurement [14].

The temperature variation of the magnetic susceptibility shows a large magnetic anisotropy as seen in Fig. 3.11 [15]. Magnetization measurement on $CeRu_2Si_2$ single crystal shows a metamagnetic-like transition at the field of 7.9 T at low temperatures (Fig. 3.12) [15].

The magnetic specific heat of $CeRu_2Si_2$ shows two Schottky-like anomalies at around 11 and 84 K (Fig. 3.13) [16]. The lower-temperature anomaly is compared to the theoretical curve of the $S = 1/2$ Kondo model with the Kondo temperature $T_K = 24.4$ K. The specific-heat peak at 84 K is understood by a Schottky anomaly coming from the crystal-field splitting between the two doublet states with the energy gap of 220 K.

Electrical resistivity of $CeRu_2Si_2$ shows an anisotropy (Fig. 3.14) [17]. Lanthanum (La) substitute effect to the electrical resistivity is studied by using the compounds $Ce_{1-x}La_xRu_2Si_2$ ($0 \leq x \leq 1$) (Fig. 3.15) [18]. A Kondo behavior with a logarithmic slope is observed for $x \geq 0.3$.

Magnetic phase diagram of $Ce_{1-x}La_xRu_2Si_2$ ($0 \leq x \leq 1$) is obtained by the specific-heat, neutron-diffraction, and magnetic-susceptibility measurements (Fig. 3.16) [19]. It is reported that an antiferromagnetic order occurs for $0.08 \leq x \leq 0.90$.

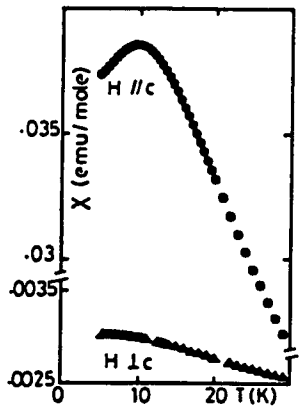

Figure 3.11: *Magnetic susceptibility of $CeRu_2Si_2$ parallel and perpendicular to the c axis at low temperatures. Note the difference in scale for the two axes [15].*

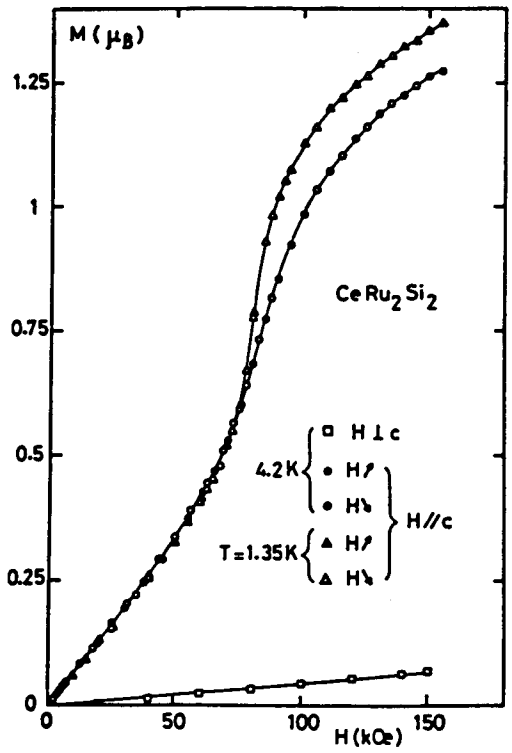

Figure 3.12: *Magnetization of $CeRu_2Si_2$ measured parallel and perpendicular to the c axis in increasing and decreasing field at 4.2 and 1.35 K [15].*

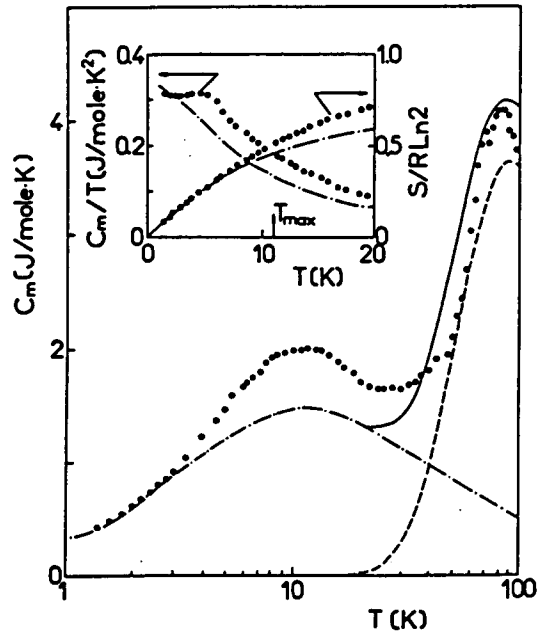

Figure 3.13: *Magnetic contribution to the specific heat of $CeRu_2Si_2$: C_m vs lnT. Inset : C_m/T and normalized entropy $S/R\,ln2$ vs T. Dash-dotted lines : theoretical value of the Kondo model (S = 1/2) for C(T), C(T)/T and S(T). Dashed line : calculated Schottky crystal field effect for a doublet-doublet splitting of 220 K. Full line : total calculated C(T) variation [16].*

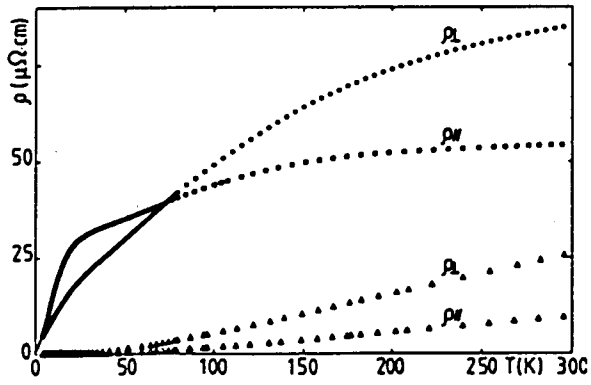

Figure 3.14: *Temperature dependence of the resistivities of $CeRu_2Si_2$ (o and •) and $LaRu_2Si_2$(△ and ▲) for the current parallel to the c axis ($\rho_\parallel$) or in the basal plane ($\rho_\perp$) [17].*

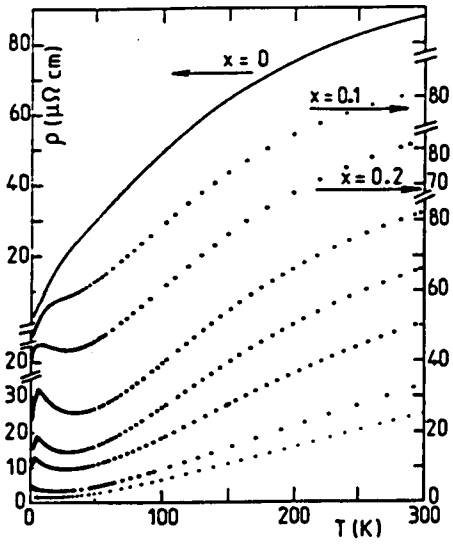

Figure 3.15: *Variations of the resistivity of $Ce_{1-x}La_xRu_2Si_2$ below 300 K. From top to bottom : x = 0, 0.1, 0.2, 0.3, 0.5, 0.7, 0.9, and 1 ($LaRu_2Si_2$). Notice the displacement of scales for the three upper curves [18].*

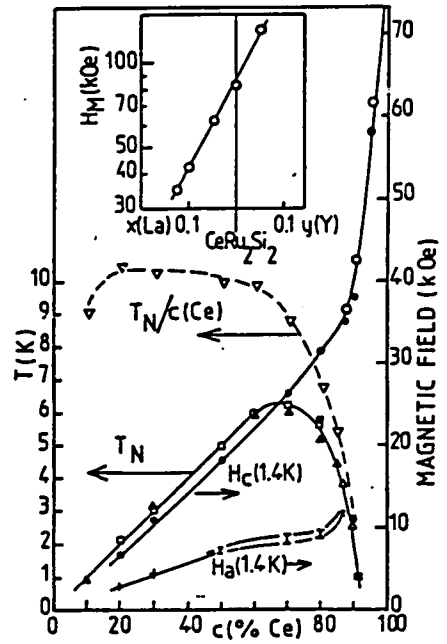

Figure 3.16: *Phase diagram of the $(La,Ce)Ru_2Si_2$ system. Main curves : variation of T_N deduced from the specific heat data (▲ and △) from neutron diffraction data (■) and from the χ_{ac} experiment data (□); variation of T_N/Ce concentration (▽ and dashed line); variation of H_c at 1.4 K (•) and H_M at 4.2 K (o) and of H_a at 1.4 K (+ and I). Insert : linear variation of $logH_M$ at 4.2 K vs small concentrations x of La and y of Y [19].*

3.3 $U(Ru_{1-x}Rh_x)_2Si_2$ and $Ce(Ru_{1-x}Rh_x)_2Si_2$

The systematic studies have been performed in the whole range of x in these systems. It has been found that these systems have several phases with different magnetic structures.

The magnetic phase diagram of $U(Ru_{1-x}Rh_x)_2Si_2$ ($0 \leq x \leq 1$) is shown in Fig. 3.17, which is obtained from the magnetic-susceptibility, magnetization, specific-heat, and neutron-scattering experiments [20, 21, 22, 23]. The region (I) indicates the phase of the heavy-fermion state with the coexistent of an antiferromagnetic order and a superconductivity. In the region (III), the susceptibility and specific heat exhibit a characteristic behavior of an antiferromagnetic transition of localized moments with wave vectors $(\frac{1}{2}, \frac{1}{2}, \frac{1}{2})$ below 47 K, and $(\frac{1}{2}, \frac{1}{2}, 0)$ and $(\frac{1}{2}, \frac{1}{2}, \frac{1}{2} \pm \frac{1}{6})$ below 42 K. The ordered state in the region (V) is characterized by the magnetic propagation vector $(0, 0, 1)$. In the boundaries (II) and (IV) where two different magnetic structures meet, the magnetic ordering seems to be suppressed with a competition of the different magnetic structures. The magnitude of the magnetic ordered moments in $U(Ru_{1-x}Rh_x)_2Si_2$ tends to increase with the Rh concentration x from $0.04\mu_B$ for x=0 to $2\mu_B$ for x=1. It is considered that the mixing between f and conduction electrons decreases with increasing x. These experiments suggest that the RKKY interaction plays an important role for the low-temperature magnetic properties in the Kondo-lattice system.

The magnetic phase diagram of $Ce(Ru_{1-x}Rh_x)_2Si_2$ ($0 \leq x \leq 1$) is composed of four regions as shown in Fig.3.18, which is obtained from the similar experiments performed on $U(Ru_{1-x}Rh_x)_2Si_2$ [24, 25]. The region (I) indicates the phase of the paramagnetic heavy-fermion state. The antiferromagnetic structure in the region (IV) is described by wave vectors $(\frac{1}{2}, \frac{1}{2}, 0)$ and $(\frac{1}{2}, \frac{1}{2}, \frac{1}{2})$. The study of the magnetic order in the region (II) indicates the spin-density wave of itinerant heavy electrons with the wave vector (0,0,0.42) for $x = 0.15$ [26, 27, 28, 29, 30].

As shown from these studies, when the Rh concentration increases, the heavy-fermion state is modified. In the more high Rh-concentration region, the localized f electron magnetic ordering occurs. The studies of these systems have indicated that the hybridization effect between the magnetic f and $4d$ conduction electrons is important to characterize the magnetism, because Rh has one more $4d$ electron than Ru. It has been found that the competition between the Kondo effect and the RKKY interactions among f electrons has an important role in these systems, as theoretically discussed [31].

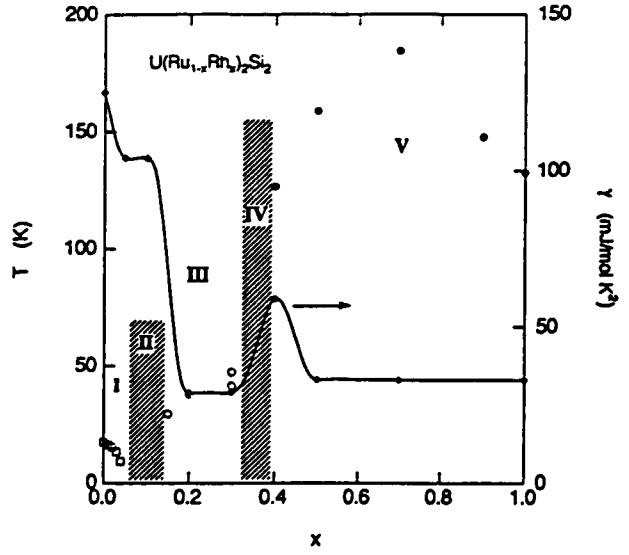

Figure 3.17: *Magnetic phase diagram of* $U(Ru_{1-x}Rh_x)_2Si_2$ *and the electronic-specific-heat coefficient* γ. □, ○, *and* • *represent the phase-transition temperature in each phases [22].*

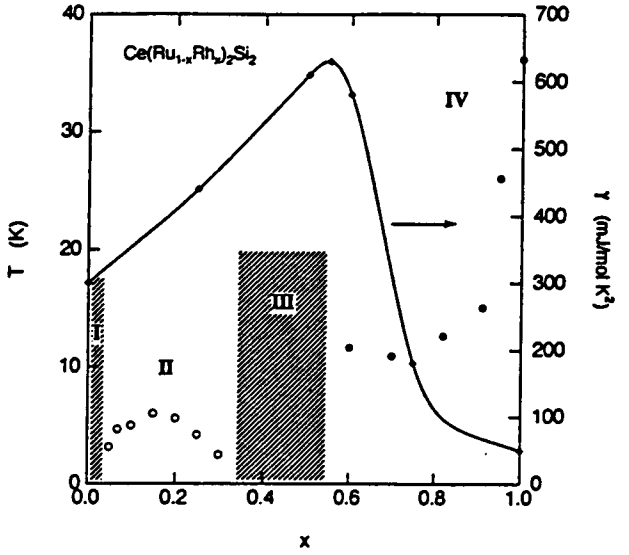

Figure 3.18: *Magnetic phase diagram of* $Ce(Ru_{1-x}Rh_x)_2Si_2$ *and the electronic-specific-heat coefficient* γ. ○ *and* • *represent the phase-transition temperature in each phases [22].*

Bibliography

[1] K. Hiebl, C. Horvath, P. Rogl, and M.J. Sienko, J. Magn. Magn. Mater. **37**, 287 (1983).

[2] T.T.M. Palstra, A.A. Menovsky, J.van den Berg, A.J. Dirkmaat, P.H. Kes, G.J. Nieuwenhuys, and J.A. Mydosh, Phys. Rev. Lett. **55**, 2727 (1985).

[3] K. Sugiyama, H. Fuke, K. Kindo, K. Shimohata, A.A. Menovsky, J.A. Mydosh, and M. Date, J. Phys. Soc. Jpn. **59**, 3331 (1990).

[4] T.T.M. Palstra, A.A. Menovsky, and J.A. Mydosh, Phys. Rev. B **33**, 6527 (1986).

[5] C. Broholm, J.K. Kjems, W.J.L. Buyers, P. Matthews, T.T.M. Palstra, A.A. Menovsky, and J.A. Mydosh, Phys. Rev. Lett. **58**, 1467 (1987).

[6] T.E. Mason, B.D. Gaulin, J.D. Garrett, Z. Tun, W.J.L. Buyers, and E.D. Isaacs, Phys. Rev. Lett. **65**, 3189 (1990).

[7] C. Broholm, H. Lin, P. Matthews, T.E. Mason, W.J.L. Buyers, M.F. Collins, A.A. Menovsky, J.A. Mydosh, and J.K. Kjems, Phys. Rev. B **43**, 12 809 (1991).

[8] E.D. Isaacs, D.B. McWhan, R.N. Kleiman, D.J. Bishop, G.E. Ice, P. Zschack, B.D. Gaulin, T.E. Mason, J.D. Garrett, and W.J.L. Buyers, Phys. Rev. Lett. **65**, 3185 (1990).

[9] M.B. Maple, J.W. Chen, Y. Dalichaouch, T. Kohara, C. Rossel, M.S. Torikachvili, M.W. McElfresh, and J.D. Thompson, Phys. Rev. Lett. **56**, 185 (1986).

[10] W. Schlabitz, J. Baumann, B. Pollit, U. Rauchschwalbe, H.M. Mayer, U. Ahlheim, and C.D. Bredl, Z. Phys. B **62**, 171 (1986).

[11] B. Renker, F. Gompf, E. Gering, P. Frings, H. Rietshel, R. Felten, F. Steglich, and G. Weber, Physica B **148**, 41 (1987).

[12] L.C. Gupta, D.E. MacLaughlin, C. Tien, C. Godart, M.A. Edwards, and R.D. Parks, Phys. Rev. B **28**, 3673 (1983).

[13] J.L. Tholence, P. Haen, D. Jaccard, P. Lejay, J. Flouquet, and H.F. Braun, J. Appl. Phys. **57**, 3172 (1985).

[14] A. Amato, C. Baines, R. Feyerherm, J. Flouquet, F.N. Gygax, P. Lejay, A. Schenck, and U. Zimmermann, Physica B **186-188**, 276 (1993).

[15] P. Haen, J. Flouquet, F. Lapierre, P. Lejay, and G. Remenyi, J. Low. Temp. Phys. **67**, 391 (1987).

[16] M.J. Besnus, J.P. Kappler, P. Lehmann, and A. Meyer, Solid State Commun. **55.** 779 (1985).

[17] F. Lapierre and P. Haen, J. Magn. Magn. Mater. **108**, 167 (1992).

[18] R. Djerbi, P. Haen, F. Lapierre, P. Lehmann, and J.P. Kappler, J. Magn. Magn. Matter. **76-77**, 260 (1988).

[19] H. Haen, J.P. Kappler, F. Lapierre, P. Lehmann, P. Lejay, J. Flouquet, and A. Meyer, J. de Phys. **49**, C8-757 (1988).

[20] Y. Miyako, S. Kawarazaki, H. Amitsuka, C.C. Paulsen, and K. Hasselbach, J. Appl. Phys. **70**, 5791 (1991).

[21] Y. Miyako, T. Kuwai, T. Taniguchi, S. Kawarazaki, H. Amitsuka, C.C. Paulsen, and T. Sakakibara, J. Magn. Magn. Mater. **108**, 190 (1992).

[22] Y. Miyako, H. Amitsuka, S. Kawarazaki, T. Taniguchi, and T. Sikama, *Physical Properties of Actinide and Rare Earth Compounds*, JJAP Series 8, (Jpn. J. Appl. Phys., Tokyo, 1993) p. 230.

[23] S. Kawarazaki, T. Taniguchi, H. Iwabuchi, Y. Miyako, H. Amitsuka, and T. Sakakibara, Phys. Lett. A **160**, 103 (1991).

[24] T. Sakakibara, C. Sekine, H. Amitsuka, and Y. Miyako, J. Magn. Magn. Mater. **108**, 193 (1992).

[25] C. Sekine, T. Sakakibara, H. Amitsuka, Y. Miyako, and T. Goto, J. Phys. Soc. Jpn. **61**, 4536 (1992).

[26] K. Fujiwara, K. Kumagai, C. Sekine, S. Murayama, Physica B **186-188**, 517 (1993).

[27] S. Kawarazaki, Y. Kobashi, J.A. Fernandez-Baca, S. Murayama, Y. Ōnuki, and Y. Miyako, Physica B **206-207**, 298 (1995).

[28] Y. Miyako, T. Takeuchi, T. Taniguchi, Y. Yamamoto, S. Kawarazaki, M. Acet, G. Dumpich, and E.F. Wassermann, Z. Phys. B **101**, 339 (1996).

[29] Y. Miyako, T. Takeuchi, T. Taniguchi, S. Kawarazaki, K. Marumoto, R. Hamada, Y. Yamamoto, M. Ocio, P. Pari, and J. Hammann, J. Phys. Soc. Jpn. **65**, Suppl. B pp. 12 (1996).

[30] Y. Miyako, T. Takeuchi, T. Taniguchi, S. Kawarazaki, K. Marumoto, R. Hamada, Y. Yamamoto, M. Sato, Y. Tabata, H. Tanabe, M. Ocio, P. Pari, and J. Hammann, Physica B, to be published in 1997.

[31] J.S. Schilling, Phys. Rev. B **33**, 1667 (1986).

Chapter 4

Experimental procedures

4.1 Sample preparation

The samples prepared for this work are listed in Table 4.1. All samples are single crystals except for $(U_{0.15}La_{0.85})Ru_2Si_2$. These compounds were made from the starting elements listed in Table 4.2. The polycrystal sample with the button shape was prepared by arc-melting of the stoichiometric amounts of the starting elements under a purified-argon atmosphere. After melting the starting materials, the sample turned over and remelted. This melting procedure were repeated several times (about 7 times) to ensure the sample homogeneity. The weight of the prepared polycrystal sample was about 10 g.

The single-crystal samples were prepared by the Czochralski method with a tri-arc furnace as schematically shown in Fig. 4.1. The single crystal was grown by pulling up the melting sample using the pulling rod under a purified-argon atmosphere. The diameter of the as-grown single crystal was controlled either by adjusting the arc current or by changing the pulling speed.

The sample characterization have been performed by using the powder X-ray diffractometer and the X-ray Laue picture. The results of the X-ray diffraction confirmed that all samples show a single phase and crystallize in the $ThCr_2Si_2$-type body-centered tetragonal structure. The formation of a single crystal and the direction of the axes were checked by taking the Laue picture.

The single-crystalline samples were cut by using a microcutter and a spark erosion cutter. The rectangular-shaped samples of about 5 mm in length were used for the measurement of the magnetic susceptibility and magnetization up to 7 T. For the high-field magnetization measurement, the sample was polished to make the thickness about 0.5 mm, or powdered, to prevent the eddy current heating. The rectangular-parallelepiped samples of the typical dimension of $s = 0.5 \times 0.5$ mm^2, $l = 5$ mm were cut for the electrical-resistivity measurement, and $s = 0.8 \times 2.5$ mm^2, $l = 7$ mm for the Hall-effect measurement. The polycrystalline samples (~ 2 g) were used for the specific-heat measurement.

Compound	impurity concentration
$(U_xLa_{1-x})Ru_2Si_2$	x=0.05, 0.07, 0.15
$(Ce_xLa_{1-x})Ru_2Si_2$	x=0.01, 0.05, 0.10
$(Pr_xLa_{1-x})Ru_2Si_2$	x=0.02, 0.05, 0.10
$LaRu_2Si_2$	
$U(Ru_{1-x}Rh_x)_2Si_2$	x=0.02, 0.03
URu_2Si_2	

Table 4.1: *Samples prepared for this work.*

Element	Purity	Shape
U	3N	ingot
La	3N,4N	ingot
Ce	3N	ingot
Pr	3N	ingot
Ru	3N	powder
Rh	3N	powder
Si	5N	ingot

Table 4.2: *Elements used for the sample making.*

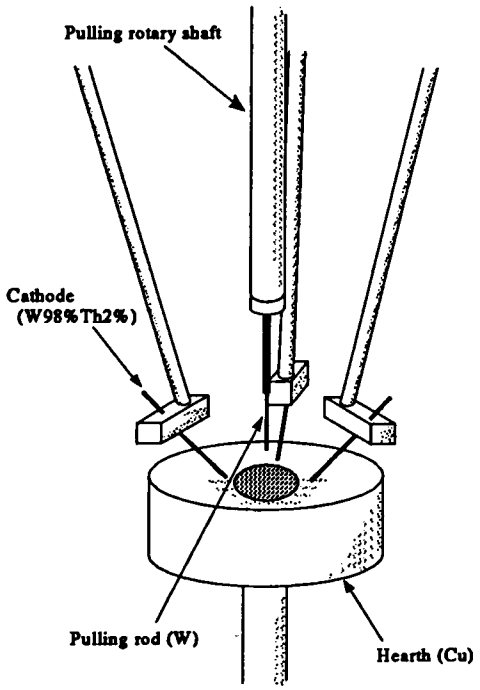

Figure 4.1: *Schematic view of the tri-arc furnace.*

4.2 Magnetic-susceptibility measurement

The magnetic-susceptibility measurements in the temperature range from 1.8 to 300 K were performed by the superconducting-quantum-interference-device (SQUID) magnetometer (Quantum Design Co., MPMS) and by the Faraday method using CAHN-2000 Electro-Balance system. The resolution of the measurements using the SQUID magnetometer is about 10^{-7} emu. The applied magnetic fields were between 0.5 and 0.7 T in this work. The magnetic-field dependence of the susceptibility was not observed in the whole temperature range below 0.7 T.

The principle of the measurement by the SQUID system is schematically shown in Fig. 4.2. The sample is magnetized in the uniform magnetic field generated by the superconducting magnet. When the sample is moving in the pick-up coil (the second-order differential gradiometer) from the top to the bottom, the variation of the flux, which is caused by the sample movement, generates the screening current in the primary coil. The screening current is detected finally as the output voltage of the rf SQUID system through the secondary coil. The magnetization of sample is counted from this signal automatically.

The principle of the measurement by the CHAN-2000 is as follows. The sample in a basket is suspended by a fine quartz rod from the electro-balance system and set near the maximum point of the field gradient of an iron-core electromagnet. The force acting on the sample is written as

$$F = \frac{1}{2} v \chi H \frac{dH}{dz}, \tag{4.1}$$

where v is volume of the sample and χ is the susceptibility. This force can be obtained by evaluating the current flowing through the torque motor of the balance. This current is monitored by a computing digital multimeter. Subtracting the blank data without sample, the susceptibility is obtained. The magnetic force is calibrated using a standard sample $FeSO_4(NH_4)_2SO_4 \cdot 6H_2O$.

The magnetic-susceptibility measurement down to 350 mK was performed by using a Hartshorn bridge ac method with a dilution refrigerator in the magnetic field of 7 Oe. The sample is magnetized in the alternating magnetic field generated by the primary coil as shown in Fig. 4.3. The magnetization of the sample changes the magnetic-flux density within the secondary coil and induces the electromotive force. The electromotive force is proportional to the time differential of the magnetic-flux density. The secondary coil is composed of two coils which are wound oppositely to each other with the same turns in order to cancel the induced electromotive force without the sample. The output voltage of the secondary coil is adjusted to be zero at 4.2 K, then this voltage is proportional to the change of the susceptibility from 4.2 K. The susceptibility is obtained by comparing the output voltage of the paramagnetic sample Gd_2O_3.

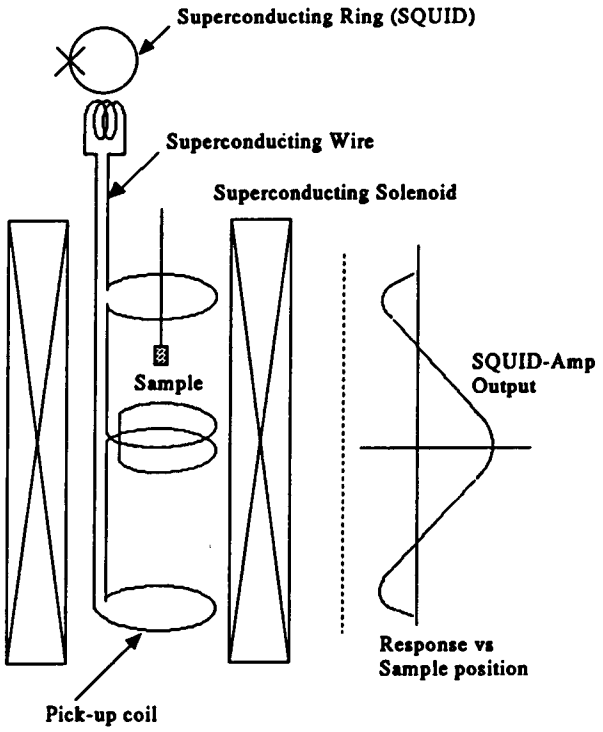

Figure 4.2: *Schematic view of the SQUID system.*

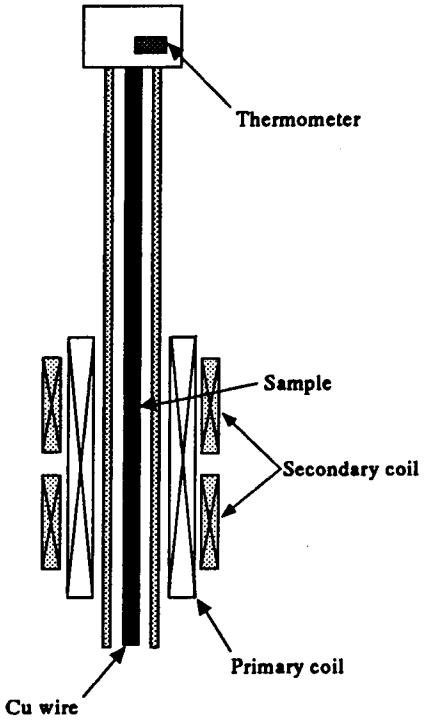

Figure 4.3: *Schematic view of the primary and secondary coils.*

4.3 Magnetization measurement

The magnetization measurements up to 7 T at various temperatures were performed by the SQUID magnetometer.

The high-field magnetization measurements up to 30 T were performed at the high magnetic field laboratory of Research Center for Extreme Materials, Osaka University. The single-layer large bore magnet 150(1L)60 were used in this experiment. This magnet can produce magnetic field up to 40 T. The magnetization was measured by using a balanced pick-up coil system [1].

The technically important point of the pick-up-coil system is how to compensate the background flux change due to a transient field. This is done by setting three coils as shown schematically in Fig. 4.4. The A-coil picks up the magnetic-flux change of the sample while the B-coil is wound in the opposite direction to the A-coil in order to compensate the background flux change. Fine adjustment is done by changing the output of the one-turn C-coil using a bridge-balance circuit. The A- and B-coil are wound around the specimen with 80 turns on a 3.0 mm diameter bakelite bobbin and 40 turns on a 4.3 mm diameter bakelite bobbin on the A-coil, respectively. The cross section of B-coil is twice as large as that of A-coil so as to make the net flux in A-coil is equal to that in B-coil. The C-coil is wound on the B-coil.

The out-put signal of the bridge-balance circuit is proportional to dM/dt but still contains background noise. The transient digital recorder is used to reduce this residual noise. Two sets of data, with and without specimen, are taken by using two shots of pulsed field. The signal dM/dt is obtained by the difference of these two data. The field derivative of magnetization dM/dH is calculated by dividing the subtracted data dM/dt by the signal dH/dt. The field and magnetization pick-up coils are calibrated by single crystalline MnF_2 as the standard sample using the spin-flop transition field and the magnetization above the transition. The block diagram of the magnetization-measurement system is shown in Fig. 4.5.

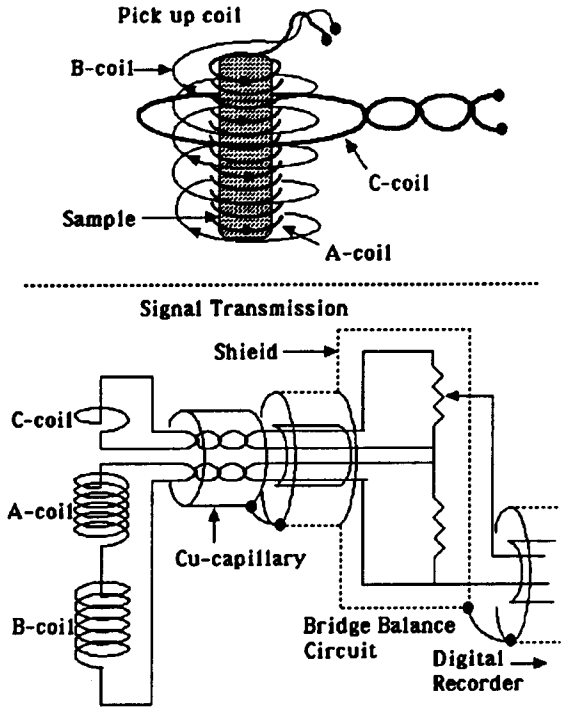

Figure 4.4: *Schematic view of the pick-up-coil system and the bridge-balance circuit for the fine compensation.*

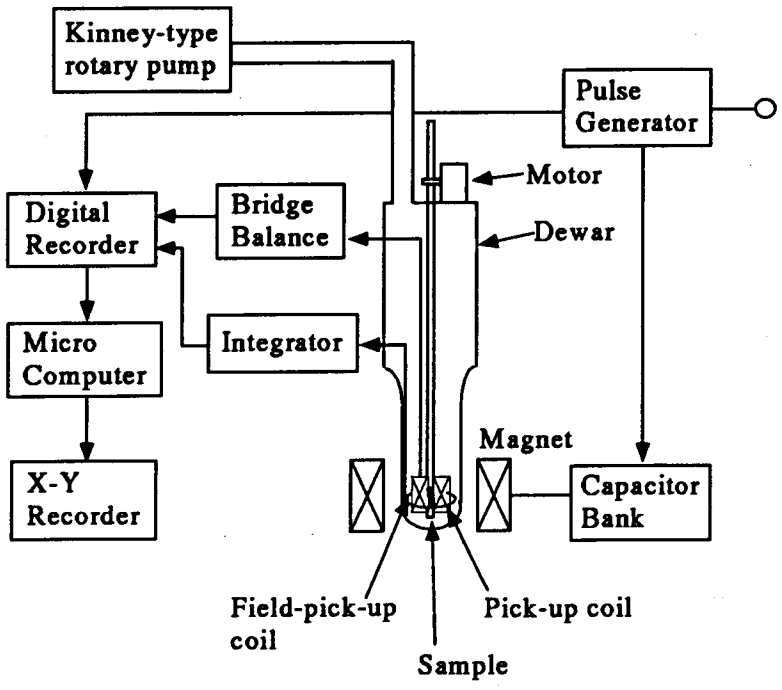

Figure 4.5: *Block diagram of the magnetization-measurement system.*

4.4 Specific-heat measurement

The specific-heat measurements in the temperature range from 2 to 80 K were performed by a quasi-adiabatic heat-pulse method. The adiabatic method is the simplest calorimetry technique for obtaining the absolute value of the heat capacity if the sample holder can be isolated thermally from the surroundings. In practice, however, it is difficult to maintain the adiabatic condition sufficiently in a wide temperature range. The temperature-dependent heat leaks from the sample holder to the surroundings cause a systematic error in the measured specific-heat value. This heat leaks are mainly due to the lead wires of the thermometer and heater. In order to correct such error, the quasi-adiabatic method was used to measure the specific heat in this study. This method is a hybrid between the adiabatic and thermal-relaxation method. It is firstly introduced by Keesom and Kok [2].

The principle of this method is as follows. Figure 4.6 shows a typical temperature vs time curve of an adiabatic pulse-heat cycle. In this figure, t_{on} and t_{off} are defined as the start and end time of the heating period, and $T_1(t)$ and $T_2(t)$ are defined as the temperature of the sample before and after the heating, respectively. $U(t)$ is defined as the extrapolated temperature difference between $T_2(t)$ and $T_1(t)$; *i.e.*, $U(t) \equiv T_2(t) - T_1(t)$ for $t \geq t_{off}$. The specific heat at $T_m = \frac{1}{2}[T_1(t_{on}) + T_2(t_{off})]$ is expressed as

$$C(T_m) = \frac{q\Delta t}{\Delta T}\left[\frac{\tau}{\Delta t}\left\{1 - \exp\left(-\frac{\Delta t}{\tau}\right)\right\}\right], \tag{4.2}$$

where q is the heat power per second supplied to the sample, $\Delta t = t_{off} - t_{on}$, and $\Delta T = U(t_{off})$. τ is the relaxation time calculated by using the least-square fit to the $U(t)$ vs t data as follows.

$$U(t) = \Delta T \exp\left(-\frac{t - t_{off}}{\tau}\right). \tag{4.3}$$

The cryostat of the calorimeter was designed and made by ourself to use above the ^{3}He temperature region. The schematic view of the cryostat and inner parts of the vacuum can are shown in Fig. 4.7 and Fig. 4.8. Three-type thermometers were used in the measurements in the two ways. One thermometer pair is a bare-element germanium (Ge)-chip resistor (2 to 40 K) and a platinum (Pt) thermometer (20 to 80 K). Another thermometer is a Cernox one (2 to 80 K). These thermometers and the pulse heater of a constantan wire were glued to a sapphire substrate with GE varnish. The sample was also attached to a sapphire substrate with GE varnish. The whole assembly is suspended by silk threads to avoid the heat leak. Similarly, the constantan wires are used for all lead wires to avoid the heat leak. The experimental value of the heat capacity is obtained by using a fully computerized system which block diagram is shown in Fig. 4.9. To avoid the heating-up effect of the thermometer, the automatic resistance bridge AVS-45 and AVS-47 (RV-Elektronikka Oy, Finland) were used for the measurement.

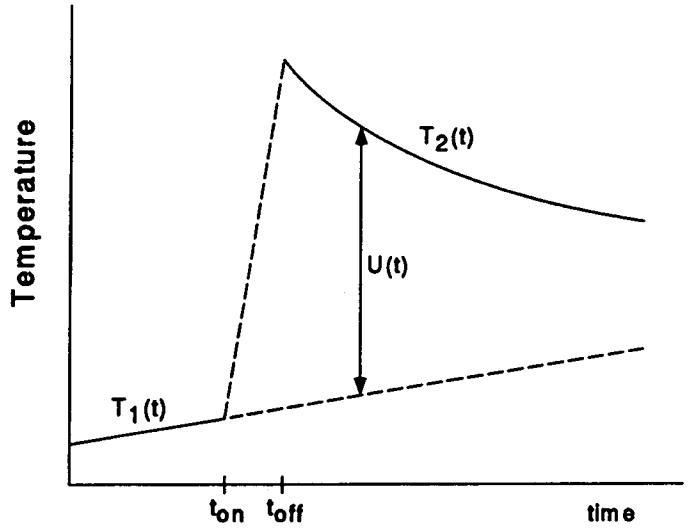

Figure 4.6: *Typical temperature vs time curve of an adiabatic pulse-heat cycle. Symbols are described in the text.*

4.5 Electrical-resistivity measurement

The electrical-resistivity measurements in the temperature range from 20 mK to 300 K were performed by a standard four-terminal dc method. The measurements below 2 K were performed with a dilution refrigerator. Four contacts to the bar-shaped samples were made by ultrasound soldering with Al wire or silver paste with Cu wire. The experimental values of the resistance were obtained by averaging the some measured values in the forward and inverted currents at the controlled temperatures. The resistance voltage was measured with the current of 10 mA. The error of the absolute value in the resistivity is 20 %, because of the error introduced by the three dimension measurements required in its calculation and to a lesser extent by the unideal sample and contact geometry. However, the relative error is less than 0.2 %.

4.6 Hall-effect measurement

The Hall-effect measurements were performed in the temperature range from 2 to 150 K. The sample with four contacts made by silver paste was mounted on the copper sample holder with GE varnish so that the c axis was normal to the (vertical) probe direction. Current contacts were attached at each end of the sample. The magnetic field applied perpendicular to the current direction was provided by a superconducting magnet with a maximum field of 8 T. The remaining contacts were attached as accurately as possible on opposite sides of the sample so that they were in a line perpendicular to the direction of the current flow for Hall-voltage measurements. The Hall voltage $V_H(H)$ was determined from the potential $V(H)$ between the transverse contacts with the magnetic field parallel

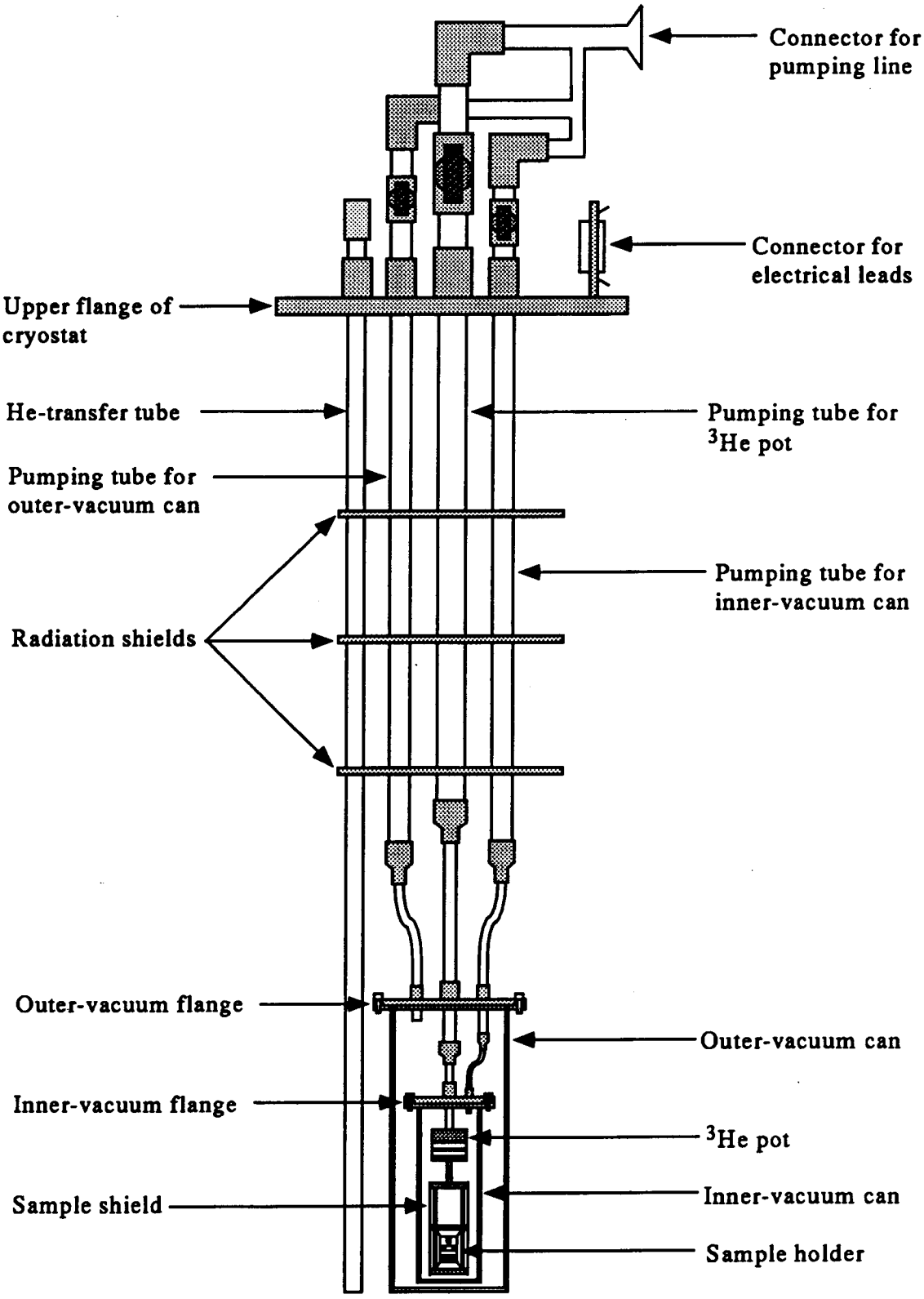

Figure 4.7: *Schematic view of the ^{3}He cryostat used for the heat-capacity measurement.*

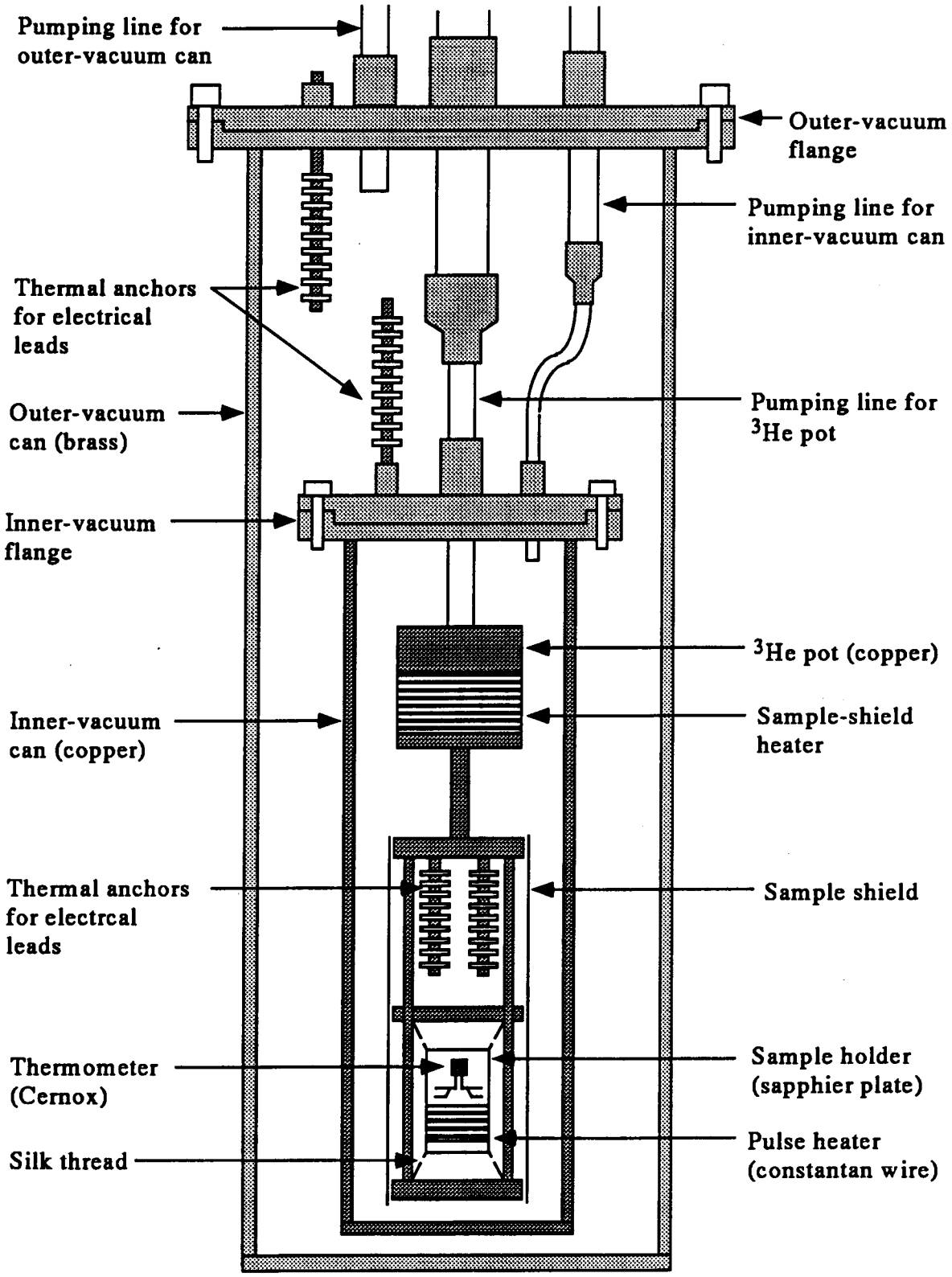

Figure 4.8: *Schematic view of the construction details of the inner parts of the ^{3}He cryostat.*

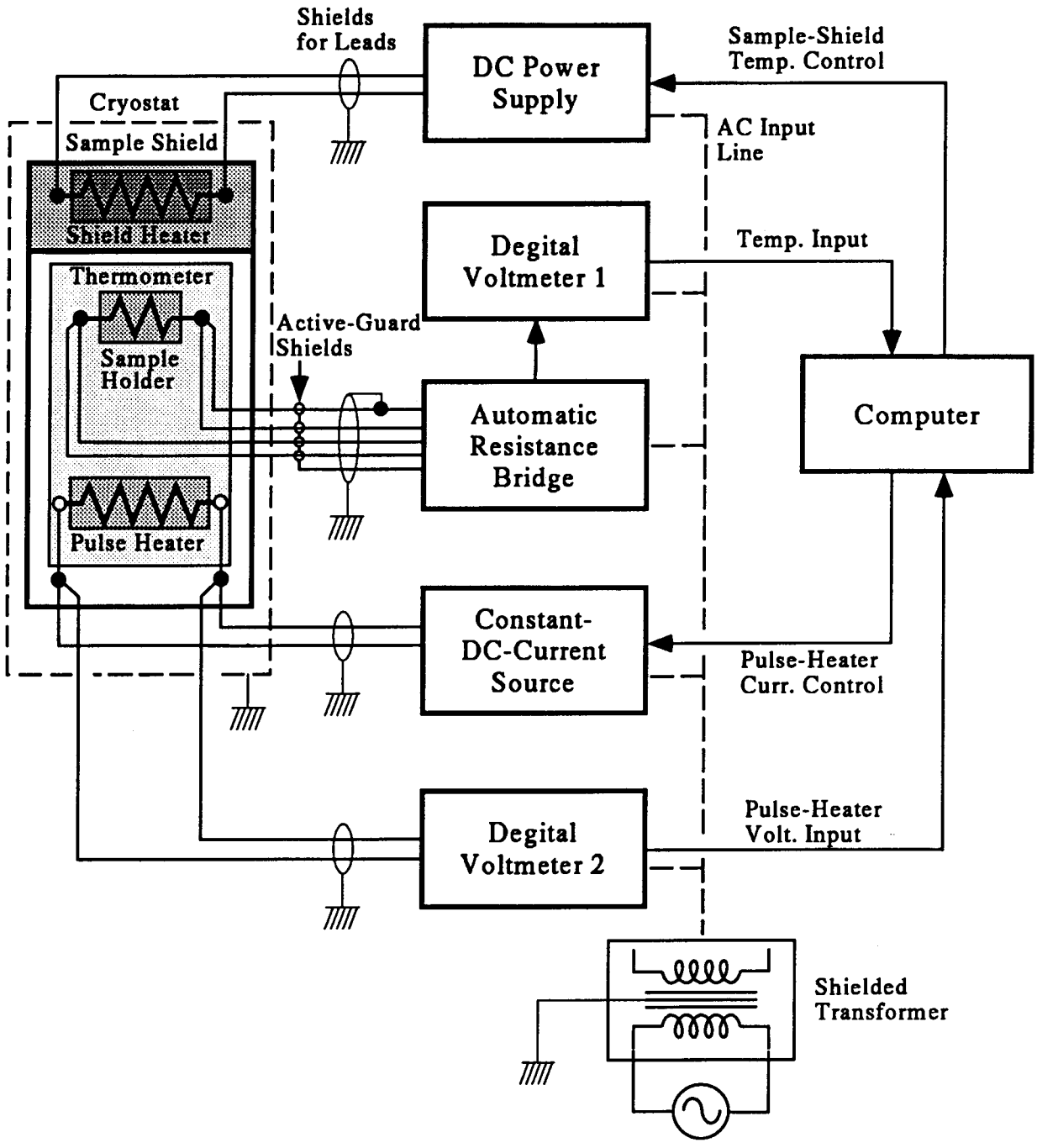

Figure 4.9: *Block diagram of the automatic calorimetric system.*

to the c axis according to

$$V_H(H) = \frac{1}{2}[V(H) - V(-H)]. \tag{4.4}$$

The potential $V(H)$ was determined by averaging the some measured voltage in the forward and inverted currents. The Hall coefficient is calculated from

$$R_H(t) = \frac{V_H(H)t}{HI}, \tag{4.5}$$

where t is the sample thickness, H is the magnetic field, and I is the current. The Hall voltage was measured with the current of 20 mA. Absolute measurement of the Hall coefficient is much better than that of the electrical resistivity since it only depend on accurate measurement of the sample's thickness.

Bibliography

[1] T. Sakakibara, H. Mollymoto, M. Motokawa, and M. Date, *High Field Magnetism*, edited by M. Date (North-Holland, Amsterdam, 1983) p. 299.

[2] W.H. Keesom and J.A. Kok, Proc. Acad. Sci. Amsterdam **35**, 294 (1932).

Chapter 5

Magnetism of the dilute uranium compound system $(U_xLa_{1-x})Ru_2Si_2$

5.1 Introduction

As introduced in Chapter 1 and 3, URu_2Si_2 is known as the interesting material exhibiting the complicated magnetism. It is classified as the heavy-fermion system with the reported γ value of 112 [1] and 180 mJ/K^2 mol [2]. It shows the large uniaxial magnetic anisotropy and the coexistence of a type-I antiferromagnetic order (T_N = 17.5 K) with an unusually small ordered moment ($\sim 0.04\mu_B$) and non-BCS-type superconductivity (T_c = 1.2 K) [3, 4, 5, 6].

For the interpretation of this magnetism, the singlet-ground-state CEF model with the CEF splitting of about 40 K is proposed [7, 8, 9]. This model, however, can not explain consistently the various experimental results of the magnetic susceptibility, magnetization, the specific heat, *etc.*. Another interpretation of the magnetism of URu_2Si_2, the SDW model is proposed for the phase-transition mechanism [1, 10]. This model can explain the Cr-like anomaly of the electrical resistivity at T_N. The decrease in γ value below T_N can be explained by the partial gap opening of the Fermi surface due to the formation of a SDW. This model, however, contradicts to the experimental result of the electrical resistivity in the high magnetic field up to 25 T [11]. This result shows the disagreement of the magnetic field dependence of the ordered moment with that of the resistivity anomaly caused by the phase transition. It suggests the existence of another order parameter differed from the magnetic dipole. There is no agreement in the interpretation of the magnetism of URu_2Si_2. The mechanism of the phase transition at T_N is still controversial. It seems that a complete explanation for the experimental results has not yet been given.

In order to clarify such uranium electron state in URu_2Si_2 experimentally, the study of the dilute uranium compound system $(U_xLa_{1-x})Ru_2Si_2$ has been performed as mentioned in this chapter[1]. The preliminary study has been performed partly [14, 15]. The study of the dilute uranium system can clarify the single-site property of the uranium ion, for example, the Kondo effect, the CEF effect. Furthermore, the inter-site effect in URu_2Si_2, for

[1] Parts of this chapter have already been published in Ref. [12, 13].

example, the RKKY interaction, the lattice coherency, will be clarified by using these single-site properties. The study of the dilute system can be a starting point for understanding the complicated magnetism of the lattice system URu_2Si_2.

Similar study for the dilute uranium system have been performed on the dilute uranium compound system $(U_xTh_{1-x})Ru_2Si_2$ ($x \leq 0.07$) [16, 17]. As explained later, however, for the temperature dependence of the magnetic susceptibility, $(U_xLa_{1-x})Ru_2Si_2$ is quite different from the dilute uranium system $(U_xTh_{1-x})Ru_2Si_2$ which indicates a logarithmic temperature dependence. The study about $(U_xTh_{1-x})Ru_2Si_2$ shows the non-Fermi-liquid behavior and suggests the possibility of the two-channel Kondo effect, which are quite different from the Fermi-liquid behavior observed in URu_2Si_2. The difference between $(U_xLa_{1-x})Ru_2Si_2$ and $(U_xTh_{1-x})Ru_2Si_2$ is discussed in the last part of this chapter.

5.2 Experimental results

5.2.1 Magnetic susceptibility

Figure 5.1 shows the magnetic susceptibilities of $(U_{0.05}La_{0.95})Ru_2Si_2$ and $LaRu_2Si_2$ single crystals along the c and a axes. It is noted that a large uniaxial magnetic anisotropy is observed for $(U_{0.05}La_{0.95})Ru_2Si_2$ as in URu_2Si_2. The susceptibility along the c axis obeys the Curie-Weiss law at high temperatures, while the susceptibility along the a axis is small and almost constant down to the lowest temperatures measured. The susceptibility of $LaRu_2Si_2$ is small and shows almost no temperature dependence. It shows a small constant negative and positive value in the field applied along the c and a axes, respectively, except for a small increase in the low-temperature region.

The uranium-concentration dependence for the magnetic susceptibility is studied by using the samples with $x = 0.07$ and 0.15. The magnetic susceptibilities of $x = 0.05$ and 0.07 along the c and a axes are shown in Fig. 5.2. The magnetic susceptibility of polycrystalline samples with $x = 0.05$, 0.07, and 0.15 are shown in Fig. 5.3. The contribution of $5f$ electrons is obtained by subtracting the susceptibility of $LaRu_2Si_2$. These data are almost similar to each other. However, there is a small difference in a gradient of the susceptibility in the low-temperature region. The susceptibility is suppressed when the uranium concentration increases as shown in Fig. 5.3. This may be understood by the effect of the antiferromagnetic RKKY interaction.

Figure 5.4 shows the magnetic susceptibility of $x = 0.07$ along the c axis down to 350 mK in the logarithmic-temperature scale. The data of $x = 0.15$, which is estimated from the experimental value of the powdered sample, are shown for a comparison with that of $x = 0.07$. The data of $x = 0.07$ keeps to increase with decreasing temperature, but it becomes nearly constant below about 10 K.

The modified Curie-Weiss law expressed below is used to fit the experimental result of the susceptibility.

$$\chi(T) = \chi_0 + \frac{N{\mu_{eff}}^2}{3k(T-\Theta)}, \tag{5.1}$$

where μ_{eff} is the effective moment, Θ is the Curie-Weiss temperature, N is the Avogadro number, and χ_0 is a constant component of the susceptibility. The fitting parameters for the dilute uranium system are listed in Table 5.1. The data of the powdered sample with $x = 0.15$ is modified to be used as that of the single-crystal sample. The fitting-temperature range is determined to minimize the deviation of the least-square fit.

U %	μ_{eff} (μ_B)	Θ (K)	χ_0 (emu/U mol)	Fitting-temperature range
5 %	3.12	-11.8	3.41×10^{-4}	$T \geq 15$ K
7 %	3.42	-10.9	-1.39×10^{-4}	$T \geq 18$ K
15 %	2.99	-12.0		$T \geq 22$ K

Table 5.1: *Fitting parameters of the modified Curie-Weiss law for the susceptibilities of $(U_xLa_{1-x})Ru_2Si_2$ (x = 0.05, 0.07, and 0.15) along the c axis.*

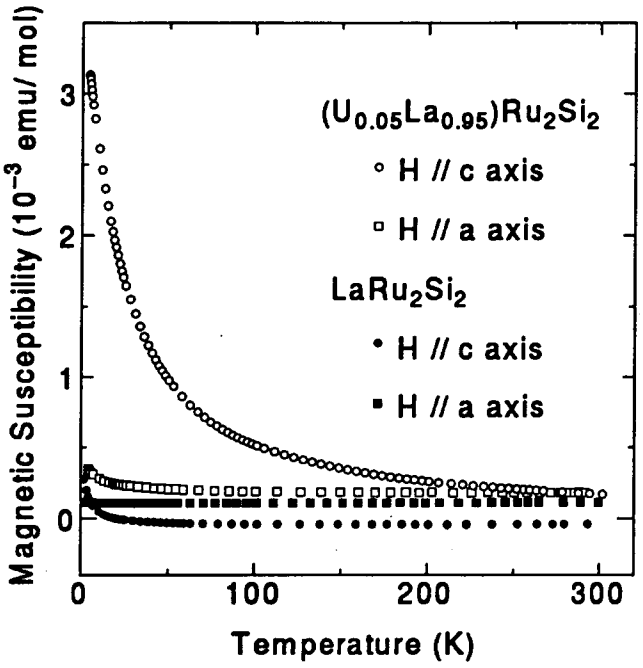

Figure 5.1: *Temperature dependence of the magnetic susceptibilities of $(U_{0.05}La_{0.95})Ru_2Si_2$ and $LaRu_2Si_2$ along the c and a axes.*

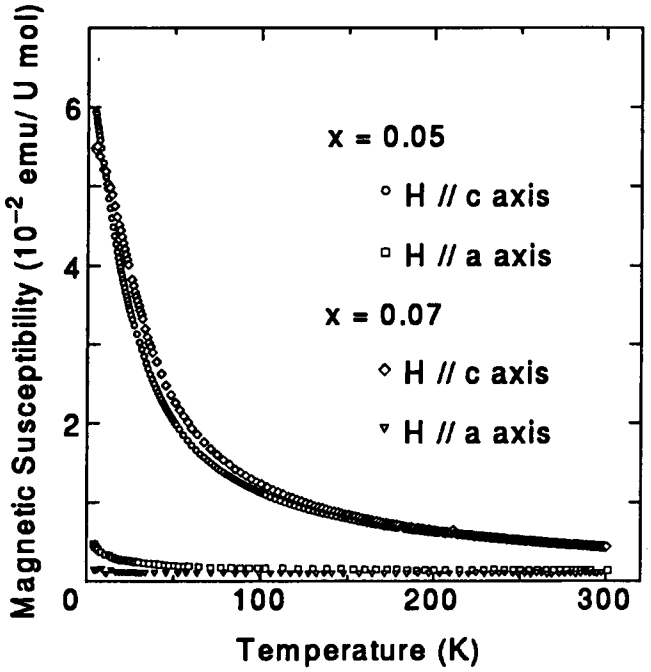

Figure 5.2: *Temperature dependence of the magnetic susceptibilities of $(U_xLa_{1-x})Ru_2Si_2$ (x = 0.05 and 0.07) along the c and a axes.*

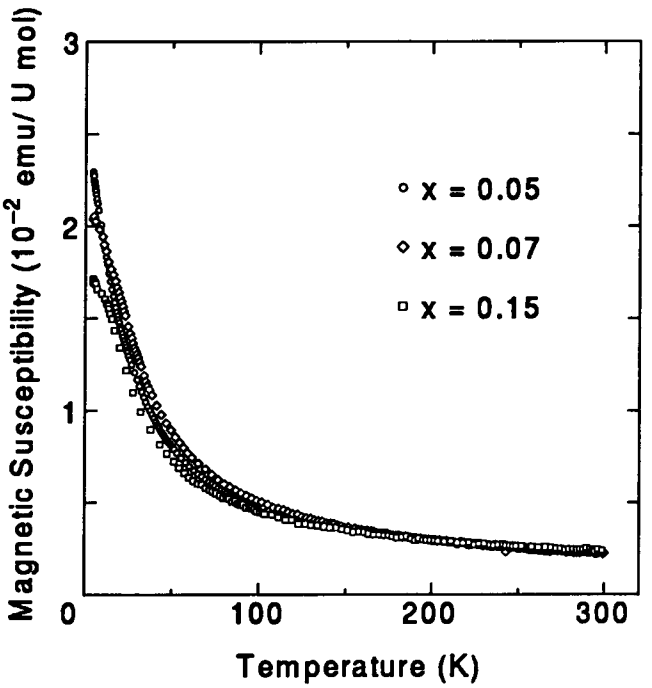

Figure 5.3: *Temperature dependence of the magnetic susceptibilities of $(U_xLa_{1-x})Ru_2Si_2$ (x = 0.05, 0.07, and 0.15)*:

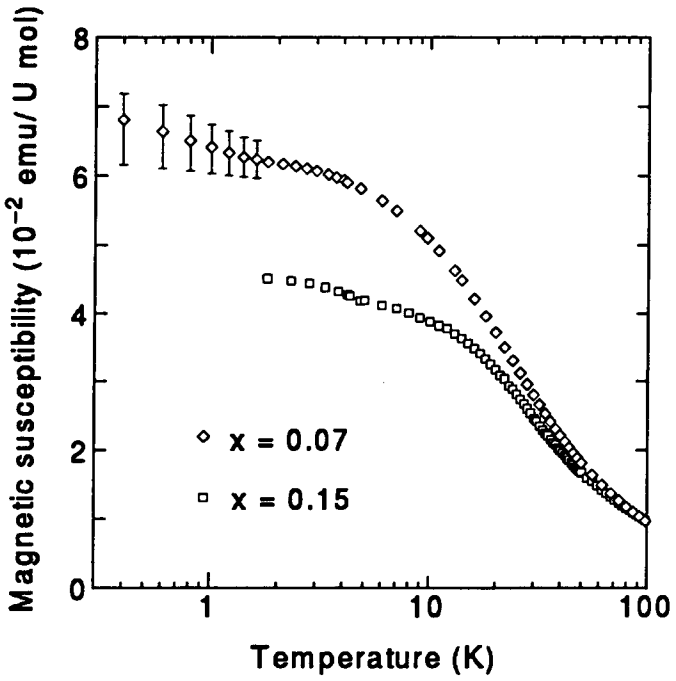

Figure 5.4: *Magnetic susceptibilities of $(U_xLa_{1-x})Ru_2Si_2$ (x = 0.07 and 0.15) along the c axis in the logarithmic-temperature scale. The data of x = 0.15 are estimated from the experimental value of the powdered sample.*

5.2.2 Magnetization

Figure 5.5 shows the magnetization curves of $(U_{0.05}La_{0.95})Ru_2Si_2$ and $LaRu_2Si_2$ single crystals along the c and a axes at 4.3 K. The large magnetic anisotropy is observed for $(U_{0.05}La_{0.95})Ru_2Si_2$. The magnetization of $(U_{0.05}La_{0.95})Ru_2Si_2$ along the c axis increases gradually up to 7 T, while the magnetization along the a axis is almost linear and small. The magnetization of $LaRu_2Si_2$ is negligibly small compared with that of $(U_{0.05}La_{0.95})Ru_2Si_2$. The magnetization curves of $(U_{0.05}La_{0.95})Ru_2Si_2$ at various temperatures along the c and a axes are shown in Fig. 5.6. All these data, except for the one along the c axis at 4.3 K, are almost linear up to 7 T. The magnitude of magnetization along the c axis at 4.3 K at 7 T is about 10 times larger than that along the a axis.

The high-field magnetization measurements were performed on the polycrystalline sample. The magnetization per uranium atom at 4.2 K is obtained for three $(U_xLa_{1-x})Ru_2Si_2$ with x = 0.05, 0.07, and 0.15, within the errors of 10% using the nominal concentrations. The contribution of $5f$ electrons is estimated in the same way mentioned above. As shown in Fig. 5.7, the magnetizations of the various uranium concentrations increase gradually and do not saturate even at 30 T.

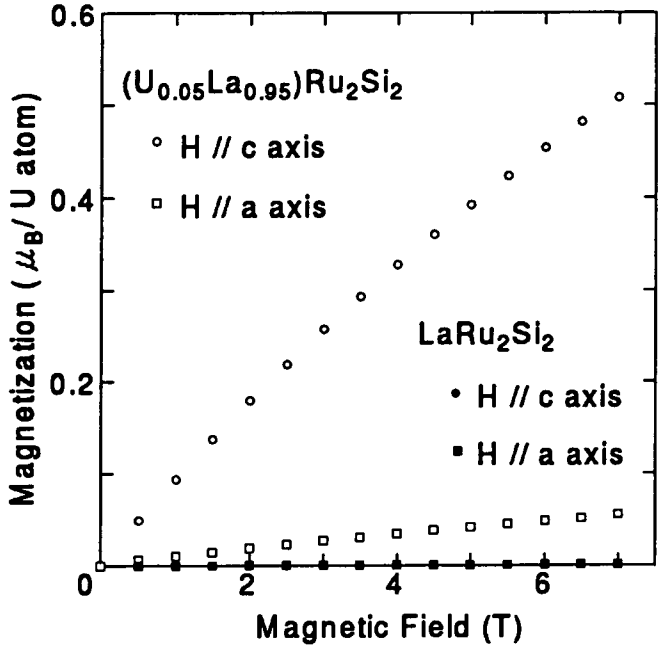

Figure 5.5: *Magnetization curves of $(U_{0.05}La_{0.95})Ru_2Si_2$ and $LaRu_2Si_2$ along the c and a axes at 4.3 K.*

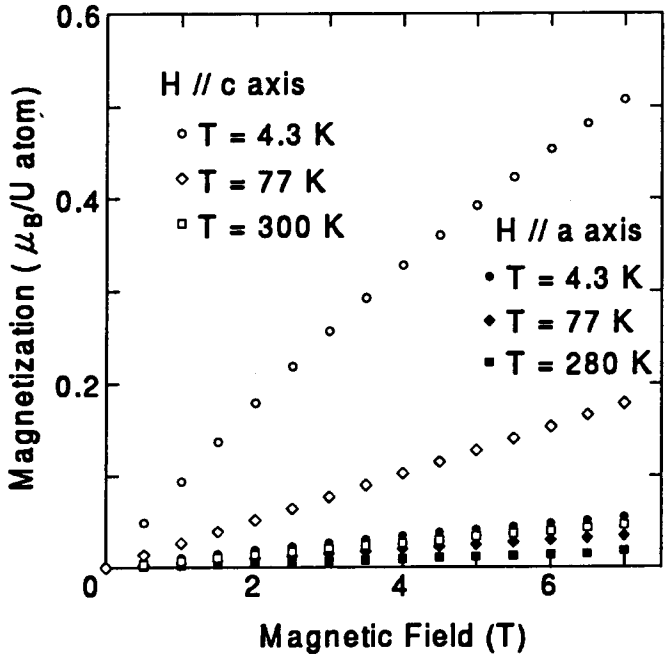

Figure 5.6: *Magnetization curves of $(U_{0.05}La_{0.95})Ru_2Si_2$ along the c and a axes at various temperatures.*

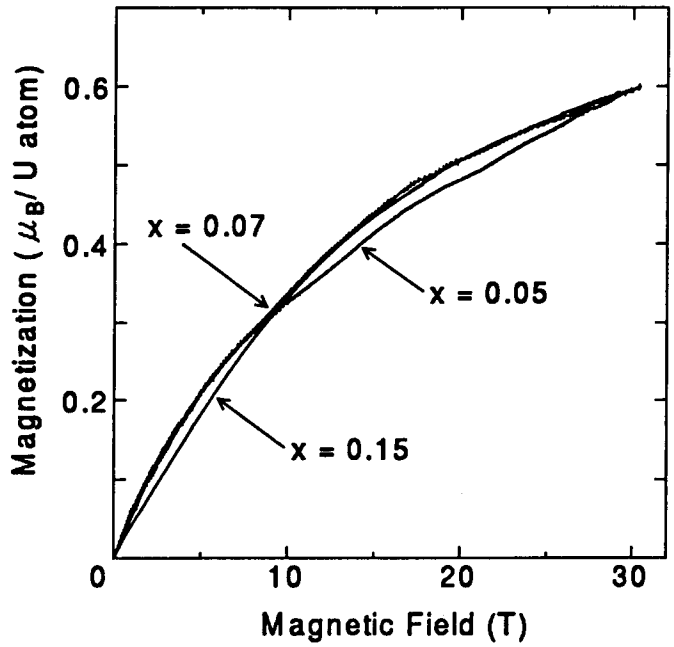

Figure 5.7: *High-field magnetization curves of* $(U_{0.05}La_{0.95})Ru_2Si_2$ *(*x *= 0.05, 0.07, and 0.15) at 4.2 K.*

5.2.3 Specific heat

The specific-heat measurements have been performed to study the thermodynamical behavior of the dilute uranium system at low temperatures. Figure 5.8 shows the specific heats of the $(U_xLa_{1-x})Ru_2Si_2$ (x = 0.05, 0.07, and 0.15) and $LaRu_2Si_2$ polycrystalline samples. No phase transition is observed for all uranium concentration. The lattice-specific heat is dominant at high temperatures and each sample shows the almost similar temperature dependence. The C/T vs T^2 plots of the specific heats of $(U_xLa_{1-x})Ru_2Si_2$ (x = 0.05, 0.07, and 0.15) and $LaRu_2Si_2$ are shown in Fig. 5.9. The C/T value increases almost linearly in proportion to the uranium concentration. The γ ($= C_{5f}/T$) value of $(U_xLa_{1-x})Ru_2Si_2$ (x = 0.05, 0.07, and 0.15) per uranium mole is estimated to be 130 $\pm$ 20 mJ/K^2 U mol. This γ value is almost the same as that of URu_2Si_2.

Figure 5.10 shows the electronic-specific heat of $(U_{0.15}La_{0.85})Ru_2Si_2$. The contribution of $5f$ electrons is obtained from the total specific heat by subtracting the lattice part using the reference compound $LaRu_2Si_2$. The specific heat of $LaRu_2Si_2$ is assumed to be equal to that of the lattice and conduction-electron part of the dilute system. The data show a broad maximum at around 25 K. The error bars in figure are explained later. The electronic-specific heat of the three compounds $(U_xLa_{1-x})Ru_2Si_2$ (x = 0.05, 0.07 and 0.15) shows the similar broad maximum at around 25 K. The qualitative behavior of the Schottky anomaly is almost independent of the uranium concentration. Figure 5.11 shows the C_{5f}/T vs T plot of the electronic-specific heat of $(U_{0.15}La_{0.85})Ru_2Si_2$. As seen in Fig. 5.11, the C_{5f}/T vs T

curve shows a broad maximum at around 17 K. This anomaly is similar to that observed for URu_2Si_2.

Although the total specific heat is measured with an experimental error of about 1 % in our measurement, the absolute value of the electronic specific heat per uranium mole has some ambiguity above 10 K. This ambiguity is mainly due to the small electronic specific heat in the dilute systems compared with the lattice part. For example, the contribution of the electronic part to the total specific heat is only about 3 % at 40 K. In addition, there is an inaccuracy of about 10 % coming from the nominal uranium concentration. This inaccuracy is estimated from the susceptibility and magnetization measurements for the samples with $x = 0.05$, 0.07, and 0.15. The estimated systematic errors are shown by the error bars in Fig. 5.10 and Fig. 5.11. The variation of the lattice specific heat per mole due to the change of the mean mass per unit lattice is small compared with the total error. Its contribution is estimated and considered in the error bars also.

The magnetic entropy is obtained by integrating the C_{5f}/T vs T plot as shown in Fig. 5.12. The obtained entropy is approaching to the value of $R\ln 3$ as temperature increases. This indicates that this dilute system has the threefold degeneracy of the CEF level at low temperatures.

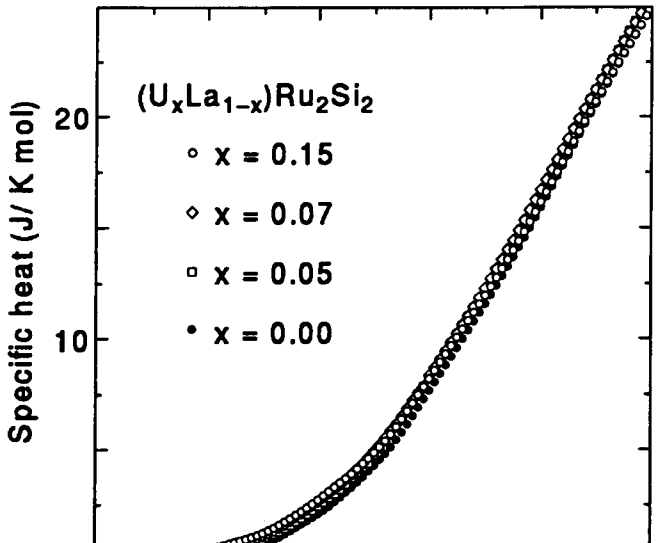

Figure 5.8: *Temperature dependence of the specific heats of $(U_xLa_{1-x})Ru_2Si_2$ ($x = 0.05$, 0.07, and 0.15) and $LaRu_2Si_2$.*

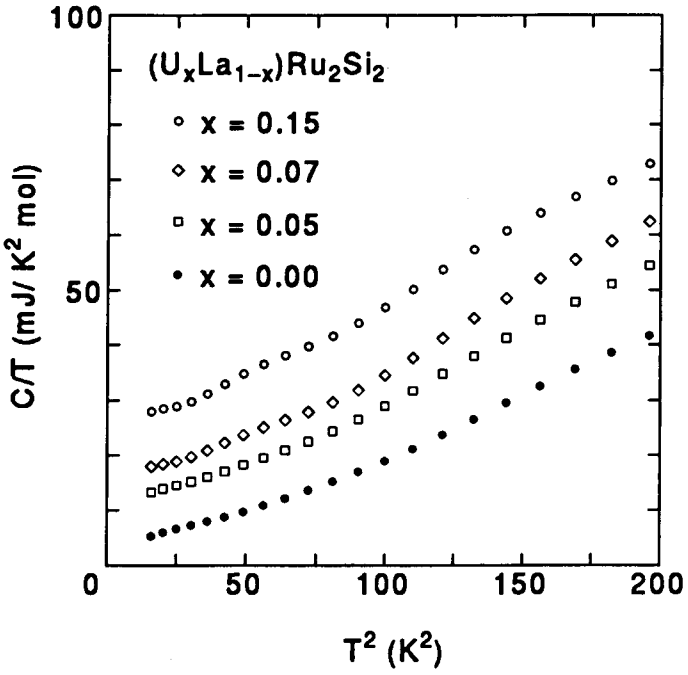

Figure 5.9: *C/T vs T^2 plots of the specific heats of $(U_xLa_{1-x})Ru_2Si_2$ (x = 0.05, 0.07, and 0.15) and $LaRu_2Si_2$.*

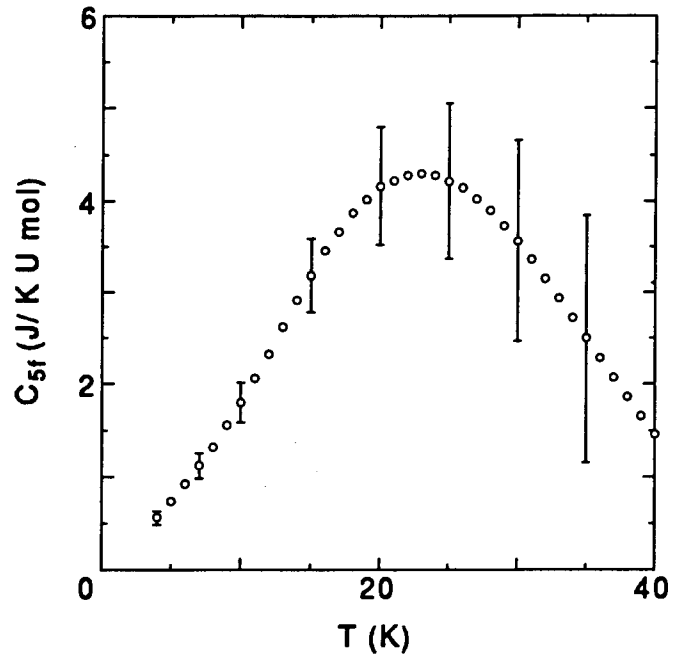

Figure 5.10: *Temperature dependence of the electronic-specific heat of $(U_{0.15}La_{0.85})Ru_2Si_2$.*

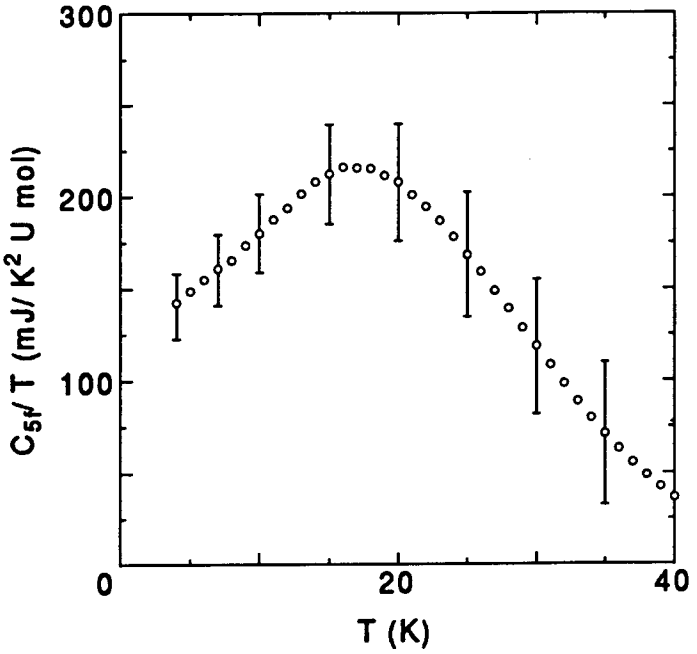

Figure 5.11: C_{5f}/T *vs* T *plot of the electronic-specific heat of* $(U_{0.15}La_{0.85})Ru_2Si_2$.

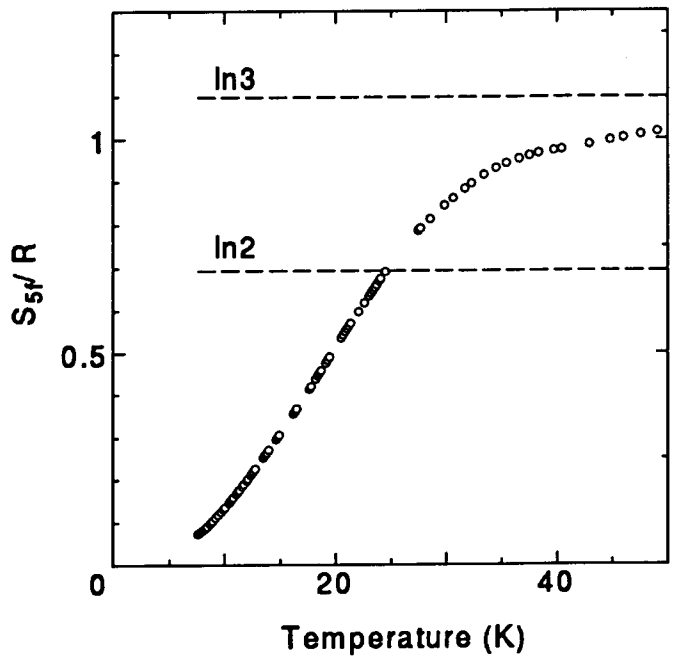

Figure 5.12: *Temperature dependence of the magnetic entropy of* $(U_{0.15}La_{0.85})Ru_2Si_2$.

5.2.4 Electrical resistivity

The electrical-resistivity measurements have been performed to study the transport property of the dilute uranium system. Figure 5.13 shows the electrical resistivities of the $(U_{0.07}La_{0.93})Ru_2Si_2$ and $LaRu_2Si_2$ single crystals with the current parallel to the c and a axes. As seen in Fig. 5.13, the data of $(U_{0.07}La_{0.93})Ru_2Si_2$ parallel to the both axes show a comparatively simple metallic nature. However, there is a distinct knee like structure at low temperature around 18 K, as reported for a polycrystal sample [18].

For the electrical resistivity of $LaRu_2Si_2$, the absolute values of the resistivities at the room temperature (295 K) are obtained to be 11 and 28 $\mu\Omega$ cm, and the residual values at low temperature (1.8 K) are 0.28 and 0.64 $\mu\Omega$ cm for the current parallel to the c and a axes, respectively. These values and the overall behavior of the temperature variation are in good agreement with those in the earlier work [19]. On the other hand, the resistivities of $(U_{0.07}La_{0.93})Ru_2Si_2$ shown in Fig. 5.13 are modified by a constant factor to show the same temperature gradient of the high-temperature resistivity of $LaRu_2Si_2$. The $(U_{0.07}La_{0.93})Ru_2Si_2$ sample is much more cleavable than that of $LaRu_2Si_2$ especially in the c plane, so that it is difficult to obtain the good sample for the resistivity measurement. Two samples are prepared for the resistivity measurement with the current parallel to the c axis. The actual values at 295 K are 362 and 1050 $\mu\Omega$ cm. These value are quite large and may be caused by the crack in the sample. If these two data are normalized at 295 K, they show the similar temperature dependence as shown in Fig. 5.13. Therefore, these data are considered to show the essential behavior of the resistivity except for the absolute value. The actual value of the resistivity of $(U_{0.07}La_{0.93})Ru_2Si_2$ with the current parallel to the a axis is 106 $\mu\Omega$ cm at 295 K. The resistivity parallel to the a axis is also modified in the similar way mentioned above. In the following discussion, the modified data are used as the resistivity of $(U_{0.07}La_{0.93})Ru_2Si_2$.

Fig. 5.14 shows the electrical resistivity of $(U_{0.07}La_{0.93})Ru_2Si_2$ and $LaRu_2Si_2$ with the current parallel to the c and a axes in the logarithmic-temperature scale. The data of $(U_{0.07}La_{0.93})Ru_2Si_2$ with the current parallel to the a axis is almost flat in the low temperature region between 20 mK and 1 K.

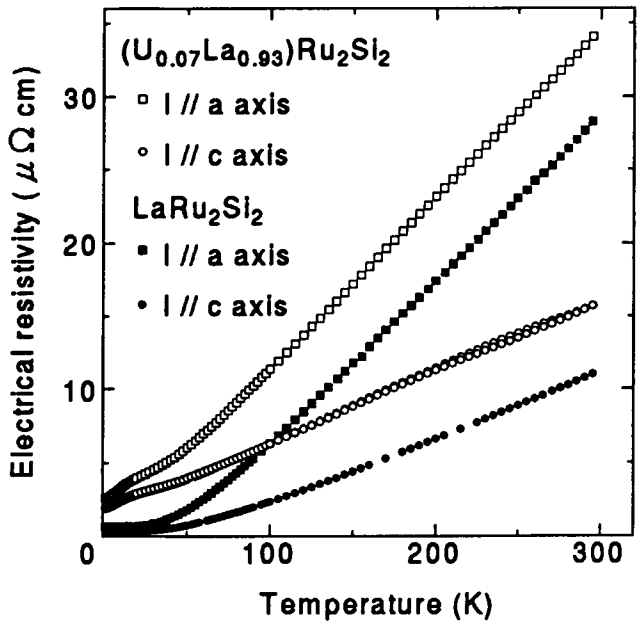

Figure 5.13: *Temperature dependence of the electrical resistivities of $(U_{0.07}La_{0.93})Ru_2Si_2$ and $LaRu_2Si_2$ with the current parallel to the c and a axes. The data of $(U_{0.07}La_{0.93})Ru_2Si_2$ are modified by a constant factor.*

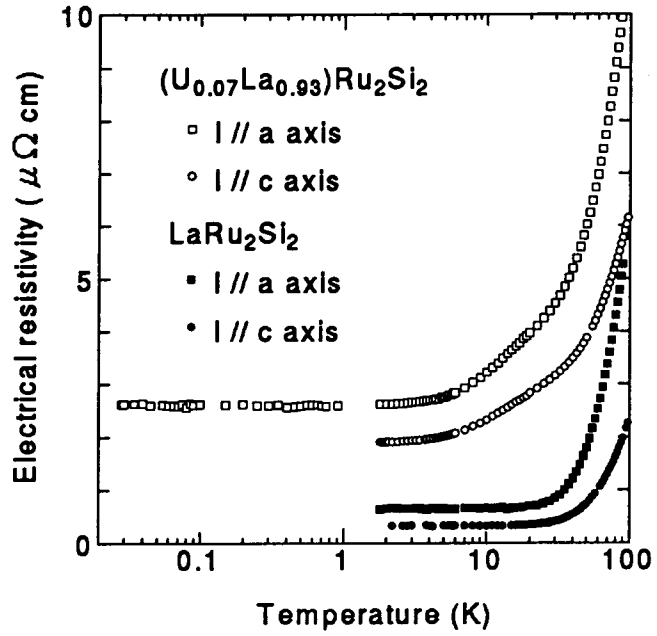

Figure 5.14: *Electrical resistivities of $(U_{0.07}La_{0.93})Ru_2Si_2$ and $LaRu_2Si_2$ with the current parallel to the c and a axes in the logarithmic-temperature scale. The data of $(U_{0.07}La_{0.93})Ru_2Si_2$ are modified by a constant factor.*

5.3 Analysis and discussion

5.3.1 Crystalline-electric-field splitting

The crystalline-electric-field (CEF) effect is considered to explain the large magnetic anisotropy of the experimental results in this section.

The electronic configurations of uranium is the radon (Rn) shell+$(5f)^3$+$(6d)^1$+$(7s)^2$. According to the earlier studies, it is possible that uranium in $(U_xLa_{1-x})Ru_2Si_2$ is in a tetra-valent state with two $5f$ electrons or a tri-valent state with three $5f$ electrons. The uranium ion is assumed here to be in either state.

The various interactions dealt in this study are classified according to their magnitudes [20]. The case of actinides is explained here. Intra-atomic correlation (U) is most important, as in the case of the lanthanides, and its order is 10^5 cm^{-1} ($\sim$ 12 eV). Spin-orbit coupling (H_{SO}) is very large and its order is 3×10^3 cm^{-1} ($\sim$ 0.37 eV). Crystal-field interaction (H_{CF}) is much stronger than that of lanthanides (the wave function of $5f$ electron is extended more than that of $4f$ electron) and its order is 10^3 cm^{-1} ($\sim$ 0.12 eV). The exchange interaction (H_{exch}) can be estimated from the ordering temperatures to be about 10^2 cm^{-1} (12 meV). These interactions are listed in Table 5.2 with those of lanthanides for a comparison. The order of the interactions is,

$$U > H_{SO} > H_{CF} > H_{exch}. \tag{5.2}$$

	Actinides	Lanthanides
U	~ 10	~ 20
H_{SO}	~ 0.3	~ 0.1
H_{CF}	0.01$\sim$0.1	< 0.01
H_{exch}	~ 0.01	$0.001 - 0.01$

Table 5.2: *Energy scale (in eV) for Coulomb (U), spin-orbit (H_{SO}), crystal-field (H_{CF}), and exchange (H_{exch}) interactions for actinides and lanthanides.*

The localized f electron state can be described by treating the synthesized angular momentum $\boldsymbol{J} = \boldsymbol{L} + \boldsymbol{S}$ as a good quantum number. According to the Hund-rule and the energy splitting caused by the spin-orbit coupling, each ground J multiplets of the f electron are determined as follows. For uranium in the tetra-valent state with $(5f)^2$, ${}^3H_4$ is the ground J multiplet with a ninefold degeneracy, and in the tri-valent state with $(5f)^3$, ${}^4I_{\frac{9}{2}}$ is the ground J multiplet with a tenfold degeneracy.

The tetragonal-crystalline-electric field is considered for these ground J multiplets, because all samples used in this study have the tetragonal symmetry. The most general operator-equivalent potential in tetragonal-point-charge symmetry can be written as

$$\mathcal{H}_{CEF} = B_2^0O_2^0 + B_4^0O_4^0 + B_4^4O_4^4 + B_6^0O_6^0 + B_6^4O_6^4, \tag{5.3}$$

where

$$
\begin{aligned}
O_2^0 &= 3J_z^2 - J(J+1), \\
O_4^0 &= 35J_z^4 - [30J(J+1) - 25]J_z^2 - 6J(J+1) + 3J^2(J+1)^2, \\
O_4^4 &= \frac{1}{2}\left(J_+^4 + J_-^4\right), \\
O_6^0 &= 231J_z^6 - 105[3J(J+1) - 7]J_z^4 \\
&\quad + \left[105J^2(J+1)^2 - 525J(J+1) + 294\right]J_z^2 \\
&\quad - 5J^3(J+1)^3 + 40J^2(J+1)^2 - 60J(J+1), \\
O_6^4 &= \frac{1}{4}\left[11J_z^2 - J(J+1) - 38\right]\left(J_+^4 + J_-^4\right) \\
&\quad + \frac{1}{4}\left(J_+^4 + J_-^4\right)\left[11J_z^2 - J(J+1) - 38\right],
\end{aligned}
$$

where B_n^m are the CEF parameters and have a dimension of the energy. O_n^m are the Stevens equivalent operators [21, 22].

The energy splittings of the J multiplet $^3H_4$ and $^4I_{\frac{9}{2}}$ are shown in Fig. 5.15 and 5.16, respectively. The wave functions of the CEF eigenstate of the J multiplet $^3H_4$ are expressed as follows.

$$
\begin{aligned}
\Gamma_3 : \quad |\Gamma_{t3}\rangle &= \frac{1}{\sqrt{2}}|-2\rangle + \frac{1}{\sqrt{2}}|+2\rangle, \\
\Gamma_3 : \quad |\Gamma_{t1}^{(2)}\rangle &= \frac{\gamma}{\sqrt{2}}|-4\rangle - \epsilon\sqrt{2}\,|0\rangle + \frac{\gamma}{\sqrt{2}}|+4\rangle, \\
\Gamma_4 : \quad |\Gamma_{t2}\rangle &= \frac{1}{\sqrt{2}}|-4\rangle - \frac{1}{\sqrt{2}}|+4\rangle, \\
\Gamma_4 : \quad |\Gamma_{t5}^{(1)}\rangle &= \alpha|\pm 3\rangle + \beta|\mp 1\rangle. \\
\Gamma_1 : \quad |\Gamma_{t1}^{(1)}\rangle &= \epsilon|-4\rangle + \gamma|0\rangle + \epsilon|+4\rangle, \\
\Gamma_5 : \quad |\Gamma_{t4}\rangle &= \frac{1}{\sqrt{2}}|-2\rangle - \frac{1}{\sqrt{2}}|+2\rangle, \\
\Gamma_5 : \quad |\Gamma_{t5}^{(2)}\rangle &= \beta|\pm 3\rangle - \alpha|\mp 1\rangle.
\end{aligned} \tag{5.4}
$$

The wave functions of the CEF eigenstate of the J multiplet $^4I_{\frac{9}{2}}$ are expressed as follows.

$$
\begin{aligned}
\Gamma_6 : \quad |\Gamma_{t\gamma}\rangle &\equiv \epsilon_1\left|\mp\frac{9}{2}\right\rangle + \epsilon_2\left|\mp\frac{1}{2}\right\rangle + \epsilon_3\left|\pm\frac{7}{2}\right\rangle, \\
\Gamma_8^{(2)} : \quad \left|\Gamma_{t\beta}^{(2)}\right\rangle &\equiv \delta_1\left|\mp\frac{5}{2}\right\rangle + \delta_2\left|\pm\frac{3}{2}\right\rangle, \\
\Gamma_8^{(2)} : \quad |\Gamma_{t\alpha}^{(2)}\rangle &\equiv \gamma_1\left|\mp\frac{9}{2}\right\rangle + \gamma_2\left|\mp\frac{1}{2}\right\rangle + \gamma_3\left|\pm\frac{7}{2}\right\rangle, \\
\Gamma_8^{(1)} : \quad \left|\Gamma_{t\beta}^{(1)}\right\rangle &\equiv \beta_1\left|\mp\frac{5}{2}\right\rangle + \beta_2\left|\pm\frac{3}{2}\right\rangle, \\
\Gamma_8^{(1)} : \quad |\Gamma_{t\alpha}^{(1)}\rangle &\equiv \alpha_1\left|\mp\frac{9}{2}\right\rangle + \alpha_2\left|\mp\frac{1}{2}\right\rangle + \alpha_3\left|\pm\frac{7}{2}\right\rangle.
\end{aligned} \tag{5.5}
$$

The matrix elements are calculated from the eigenstates by using the operator J_z and J_x.

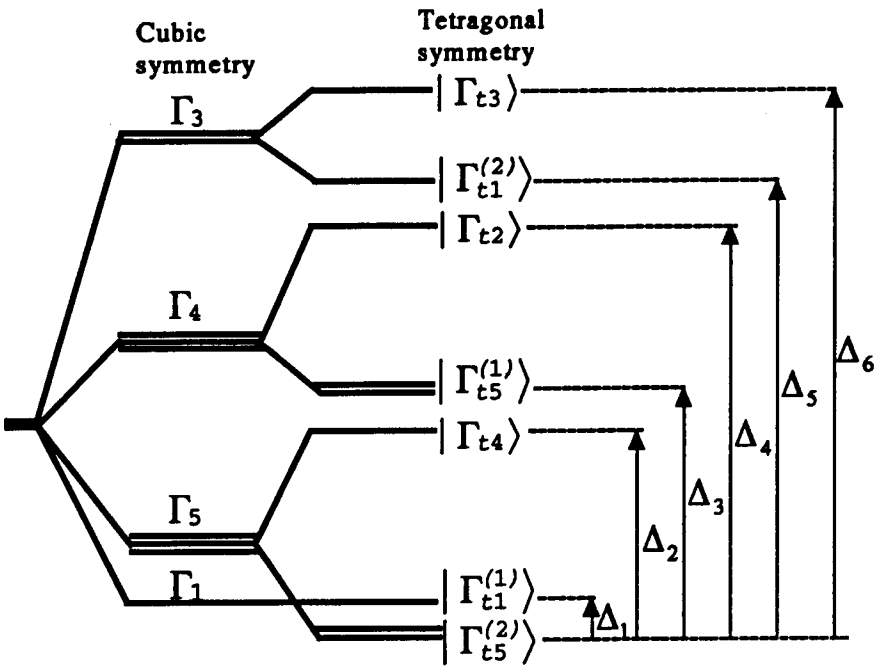

Figure 5.15: *Energy split of the tetragonal CEF for* $J = 4$.

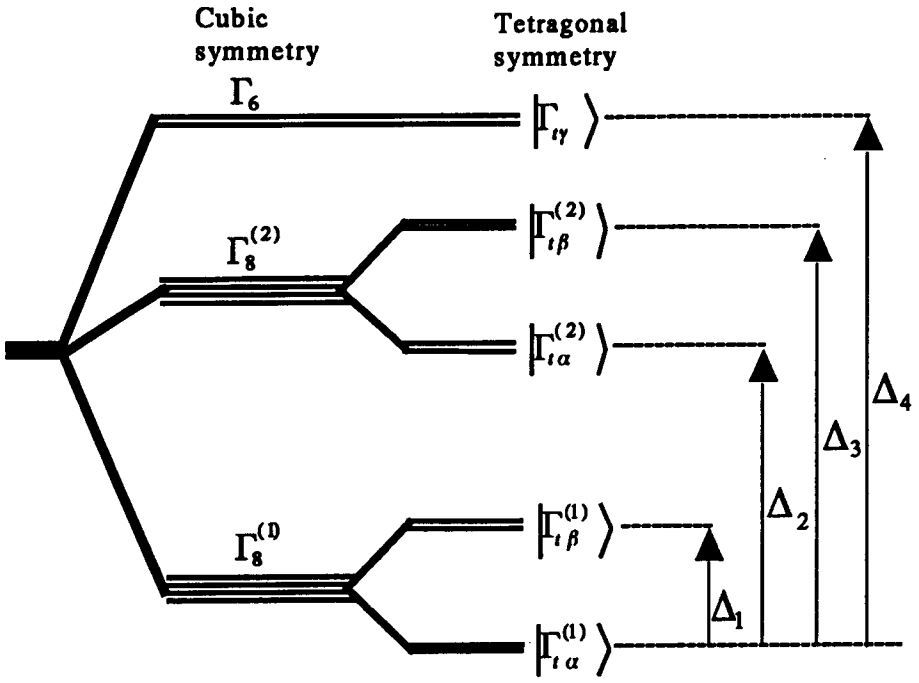

Figure 5.16: *Energy split of the tetragonal CEF for* $J = \frac{9}{2}$.

The magnetic susceptibility is calculated from the matrix elements by regarding the external field as a perturbation. The Hamiltonian with the external field along the i axis is given by

$$\mathcal{H} = \mathcal{H}_0 - g_J \mu_B J_i H, \tag{5.6}$$

where g_J is the Landé's g factor and $\mathcal{H}_0$ is the CEF Hamiltonian. The general formula of the magnetic susceptibility is expressed as

$$\chi = \frac{N(g_J\mu_B)^2}{Z^0} \sum_n \left[\sum_{m(lf)} \frac{|\langle m|J_i|n\rangle|^2}{kT} + 2 \sum_{m(hf)} \frac{|\langle m|J_i|n\rangle|^2}{E_m^0 - E_n^0} \right] e^{-E_n^0/kT}, \tag{5.7}$$

where

$$\mathcal{H}_0|n\rangle = E_n^0|n\rangle, \tag{5.8}$$

$$Z^0 = \sum_n e^{-E_n^0/kT}, \tag{5.9}$$

$$E_m^0 = E_n^0 \quad \text{in the summation of} \quad \sum_{m(lf)},$$

$$E_m^0 \neq E_n^0 \quad \text{in the summation of} \quad \sum_{m(hf)}.$$

The magnetic susceptibility along the c and a axes are calculated by substituting $\langle m|J_z|n\rangle$ and $\langle m|J_x|n\rangle$ for $\langle m|J_i|n\rangle$, respectively. The fitting parameters are the energy splitting Δ_i between the ground and excited state

$$\Delta_i = E_n^0 - E_0^0 \tag{5.10}$$

and the coefficients of the wave functions, *i.e.*, α, β, γ, ε, *etc.*. The parameters are determined by fitting the experimental results.

The magnetization can be calculated by diagonalizing the total Hamiltonian given by Eq. 5.6 regarding the CEF eigenstate as a non-perturbative normalized-orthogonal system. The magnetization along the i axis is calculated by using the eigenvalue E_α and eigenstate $|\alpha\rangle$ of the total Hamiltonian as follows.

$$M_i = \frac{g_J\mu_B}{Z} \sum_\alpha \langle\alpha|J_i|\alpha\rangle\, e^{-E_\alpha/kT}, \tag{5.11}$$

where

$$\mathcal{H}|\alpha\rangle = E_\alpha|\alpha\rangle, \tag{5.12}$$

$$Z = \sum_\alpha e^{-E_\alpha/kT}. \tag{5.13}$$

The contribution of the CEF to the specific heat is calculated from the definition of the internal energy as follows.

$$C_V \equiv \left(\frac{\partial U}{\partial T}\right)_V \tag{5.14}$$

$$= \frac{\partial}{\partial T}\left(\frac{kT^2}{Z^0}\frac{\partial Z^0}{\partial T}\right)_V, \tag{5.15}$$

where Z^0 is the partition function of the CEF Hamiltonian defined as Eq. 5.9. This specific heat is expressed by the Schottky formula as follows.

$$C_V = \frac{1}{kT^2 Z^0}\left[\sum_n (E_n^0)^2 e^{-E_n^0/kT}\right] - \frac{1}{kT^2}\left[\frac{1}{Z^0}\sum_n E_n^0 e^{-E_n^0/kT}\right]. \tag{5.16}$$

5.3.2 Crystalline-electric-field model

As seen in Fig. 5.1 and 5.4, the magnetic susceptibility along the c axis increases even at the lowest temperature, in contrast with the temperature dependence in URu_2Si_2. This behavior and the temperature dependence of the susceptibility at high temperatures can not be explained by the singlet-ground-state CEF model with the first excited energy of about 40 K which is proposed for URu_2Si_2 [7, 9]. This suggests that the ground state has a degeneracy, because the calculations with the singlet-ground-state CEF model gives the constant value of the susceptibility at low temperatures. Therefore, a singlet is eliminated from the candidate of the ground state. However, the calculated susceptibility for $J = 9/2$ along the a axis has a Curie-law term proportional to $1/T$ and the temperature dependence of the susceptibility can not be explained by using the ground multiplet ${}^4I_{\frac{9}{2}}$. If a tetravalent state with $J = 4$ is assumed [16], the two degenerate ground states, $\Gamma_{t5}^{(2)}$ and $\Gamma_{t5}^{(1)}$, give a good fit to the data. Here after, we discuss the CEF effect with $\Gamma_{t5}^{(2)}$ ground state, because $\Gamma_{t5}^{(1)}$ and $\Gamma_{t5}^{(2)}$ lead to the similar results.

The dashed lines in Fig. 5.17 are the best fitting results of the CEF calculation to the experimental data. The contribution of $5f$ electrons is obtained by subtracting the data of $LaRu_2Si_2$. The CEF splitting determined here is as follows. The ground state is the magnetic non-Kramers doublet with the strong Ising property and the first excited state is the non-magnetic singlet located at 60 ± 6 K. This exciting energy is required to explain the Schottky anomaly in the specific-heat data. The wave functions of the ground and first excited states are $\Gamma_{t5}^{(2)}$ and $\Gamma_{t1}^{(1)}$ (or $\Gamma_{t5}^{(1)}$ and $\Gamma_{t1}^{(2)}$), respectively. The definition of the wave functions is expressed in the paper of Nieuwenhuys [7]. The J_x matrix element between these two states is very small, so that this energy splitting could not be determined by the CEF fitting calculation for the susceptibility data. The other singlets are determined to be located at about 10^3 K above the ground state. The J_x matrix element between $\Gamma_{t5}^{(2)}$ (or $\Gamma_{t5}^{(1)}$) and the other singlets are not so small, so that the energy splitting should be large to realize the small constant value of the calculated susceptibility along the a axis. There is a Curie-law term in the calculated susceptibility along the c axis, while there is no such term in that along the a axis. As shown in Fig. 5.17, the calculated susceptibilities agree well with the experimental results in the temperature region above 100 K. However, the experimental result along the c axis deviates from the calculated susceptibility below about 100 K, where the experimental value is suppressed smaller than the calculated one.

The fitting curves used in Fig. 5.17 are compared with the susceptibility data of the various uranium concentration to study the effect of the RKKY interaction. As shown in Fig. 5.18, this fitting curve also fits well to the susceptibilities of 7 and 15 % uranium compounds above 100 K. On the other hand, at low temperatures below 25 K, the suscepti-

bilities of these three compounds largely deviate from the calculated one. These deviations can not be explained by only the onset of the RKKY interaction effect. The Curie-Weiss constant $\Theta = -11 \pm 1$ K is obtained for the samples with $x = 0.05$, 0.07 and 0.15, and it is independent on the uranium concentration. The RKKY interaction has only a minor effect on the suppression of the susceptibility in the samples with $x \leq 0.15$. This difference between the experimental data and the fitting curve indicates that the single-site screening of the localized magnetic moment is the major effect on the suppression of the susceptibility in this dilute system.

The calculated magnetization curves using the same parameters are compared to the experimental magnetization data (see Fig. 5.19). The calculated curves agree well with the experimental results at 77 and 300 K. However, the experimental value at 4.3 K is much smaller than the calculated value. Moreover the theoretical line is qualitatively different from the experimental data. The dashed line in Fig. 5.20 shows the calculated magnetization based on the CEF model using the same fitting parameters for the high-temperature susceptibility. The saturated moment along the c axis is estimated to be about $1.8\mu_B$ by this CEF fitting. This value is almost the same as that obtained from the high-field magnetization measurement on URu_2Si_2[23]. The large anisotropic g values seen in Fig. 5.17 are averaged by integrating the direction cosine to the magnetic field. The calculated magnetization shows a saturation at about 15 T, which is quite different from the experimental data (solid line). This means that at low temperatures, the CEF model is not valid to understand the magnetic properties.

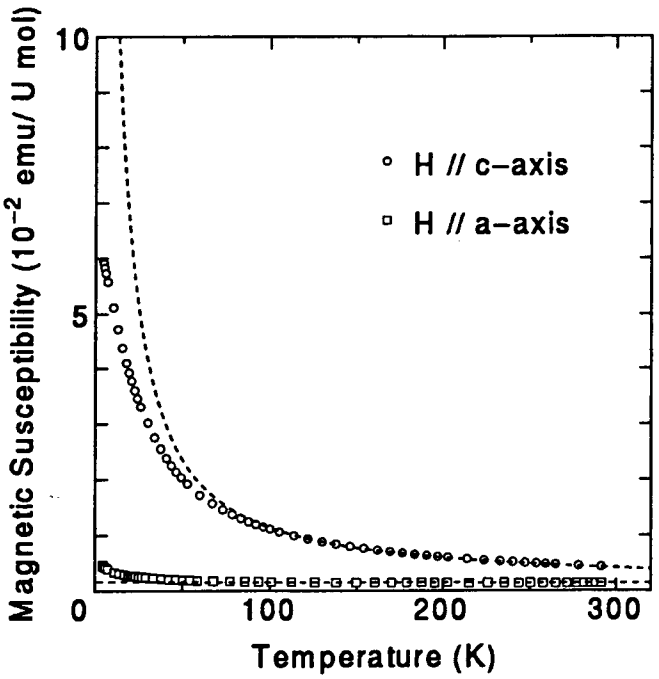

Figure 5.17: *Temperature dependence of the magnetic susceptibility of $(U_{0.05}La_{0.95})Ru_2Si_2$ along the c and a axes. The dashed lines show the temperature dependence of the calculated magnetic susceptibility based on the CEF model.*

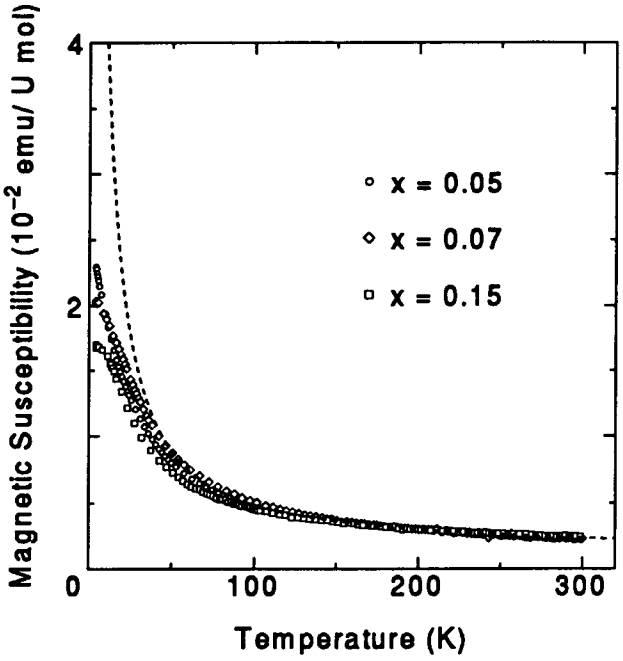

Figure 5.18: *Temperature dependence of the magnetic susceptibilities of* $(U_xLa_{1-x})Ru_2Si_2$ *(*x *= 0.05, 0.07, and 0.15). The dashed line shows the temperature dependence of the calculated magnetic susceptibility based on the CEF model.*

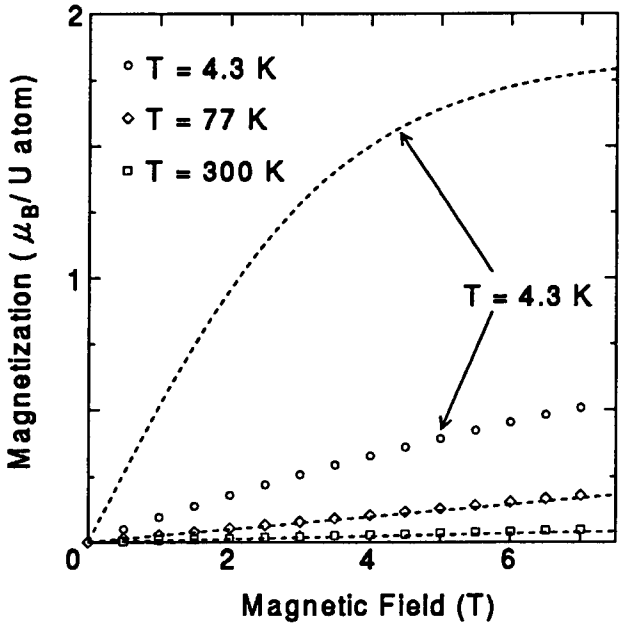

Figure 5.19: *Magnetization curves of* $(U_{0.05}La_{0.95})Ru_2Si_2$ *along the c axis at various temperatures. The dashed lines show the magnetization curves along the c axis at various temperatures calculated by the CEF model.*

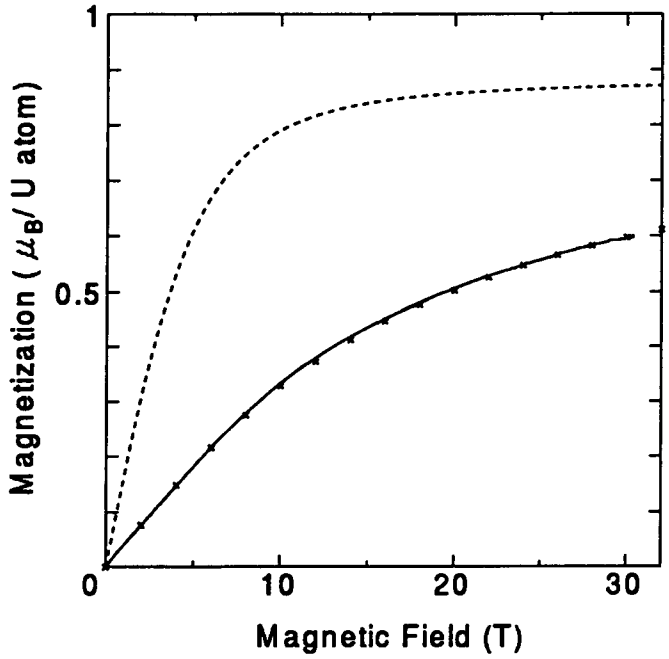

Figure 5.20: *High-field magnetization curve of $(U_{0.15}La_{0.85})Ru_2Si_2$ at 4.2 K. The dashed line and the crosses show the magnetization curves calculated by the CEF and Kondo model, respectively.*

5.3.3 Kondo model

The Kondo model is used to explain the single-site screening of the localized magnetic moment which is seen in the susceptibility and magnetization at low temperatures. The experimental results are compared with the exact Bethe-ansatz results in Schlottman's review article [24]. The fitting calculation is made for the $S = 1/2$ case, because the CEF ground state is considered to be a doublet. The fitting parameter is the Kondo temperature.

The fitting result of the magnetization data is given by the crosses in Fig. 5.20. The Kondo model [25] is applied to only the magnetization calculation along the c axis, because the susceptibility along the a axis is negligibly small compared with that along the c axis and the screening is detected only for the c axis susceptibility. The saturated moment used in this fitting is the same as that used in the CEF calculation. The Kondo temperature $T_{K,M}$ is estimated to be 13 ± 2 K in the definition by Desgranges and Schotte [26]. The lower index of M denotes that this Kondo temperature is estimated from the magnetization data. The magnetization calculated by the Kondo model agrees fairly well with the experimental results over the whole range of the measurement.

The magnetic susceptibility is also fitted by the Kondo model using the same parameters [27]. The calculated susceptibility of this model has a finite value at zero temperature and the overall behavior of this fitting quantitatively agrees with the experimental results over the whole temperature range as seen in Fig. 5.21. This is more clearly seen in the plots

of $-Td\chi/dT$ as a function of the temperature (see Fig. 5.22). The value of this plot is that it eliminates the constant component of the susceptibility, leaves the term of $1/T$ unchanged, and converts the term of $\ln T$ to a constant. The magnetic susceptibility of $(U_{0.15}La_{0.85})Ru_2Si_2$ was measured by using the powdered sample, but for $x = 0.05$ and 0.07, the susceptibility data as the powdered sample are obtained by averaging the data for the single crystals. The temperature dependence of the susceptibilities for the single crystal and powdered sample are the same each other except for the absolute value, because the susceptibility along the a axis is constant. As is seen in Fig. 5.22, the experimental data show almost no uranium concentration dependence, reach a maximum at around 25 K, and decrease in the low temperature region. The susceptibility increases more steeply than the slope of $-\ln T$ above 25 K while it increases weakly below 25 K. It becomes nearly constant below about 10 K as shown in Fig. 5.4, which means the formation of the Kondo singlet state. The solid line in Fig. 5.22 shows the fitting result for the susceptibility by using the Kondo model, which traces well the experimental data. On the other hand, the susceptibility calculated by the CEF model, which is indicated by the dashed line, deviates from the experimental value below 100 K, because this CEF model has a susceptibility with the term of $1/T$. These analyses have ignored the effect of the interactions between the dilute magnetic moments, because $-Td\chi/dT$ vs T plots are almost independent of the uranium concentration.

The experimental data of the electronic-specific heat at low temperatures are also fitted qualitatively well by the calculation which takes account of both the Kondo model [26, 28] and the CEF splitting. The fitting results are shown by the lines in Fig. 5.23. The dash-dotted and dashed lines show the specific heat calculated by the Kondo model and the CEF splitting, respectively. The solid line shows the total calculated specific heat. The Kondo temperature $T_{K,C}$ is estimated to be 67 ± 10 K. The lower index of C denotes that this Kondo temperature is estimated from the specific heat data. The CEF excitation energy Δ is determined to be 60 ± 6 K. From these results, it is concluded that the Kondo behavior does exist in the dilute uranium system $(U_xLa_{1-x})Ru_2Si_2$ and the Kondo screening reduces the magnetic moment of the uranium atom at low temperatures. Moreover, the observation of the enhanced γ value is the evidence to show that the ground state of the $5f$ electrons at low temperatures is the Kondo singlet state described as the Fermi liquid [29].

As shown in Fig. 5.13, the electrical resistivity increases with increasing temperature. There is no $-\ln T$ dependence of the resistivity. Although the magnetic contribution to the resistivity is estimated by subtracting the lattice contribution using the resistivity of $LaRu_2Si_2$, its magnetic resistivity apparently increase with increasing temperature as shown in Fig. 5.24. This increase does occur whether a constant factor to the resistivity of $(U_{0.07}La_{0.93})Ru_2Si_2$ is modified or not. The T^2 law of the resistivity is observed in the low temperature region as shown in Fig. 5.25. If the modified resistivity shown in Fig. 5.13 are used to the fitting, the coefficient A of the T^2 term is positive and the values with the current parallel to the a and c axes are estimated to be about 6.6×10^{-3} and 5.0×10^{-3} $\mu\Omega$ cm/K^2, respectively.

This resistivity behavior, however, does not contradict with the Kondo screening. Fis-

cher mentioned that some dilute alloys such as RhFe, which impurity resistivity increases with increasing temperature, are probably the Kondo systems with temperature dependent transport properties characteristic of the Wolff model [30]. According to this review, the coefficient of the T^2 contribution to the resistivity might be positive or negative. Traditionally, a decreasing resistivity with increasing temperature has been described by the Anderson or Kondo models, and an increasing resistivity with increasing temperature has been described by the Wolff model which considers the local-spin fluctuation (LSF). This rule is not without exception, since a sufficiently large shift of the impurity level with respect to the Fermi energy leads to a change in sign of the T^2 term [31]. The Kondo and LSF systems exhibit the same power laws at low temperatures in all physical properties and show the same thermal and magnetic properties. For example, above the characteristic temperature, the Kondo temperature (T_K) and the local-spin-fluctuation temperature (T_*), the impurities are magnetic, that is, they behave as if they possess a well defined moment. Therefore, the data of the resistivity may be thought to show the behavior of the Kondo system [32].

The Kadowaki-Woods ration A/γ^2 is used in the next formula of the impurity contribution ${A_{\rm imp}}/{\gamma_{\rm imp}}^2$, where $A_{\rm imp}$ is the coefficient of the T^2 term of the magnetic resistivity per molar uranium, and $\gamma_{\rm imp}$ is the electronic-specific-heat coefficient per molar uranium. The value of ${A_{\rm imp}}/{\gamma_{\rm imp}}^2$ with the current parallel to the a axis is estimated to be about 0.35×10^{-5} $\mu\Omega$ cm (U mol K/mJ)^2/U which order is the same as the common value of 1.0×10^{-5} $\mu\Omega$ cm (mol K/mJ)^2 for all of the heavy fermion compounds including URu_2Si_2 [33]. The similarity of these values between the dilute uranium system $(U_xLa_{1-x})Ru_2Si_2$ and URu_2Si_2 suggests that the Kondo resonance enhances the density of states at the Fermi level and it contributes the scattering of the conduction electron which causes the T^2 dependence of the resistivity.

Another contribution to the increasing resistivity will be the CEF effect. As seen in Fig. 5.13, the data with the current parallel to the both axes show a broad rounded curvature at around 200 K. Similar behavior has been observed in the magnetic resistivity of $CeRu_2Si_2$, which is considered to be resulted from the CEF effect [19]. As mentioned in the experimental results, the data along the both axes show a kink at about 18 K. The specific heat measurement indicates the CEF splitting of 60 ± 6 K and the CEF effect may be appeared in the resistivity, because the spin-disorder magnetic resistivity is considered to decrease when the CEF degeneracy decreases as temperature decreases. Anyway, the further investigation for the resistivity of the sample with lower uranium concentration and the resistivity in the magnetic field is needed to study the transport properties observed in $(U_{0.07}La_{0.93})Ru_2Si_2$.

The difference of the Kondo temperature between $T_{K,C}$ and $T_{K,M}$ obtained from the specific heat and from the magnetization and susceptibility is caused by the difference of the Wilson ratio for the dilute uranium system $(U_xLa_{1-x})Ru_2Si_2$ and the exact solution of the $S = 1/2$ Kondo model. If the Wilson ratio formula $(\chi_{\rm imp}/{g_J}^2 J(J+1){\mu_B}^2)/(\gamma_{\rm imp}/\pi^2{k_B}^2)$ with $J = 4$ is used, the Wilson ratio of our system is estimated to be about 8.5 which is different from the value of 2 obtained from the exact solution of the $S = 1/2$ Kondo

model. The Wilson ratio of 2 is obtained by the exact calculation for the isotropic $S = 1/2$ Kramers-doublet ground-state system. Our system is the Ising-type non-Kramers-doublet ground-state system, and it is not necessary that the Wilson ratio of our system should be 2. If the difference of the Wilson ratio is considered, $T_{K,M}$ is modified to be 55.3 ± 8.5 K by a factor of 8.5/2. The modified value of $T_{K,M}$ is fairly the same value as $T_{K,C}$. Therefore, T_K may be adjusted to fit the experimental results of the specific heat and the susceptibility, because the $S = 1/2$ Kondo model is used. The exact calculation of the thermodynamics properties for the system with the doublet-singlet CEF splitting has not yet been performed.

As mentioned in the Introduction, the study of the dilute uranium compounds $(U_xTh_{1-x})Ru_2Si_2$ ($x \leq 0.07$) suggests the possibility of the two-channel Kondo effect [16, 17]. According to their work, the CEF ground state is the same as that obtained in the present study. However, C_{5f}/T increases logarithmically and does not approach a constant value. Moreover the specific heat show no Schottky anomaly. These results are quite different from those of URu_2Si_2 and are considered to be a non-Fermi-liquid behavior. On the other hand, the present results show the similarity of the γ value and Schottky anomaly between the dilute uranium system $(U_xLa_{1-x})Ru_2Si_2$ and URu_2Si_2. Therefore, we suspect that the present results indicate the fundamental interactions important for URu_2Si_2. The difference between $(U_xLa_{1-x})Ru_2Si_2$ and $(U_xTh_{1-x})Ru_2Si_2$ may be explained by the shift of the singlet excited-energy level. The theoretical study shows that the singlet excited state plays an important role in stabilizing the Fermi-liquid state over the non-Fermi-liquid state [34].

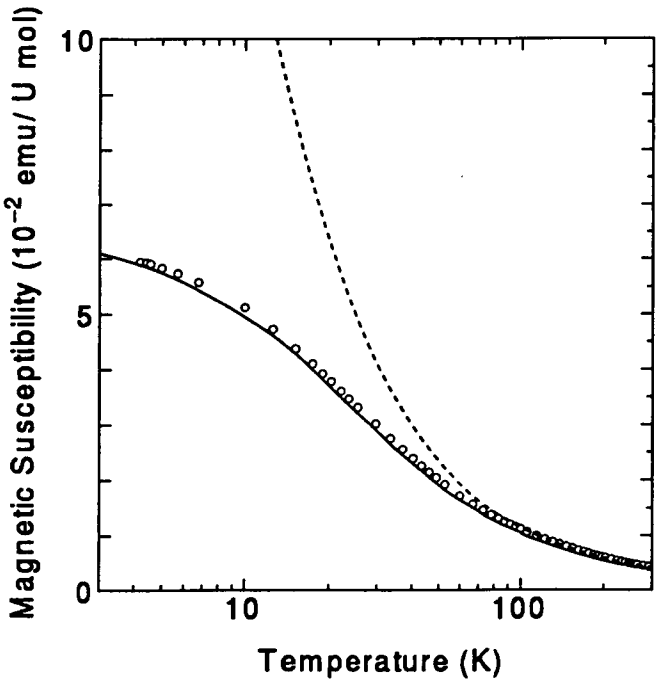

Figure 5.21: *Magnetic susceptibility of $(U_{0.05}La_{0.95})Ru_2Si_2$ along the c axis in the logarithmic temperature scale. The dashed and solid lines show the magnetic susceptibilities calculated by the CEF and Kondo model calculations, respectively.*

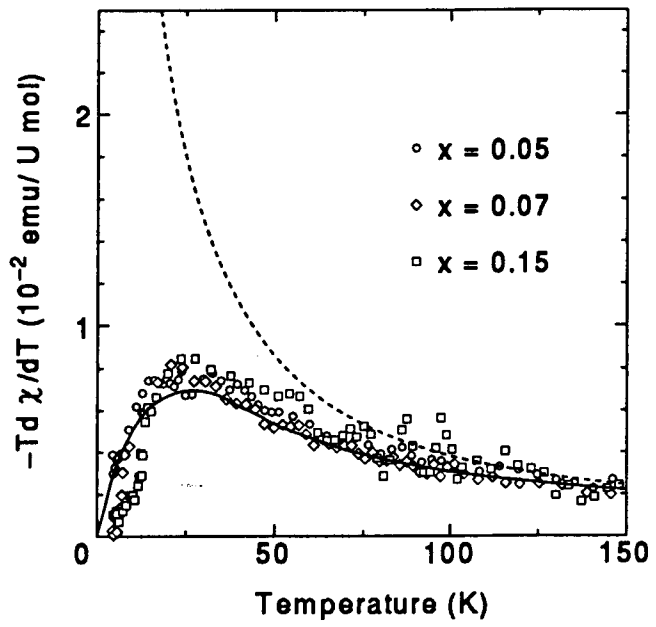

Figure 5.22: *Temperature dependence of the $-Td\chi/dT$ plots of $(U_xLa_{1-x})Ru_2Si_2$ ($x = 0.05$, 0.07, and 0.15). The dashed and solid lines show the CEF and Kondo model calculations, respectively.*

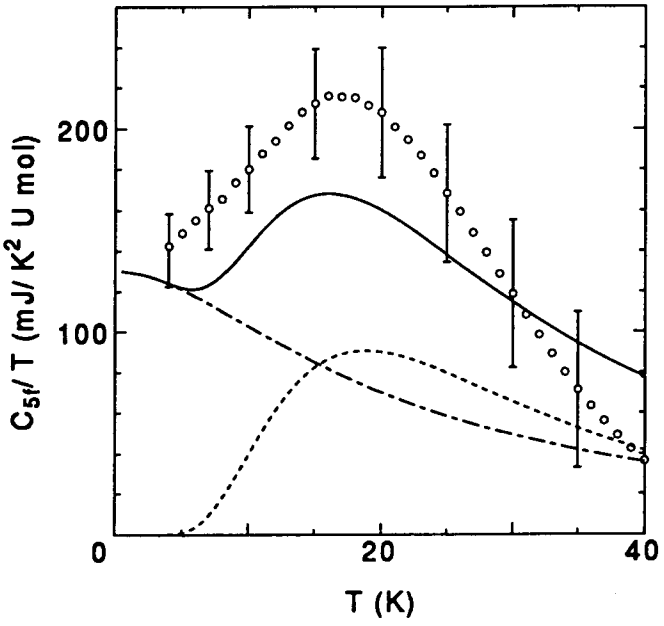

Figure 5.23: *C_{5f}/T vs T plot of the electronic-specific heat of $(U_{0.15}La_{0.85})Ru_2Si_2$. The dash-dotted and dashed lines show the specific heat calculated by the Kondo model and the CEF splitting, respectively. The solid line shows the total calculated specific heat using the Kondo model and the CEF splitting.*

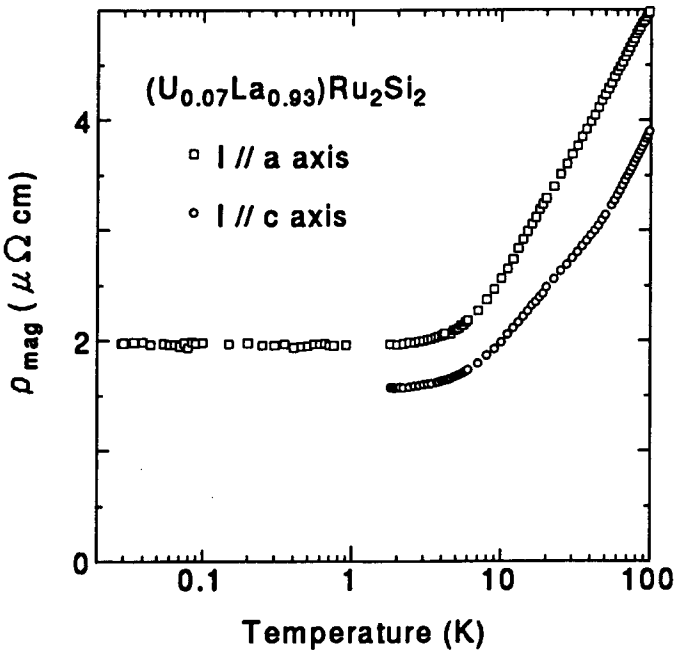

Figure 5.24: *Magnetic resistivity of $(U_{0.07}La_{0.93})Ru_2Si_2$ with the current parallel to the c and a axes in the logarithmic-temperature scale.*

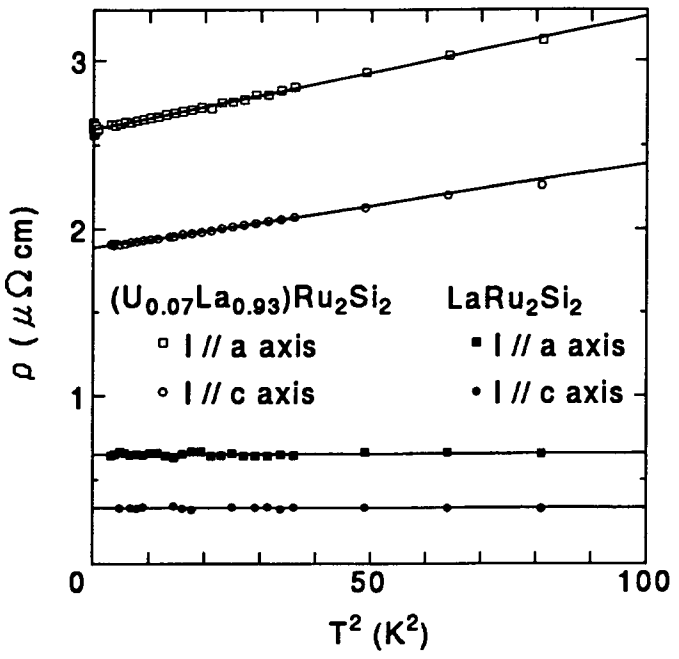

Figure 5.25: *ρ vs T^2 plots of the electrical resistivities of $(U_{0.07}La_{0.93})Ru_2Si_2$ and $LaRu_2Si_2$ with the current parallel to the c and a axes.*

5.4 Conclusion

We have analyzed the magnetic, thermodynamical, and transport properties of the dilute uranium compound system $(U_xLa_{1-x})Ru_2Si_2$ ($x \leq 0.15$) by the crystalline-electric-field (CEF) and Kondo models. In the high-temperature region above 100 K, the CEF model is a good picture. It can explain the large uniaxial anisotropy of the magnetic susceptibility and magnetization and the temperature dependence of the susceptibility at high temperatures. The CEF scheme is the non-Kramers doublet ground state and the singlet first excited state with the CEF splitting of 60 ± 6 K. This CEF splitting is determined by the Schottky anomaly in the specific heat.

However, the single-site screening of the magnetic moment is observed at low temperatures and it can not be explained by the CEF model. This screening can be explained by the Kondo model. The Kondo model shows a good agreement with the experimental data. This means that there is the single-site Kondo screening of the uranium atom and the Fermi-liquid state occurs at low temperatures. The γ value ($= C_{5f}/T$) is estimated to be 130 ± 20 mJ/K^2 U mol. The Kondo temperature is estimated to be 67 ± 10 K from the specific-heat data by using the $S = 1/2$ Kondo model. The Schottky anomaly of the specific heat is observed and the experimental data show a broad maximum at around 25 K. The γ value and Schottky anomaly are nearly the same as those observed for URu_2Si_2. From these results, it is suggested that the single-site Kondo screening is important for understanding the Fermi-liquid state in URu_2Si_2. Further study on the samples with more uranium concentration is necessary to clarify the role of the RKKY interaction in the formation process of the heavy-fermion state in URu_2Si_2.

Bibliography

[1] M.B. Maple, J.W. Chen, Y. Dalichaouch, T. Kohara, C. Rossel, M.S. Torikachvili, M.W. McElfresh, and J.D. Thompson, Phys. Rev. Lett. **56**, 185 (1986).

[2] T.T.M. Palstra, A.A. Menovsky, J.van den Berg, A.J. Dirkmaat, P.H. Kes, G.J. Nieuwenhuys, and J.A. Mydosh, Phys. Rev. Lett. **55**, 2727 (1985).

[3] C. Broholm, J.K. Kjems, W.J.L. Buyers, P. Matthews, T.T.M. Palstra, A.A. Menovsky, and J.A. Mydosh, Phys. Rev. Lett. **58**, 1467 (1987).

[4] E.D. Isaacs, D.B. McWhan, R.N. Kleiman, D.J. Bishop, G.E. Ice, P. Zschack, B.D. Gaulin, T.E. Mason, J.D. Garrett, and W.J.L. Buyers, Phys. Rev. Lett. **65**, 3185 (1990).

[5] T.E. Mason, B.D. Gaulin, J.D. Garrett, Z. Tun, W.J.L. Buyers, and E.D. Isaacs, Phys. Rev. Lett. **65**, 3189 (1990).

[6] C. Broholm, H. Lin, P. Matthews, T.E. Mason, W.J.L. Buyers, M.F. Collins, A.A. Menovsky, J.A. Mydosh, and J.K. Kjems, Phys. Rev. B **43**, 12 809 (1991).

[7] G.J. Nieuwenhuys, Phys. Rev. B **35**, 5260 (1987).

[8] R. Konno, Prog. Theor. Phys. **89**, 51 (1993).

[9] P. Santini and G. Amoretti, Phys. Rev. Lett. **73**, 1027 (1994).

[10] M.W. McElfrsh, J.D. Thompson, J.O. Willis, M.B. Maple, T. Kohara and M.S. Torikachvili, Phys. Rev. B **35**, 43 (1987).

[11] S.A.M. Mentink, T.E. Mason, S. Süllow, G.J. Nieuwenhuys, A.A. Menovsky, J.A. Mydosh, and J.A.A.J. Perenboom, Phys. Rev. B **53**, R6014 (1996).

[12] K. Marumoto, T. Takeuchi, T. Taniguchi and Y. Miyako, Physica B **206-207**, 519 (1995).

[13] K. Marumoto, T. Takeuchi, and Y. Miyako, Phys. Rev. B **54**, 12 194 (1996).

[14] Y. Miyako, T. Kuwai, T. Taniguchi, S. Kawarazaki, H. Amitsuka, C.C. Paulsen, and T. Sakakibara, J. Magn. Magn. Mater. **108**, 190 (1992).

[15] Y. Miyako, H. Amitsuka, S. Kawarazaki, T. Taniguchi, and T. Sikama, *Physical Properties of Actinide and Rare Earth Compounds*, JJAP Series 8, (Jpn. J. Appl. Phys., Tokyo, 1993) p. 230.

[16] H. Amitsuka, T. Hidano, T. Honma, H. Mitamura, and T. Sakakibara, Physica B **186-188**, 337 (1993).

[17] H. Amitsuka and T. Sakakibara, J. Phys. Soc. Jpn. **63**, 736 (1994).

[18] S.B. Roy and B.R. Coles, J. Magn. Magn. Mater. **108**, 43 (1992).

[19] F. Lapierre and P. Haen, J. Magn. Magn. Mater. **108**, 167 (1992).

[20] J.-M. Fournier and R. Troć, *Handbook on the Physics and Chemistry of the Actinides*, edited by A.J. Freeman and G.H. Lander (North-Holland, Amsterdam, 1985) Vol. 2, p. 29.

[21] K.R. Lea, M.J.M. Leask, and W.P. Wolf, J. Phys. Chem. Solids **23**, 1381 (1962).

[22] G. Amoretti, A. Blaise, and J. Mulak, J. Magn. Magn. Mater. **42**, 65 (1984).

[23] K. Sugiyama, H. Fuke, K. Kindo, K. Shimohata, A.A. Menovsky, J.A. Mydosh, and M. Date, J. Phys. Soc. Jpn. **59**, 3331 (1990).

[24] P. Schlottmann, Phys. Report **181**, 1 (1989).

[25] V.T. Rajan, J.H. Lowenstein and N. Andrei, Phys. Rev. Lett. **49**, 497 (1982).

[26] H.U. Desgranges and K.D. Schotte, Phys. Lett. **91A**, 240 (1982).

[27] V.T. Rajan, Phys. Rev. Lett. **51**, 308 (1983).

[28] L.N. Oliveira and J.W. Wilkins, Phys. Rev. Lett. **47**, 1553 (1981).

[29] K. Yamada, Prog. Theor. Phys. **53**, 970 (1975).

[30] K.H. Fischer, Phys. Report **47**, 225 (1978).

[31] K.H. Fischer, J. Low Temp. Phys. **17**, 87 (1974).

[32] K. Marumoto, T. Takeuchi, Y. Miyako, M. Ocio, P. Pari, and J. Hammann, submitted to J. Magn. Magn. Mater.

[33] K. Kadowaki and S.B. Woods, Solid State Commun. **58**, 507 (1986).

[34] M. Koga and H. Shiba, J. Phys. Soc. Jpn. **64**, 4345 (1995).

Chapter 6

Comparative study with the dilute cerium compound system $(Ce_xLa_{1-x})Ru_2Si_2$

6.1 Introduction

As introduced in chapter 3, $CeRu_2Si_2$ is known as the paramagnetic heavy-fermion compound with the Kondo temperature $T_K = 24.4$ K. The lanthanum (La) doped compound $Ce_{1-x}La_xRu_2Si_2$ shows the magnetic order in the lanthanum-concentration range between $x = 0.08$ and 0.90. Magnetic structure changes from the pure-sine wave for $x = 0.13$ to the square wave for $x = 0.20$ as determined by the neutron-scattering measurement [1]. The μSR measurement has also been performed in this concentration region to study the variation of the magnetism from the itinerant-electron state to the localized-electron state with increasing the La concentration [2]. Antiferromagnetic ordering occurs also in the low cerium concentration region above $x = 0.7$ [3, 4]. However, the magnetism in this concentration region has not yet been investigated sufficiently.

The measurement on the dilute cerium compound system $(Ce_xLa_{1-x})Ru_2Si_2$ ($x \leq 0.10$) is performed to clarify the magnetic behavior in the lower-cerium-concentration region and the single-site properties of the cerium ion. It would be interesting to compare the single-site properties in $(Ce_xLa_{1-x})Ru_2Si_2$ with those in $(U_xLa_{1-x})Ru_2Si_2$ because both $CeRu_2Si_2$ and URu_2Si_2 compounds are known as a heavy-fermion system with different f electrons.

6.2 Experimental results

6.2.1 Magnetic susceptibility

The magnetic susceptibilities of the $(Ce_{0.05}La_{0.95})Ru_2Si_2$ and $LaRu_2Si_2$ single crystals along the c and a axes are shown in Fig. 6.1. It is noted that a large uniaxial magnetic anisotropy is observed for $(Ce_{0.05}La_{0.95})Ru_2Si_2$ as in $CeRu_2Si_2$. The susceptibility along the

c axis obeys the Curie-Weiss law at high temperatures, while the susceptibility along the a axis is small and almost constant except for a increase in the low-temperature region. The susceptibility of $LaRu_2Si_2$ is small and shows almost no temperature dependence. It shows a small constant negative and positive value in the field applied along the c and a axes, respectively, except for a small increase in the low-temperature region.

Figure 6.2 shows the magnetic susceptibilities of $(Ce_xLa_{1-x})Ru_2Si_2$ with various cerium concentrations of $x = 0.01$, 0.05, and 0.10 along the c and a axes. The contribution of $4f$ electrons is obtained by subtracting the susceptibility of $LaRu_2Si_2$. The low-temperature behavior of these susceptibility in the logarithmic-temperature scale are shown in Fig. 6.3. These data seem to show almost no cerium concentration dependence. Figure 6.4 shows the $\chi_{4f}T$ vs T plots of the magnetic susceptibilities of $x = 0.01$, 0.05, and 0.10 along the c axis. All data show an almost constant down to about 20 K in this plot and this means the existence of the localized electron described by the Curie law. The data below about 20 K, however, show the decrease of the $\chi_{4f}T$ plot. As discussed later, this behavior indicates either the screening of the localized magnetic moment or the antiferromagnetic correlation between the magnetic moments.

The modified Curie-Weiss law (Eq. 5.1) is used to fit the experimental result of the susceptibility. The fitting parameters for the dilute cerium system are listed in Table 6.1. The fitting-temperature range is determined to minimize the deviation of the least-square fit.

Ce %	μ_{eff} (μ_B)	Θ (K)	χ_0 (emu/U mol)	Fitting-temperature range
1 %	3.12	−0.81	-2.77×10^{-3}	$T \geq 20$ K
5 %	3.23	−3.90	-5.42×10^{-4}	$T \geq 20$ K
10 %	3.12	−0.81	-5.32×10^{-4}	$T \geq 26$ K

Table 6.1: *Fitting parameters of the modified Curie-Weiss law for the susceptibilities of $(Ce_xLa_{1-x})Ru_2Si_2$ ($x = 0.01$, 0.05, and 0.10) along the c axis.*

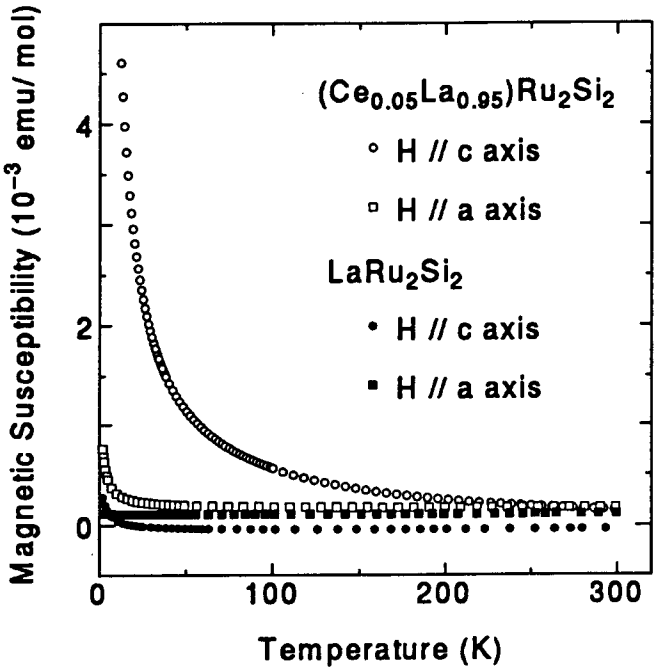

Figure 6.1: *Temperature dependence of the magnetic susceptibilities of* $(Ce_{0.05}La_{0.95})Ru_2Si_2$ *and* $LaRu_2Si_2$ *along the c and a axes.*

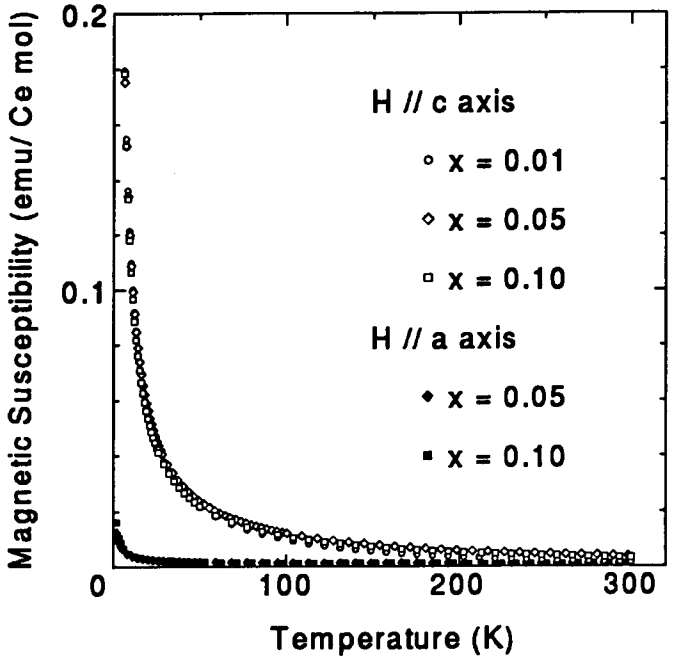

Figure 6.2: *Temperature dependence of the magnetic susceptibilities of* $(Ce_xLa_{1-x})Ru_2Si_2$ *(*x *= 0.01, 0.05, and 0.10) along the c and a axes.*

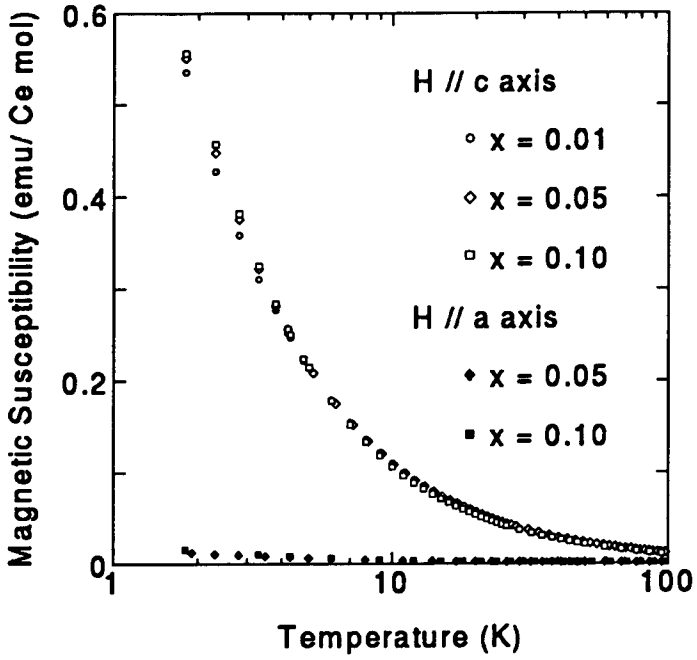

Figure 6.3: *Magnetic susceptibilities of* $(Ce_xLa_{1-x})Ru_2Si_2$ *(*x *= 0.01, 0.05, and 0.10) along the c and a axes in the logarithmic-temperature scale.*

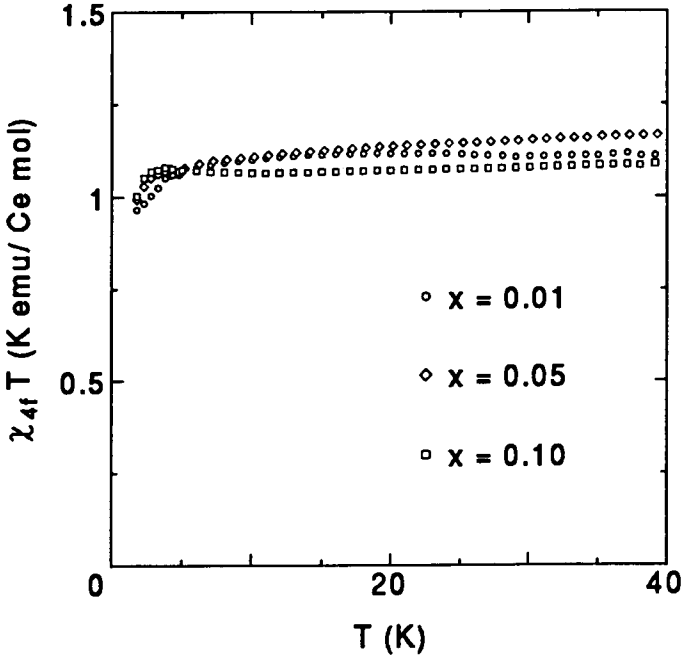

Figure 6.4: $\chi_{4f}T$ *vs* T *plots of the magnetic susceptibilities of* $(Ce_xLa_{1-x})Ru_2Si_2$ *(*x *= 0.01, 0.05, and 0.10) along the c axis.*

6.2.2 Magnetization

Figure 6.5 shows the magnetization curves of the $(Ce_{0.05}La_{0.95})Ru_2Si_2$ and $LaRu_2Si_2$ single crystals along the c and a axes at 4.2 K. The large magnetic anisotropy is observed for $(Ce_{0.05}La_{0.95})Ru_2Si_2$. The data of $(Ce_{0.05}La_{0.95})Ru_2Si_2$ along the c axis shows the tendency to saturation of the magnetization at 7 T. The magnetization of $LaRu_2Si_2$ is negligibly small compared with that of $(Ce_{0.05}La_{0.95})Ru_2Si_2$. The magnetization curves of $(Ce_xLa_{1-x})Ru_2Si_2$ of $x = 0.01$ and 0.05 along the c axis at various temperatures are shown in Fig. 6.6. The contribution of $4f$ electrons is obtained in the same way mentioned above. It seems that the remarkable cerium-concentration dependence is not observed in the magnetization curves. The magnitude of the magnetization along the c axis at 4.2 K at 7 T is about 30 times larger than that along the a axis.

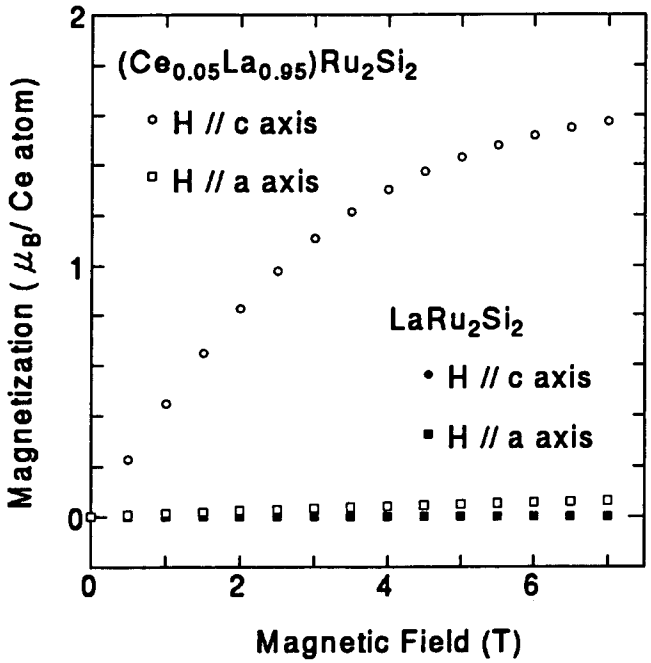

Figure 6.5: *Magnetization curves of $(Ce_{0.05}La_{0.95})Ru_2Si_2$ and $LaRu_2Si_2$ along the c and a axes at 4.2 K.*

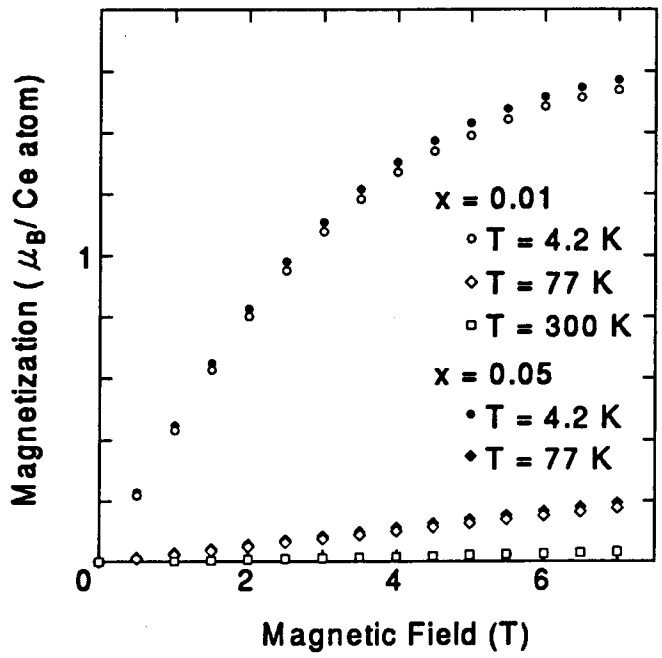

Figure 6.6: *Magnetization curves of* $(Ce_xLa_{1-x})Ru_2Si_2$ *(*x *= 0.01 and 0.05) along the c axis at various temperatures.*

6.2.3 Specific heat

Figure 6.7 shows the specific heats of the $(Ce_xLa_{1-x})Ru_2Si_2$ (x = 0.05 and 0.10) and $LaRu_2Si_2$ polycrystalline samples. The specific heats of $(Ce_xLa_{1-x})Ru_2Si_2$ (x = 0.05 and 0.10) and $LaRu_2Si_2$ in the low-temperature region are shown in Fig. 6.8. No phase transition is observed in each sample down to 3 K. The lattice-specific heat is dominant at high temperatures and each sample shows same temperature dependence. However, the data of $(Ce_xLa_{1-x})Ru_2Si_2$ show a upturn behavior at low temperatures. The C/T vs T^2 plots of the specific heats with each cerium concentration are shown in Fig. 6.9. The C/T of $(Ce_xLa_{1-x})Ru_2Si_2$ start to deviate from that of $LaRu_2Si_2$ with decreasing temperature in the low-temperature region. This behavior is more evident as the cerium concentration increases. Figure 6.10 shows the C_{4f}/T vs T plots of the electronic-specific heats of $(Ce_xLa_{1-x})Ru_2Si_2$ (x = 0.05 and 0.10). The contribution of $4f$ electron is obtained from the total specific heat by subtracting the lattice part using the specific heat of $LaRu_2Si_2$. The data steeply increase as temperature decreases and do not show the tendency to a constant down to 3 K. It seems that the data can not be normalized by the cerium concentration even if we concern the systematic errors explained in subsection 5.2.3. The increasing behavior of the data is shifted toward the lower temperature as the cerium concentration decreases.

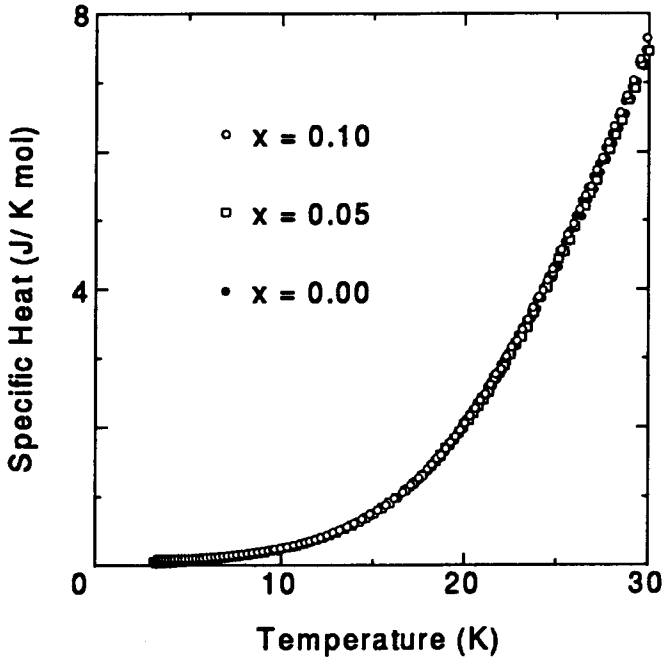

Figure 6.7: *Temperature dependence of the specific heats of* $(Ce_xLa_{1-x})Ru_2Si_2$ *(*x *= 0.05 and 0.10) and* $LaRu_2Si_2$.

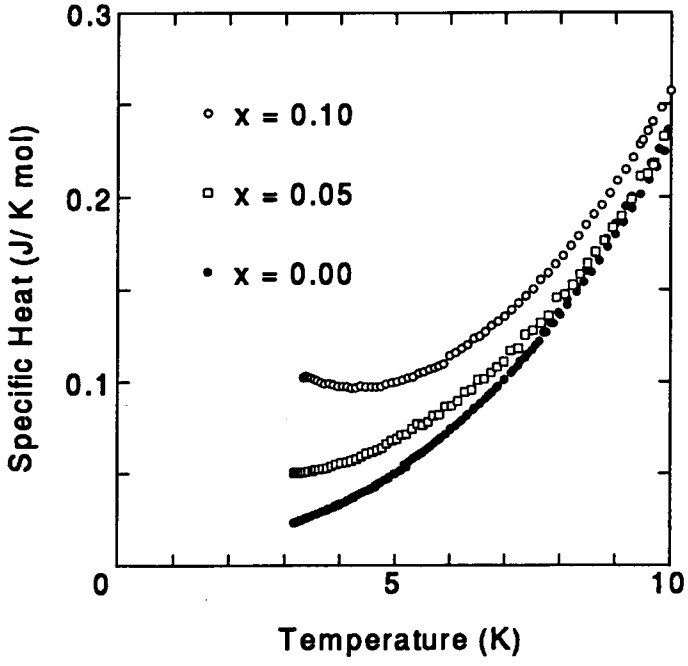

Figure 6.8: *Temperature dependence of the specific heats of* $(Ce_xLa_{1-x})Ru_2Si_2$ *(*x *= 0.05 and 0.10) and* $LaRu_2Si_2$ *in the low-temperature region.*

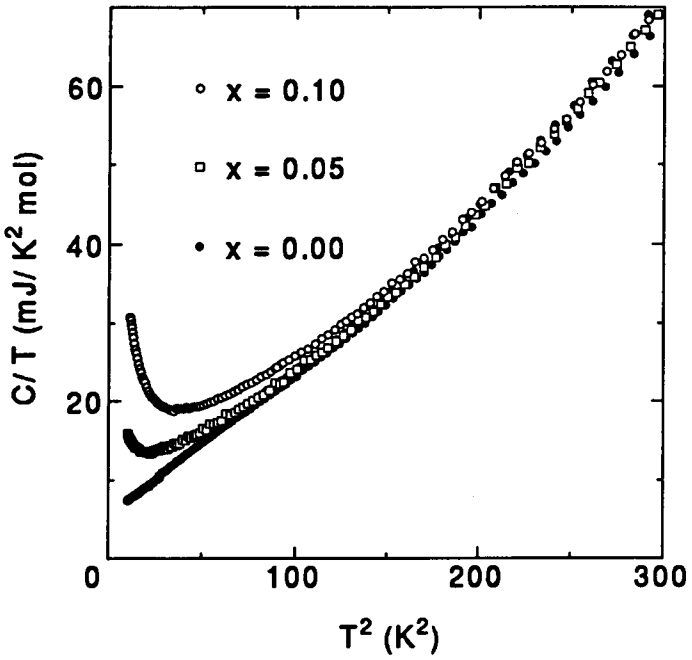

Figure 6.9: *C/T vs T^2 plots of the specific heats of $(Ce_xLa_{1-x})Ru_2Si_2$ (x = 0.05 and 0.10) and $LaRu_2Si_2$.*

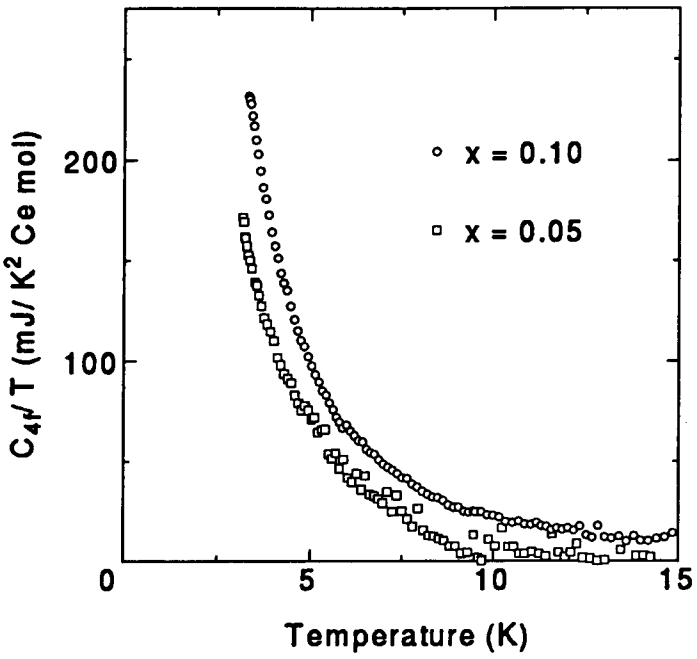

Figure 6.10: *C_{4f}/T vs T plots of the electronic-specific heats of $(Ce_xLa_{1-x})Ru_2Si_2$ (x = 0.05 and 0.10).*

6.3 Analysis and discussion

The crystalline-electric-field (CEF) effect is concerned to explain the large magnetic anisotropy of the experimental results.

The electronic configurations of cerium is the xenon (Xe) shell+$(4f)^2$+$(5d)^0$+$(6s)^2$. According to the earlier studies, it is suggested that cerium in $(Ce_xLa_{1-x})Ru_2Si_2$ is in a tri-valent state with one $4f$ electron [5, 6, 7, 8]. Therefore, the cerium ion is assumed here to be in tri-valent state. For cerium in the tri-valent state with $(4f)^1$, ${}^2F_{\frac{5}{2}}$ is the ground J multiplet with a sixfold degeneracy. The energy splitting of the J multiplet ${}^2F_{\frac{5}{2}}$ is shown in Fig. 6.11. The wave functions of the CEF eigenstate of the J multiplet ${}^2F_{\frac{5}{2}}$ are expressed as follows.

$$\begin{aligned}
\Gamma_7 : \quad |\Gamma_{t7}^{(1)}\rangle &= \beta\left|\pm\frac{5}{2}\right\rangle - \alpha\left|\mp\frac{3}{2}\right\rangle, \\
\Gamma_8 : \quad |\Gamma_{t6}\rangle &= \left|\pm\frac{1}{2}\right\rangle, \\
\Gamma_8 : \quad |\Gamma_{t7}^{(2)}\rangle &= \alpha\left|\pm\frac{5}{2}\right\rangle + \beta\left|\mp\frac{3}{2}\right\rangle. \qquad (6.1)
\end{aligned}$$

The matrix elements are calculated from the eigenstates by using the operator J_z and J_x.

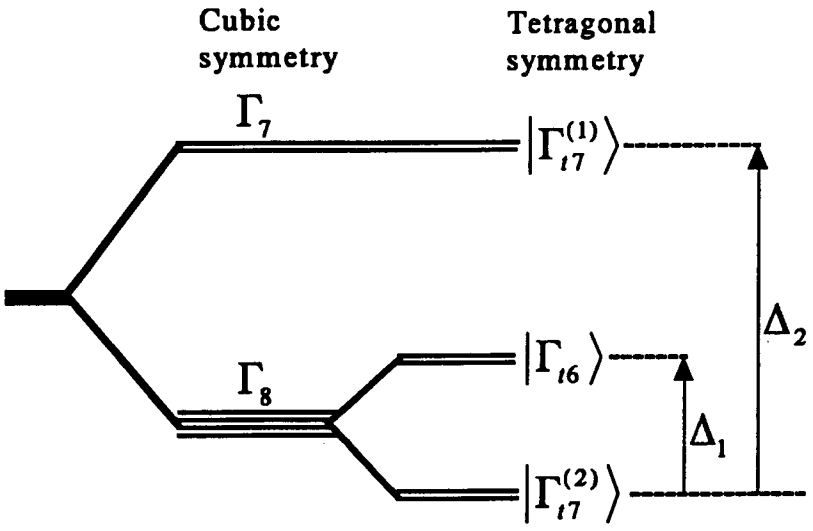

Figure 6.11: *Energy split of the tetragonal CEF for* $J = \frac{5}{2}$.

Among the three doublets in Fig. 6.11, Γ_{t6} gives much worse fitting between the calculated susceptibility and experimental data than others. Therefore, Γ_{t6} is eliminated from the candidate of the ground state. $\Gamma_{t7}^{(1)}$ and $\Gamma_{t7}^{(2)}$ give a good fit to the data. Here after, we discuss the CEF effect with $\Gamma_{t7}^{(1)}$ ground state, because $\Gamma_{t7}^{(1)}$ and $\Gamma_{t7}^{(2)}$ lead to the similar results.

Fig. 6.12 shows the best fitting curves of the magnetic susceptibility to the experimental data. The large uniaxial magnetic anisotropy is explained by the CEF model. The parameters determined here are as follows. The coefficient α of the wave function is estimated to

be 0.9618, which corresponds to that $\beta = \sqrt{1-\alpha^2}$ is 0.2739. The energy splitting Δ_1 and Δ_2 are about 300 $\sim$ 400 K and 10^3 K, respectively. These parameters agree fairly well with those for $CeRu_2Si_2$ [5, 6, 7, 8]. The calculated susceptibilities can explain the experimental data in the temperature region above 50 K. However, the calculated susceptibilities along the both axes deviate from the experimental data in the low temperature region below 20 K as shown in Fig. 6.13.

The magnetization is calculated by using the same fitting parameters. Fig. 6.14 shows the fitting results to the magnetization data of $(Ce_xLa_{1-x})Ru_2Si_2$ ($x = 0.01$ and 0.05) along the c axis at various temperatures. The calculated magnetizations at 77 and 300 K agree fairly well with the experimental data. The calculated magnetization at 4.2 K is a little larger than the value of the experimental data.

The $-Td\chi/dT$ vs T plot of the magnetic susceptibility of $(Ce_{0.05}La_{0.95})Ru_2Si_2$ is shown in Fig. 6.15. The $-Td\chi/dT$ vs $\ln T$ plot is also shown in Fig. 6.16. The dashed lines in Fig. 6.15 and 6.16 show the $-Td\chi/dT$ plot calculated by the CEF model. As explained in subsection 5.3.3, this plot is used to classify the temperature dependence of the susceptibility. No maximum is observed in the $-Td\chi/dT$ plot of the experimental data above 2 K, which is in contrast with the case of the dilute uranium system $(U_xLa_{1-x})Ru_2Si_2$. The susceptibility increases more steeply than the slope of $-\ln T$ above 2 K. There is no complete screening of the localized magnetic moment as that in the dilute uranium system. The data along the both axes above 50 K are fairly well fitted by the fitting curves. However, the data especially along the a axis deviate from the fitting curves in the low-temperature region below 20 K. The low-temperature behavior of the data can not be explained completely by the CEF model.

The CEF model is not valid to explain the experimental results at low temperatures, which is also suggested by the magnetic-specific heat shown in Fig. 6.10 and the $\chi_{4f}T$ vs T plot shown in Fig. 6.4. The increase of the C_{4f}/T at low temperatures may mean that there exist the Kondo screening due to the small T_K or the antiferromagnetic correlation of the phase transition.

The Kondo screening is discussed first for the reason of the increase of the C_{4f}/T. The Kondo screening is expected to be observed in the dilute cerium system $(Ce_xLa_{1-x})Ru_2Si_2$, because $CeRu_2Si_2$ is known as the Kondo lattice system with $T_K = 24.4$ K. The Kondo temperature, however, is considered to be variable when the volume of the compound varies [9]. When the unit-cell volume expands, the Kondo temperature is considered to decrease. The unit-cell volume of $LaRu_2Si_2$ is larger than that of $CeRu_2Si_2$ [10] and then the unit-cell volume of $(Ce_xLa_{1-x})Ru_2Si_2$ is larger than that of $CeRu_2Si_2$. It is possible that the Kondo temperature of $(Ce_xLa_{1-x})Ru_2Si_2$ ($x \leq 0.10$) is much lower than 1 K. Therefore, the increase of the C_{4f}/T may show the beginning of the enhancement of the γ value, because the γ value is in inverse proportion to the Kondo temperature T_K, *i.e.*, $\gamma \propto 1/T_K$. The decrease of the $\chi_{4f}T$ at low temperatures may then show the beginning of the Kondo screening of the localized magnetic moment.

The magnetic-phase transition effect is discussed second for another reason of the increase of the C_{4f}/T. As explained in section 6.1, the lanthanum-doped compound shows the

magnetic order. The dilute cerium compound $(Ce_{0.10}La_{0.90})Ru_2Si_2$ has been reported to exhibit the magnetic order with the Néel temperature $T_N = 0.9$ K without showing the specific-heat data [11]. This temperature is considerably lower than the temperature range performed for the specific-heat measurement. The tail part of the magnetic correlation due to the magnetic order spreads in the wide temperature range above T_N as seen in the specific-heat data of $(Ce_{0.30}La_{0.70})Ru_2Si_2$ [7]. Therefore, the increase of the C_{4f}/T at low temperatures may show the tail part of the magnetic order. The decrease of the $\chi_{4f}T$ at low temperatures may then show the antiferromagnetic correlation between the magnetic moments. In either case, the measurement with the dilution refrigerator in the lower temperature region is necessary to clarify the magnetic property and the ground state of the dilute cerium system.

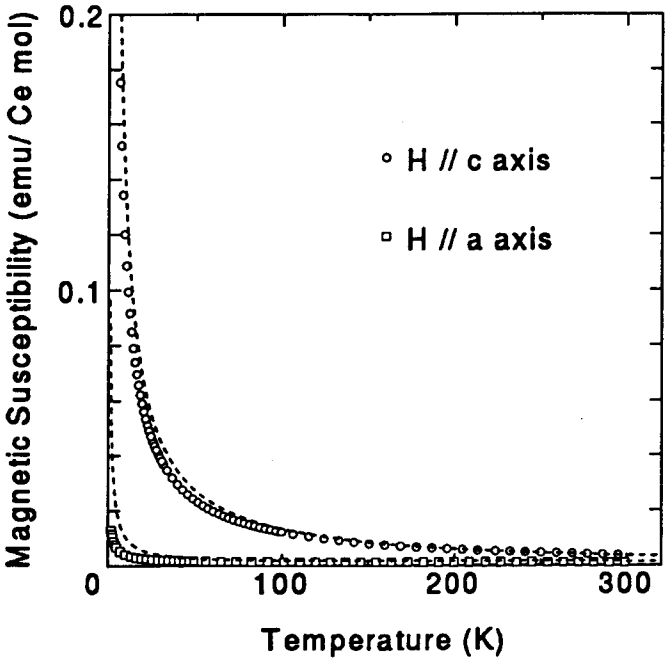

Figure 6.12: *Temperature dependence of the magnetic susceptibility of* $(Ce_{0.05}La_{0.95})Ru_2Si_2$ *along the c and a axes. The dashed lines show the temperature dependence of the calculated magnetic susceptibility along the c and a axes.*

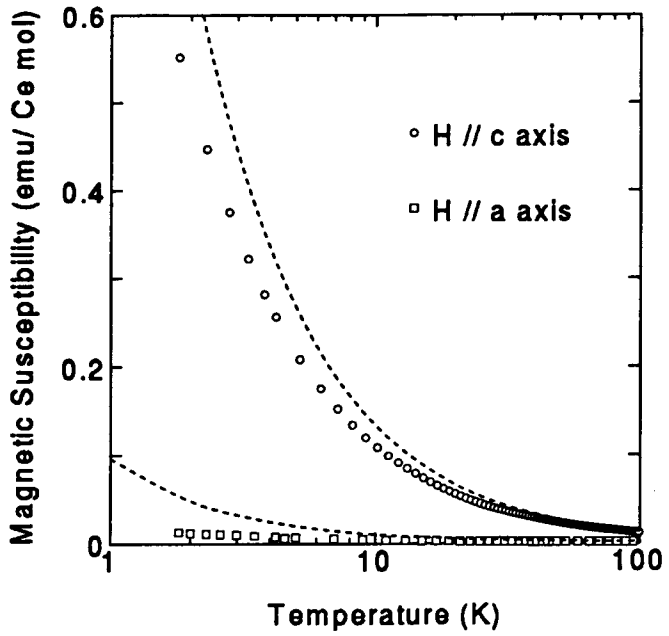

Figure 6.13: *Magnetic susceptibility of* $(Ce_{0.05}La_{0.95})Ru_2Si_2$ *along the c and a axes in the logarithmic-temperature scale. The dashed lines show the temperature dependence of the calculated magnetic susceptibility along the c and a axes.*

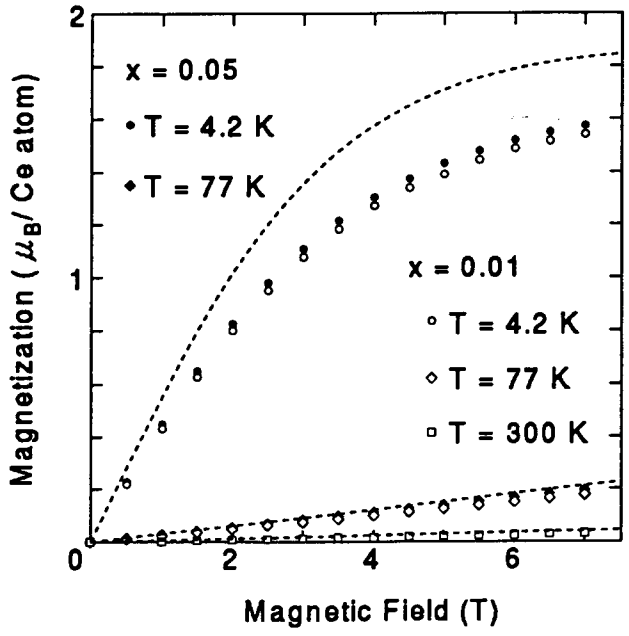

Figure 6.14: *Magnetization curves of* $(Ce_xLa_{1-x})Ru_2Si_2$ *(*$x = 0.01$ *and 0.05) along the c axis at various temperatures. The dashed lines show the calculated magnetization curves along the c axis at various temperatures.*

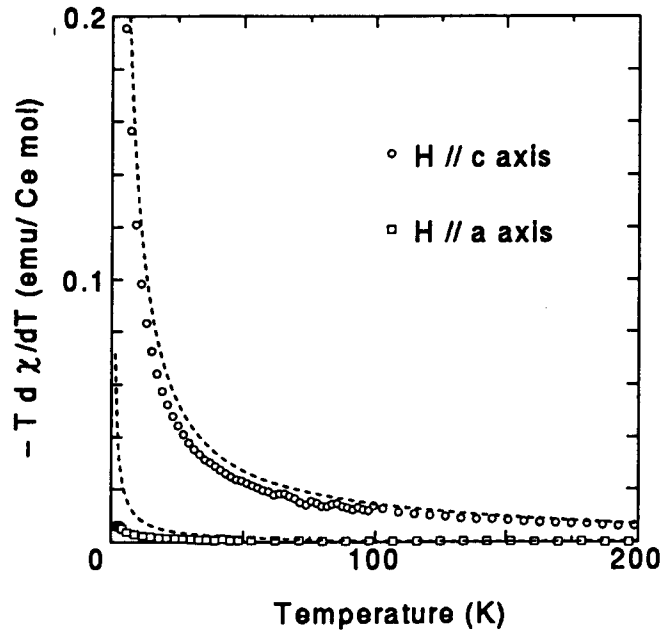

Figure 6.15: *Temperature dependence of the $-Td\chi/dT$ plot of $(Ce_{0.05}La_{0.95})Ru_2Si_2$ along the c and a axes. The dashed lines show the temperature dependence of the $-Td\chi/dT$ plot using the calculated magnetic susceptibility along the c and a axes.*

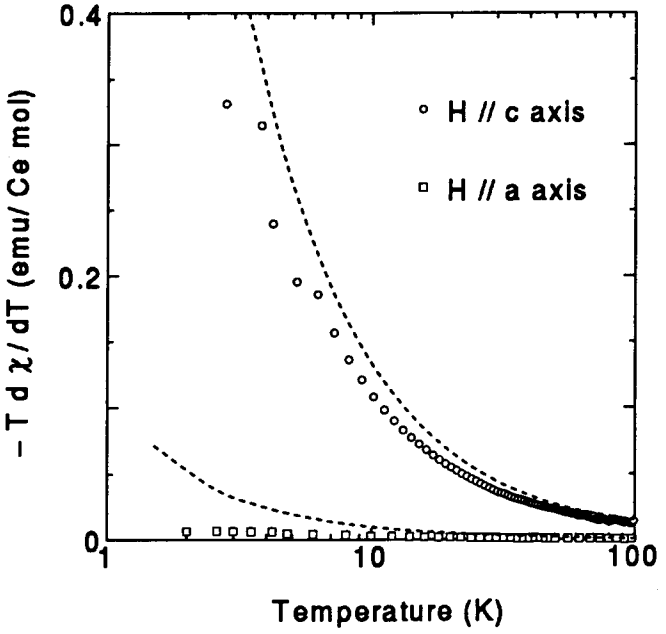

Figure 6.16: *$-Td\chi/dT$ plot of $(Ce_{0.05}La_{0.95})Ru_2Si_2$ along the c and a axes in the logarithmic-temperature scale. The dashed lines show the temperature dependence of the $-Td\chi/dT$ plot using the calculated magnetic susceptibility along the c and a axes.*

6.4 Conclusion

We have analyzed the magnetic and thermodynamical properties of the dilute cerium compound system $(Ce_xLa_{1-x})Ru_2Si_2$ ($x \leq 0.10$) by the crystalline-electric-field (CEF) model. In the high-temperature region above 50 K, the CEF model shows a good agreement with the experimental data. The obtained CEF parameters agree fairly well with those for $CeRu_2Si_2$.

The low-temperature behavior below about 20 K, however, can not be explained by the CEF model. The experimental results of the magnetic susceptibility and magnetization indicate an antiferromagnetic screening or correlation of the magnetic moment at low temperatures. The experimental result of the specific heat indicates the anomaly of the enhancement of the specific heat at low temperatures. These experimental results is considered to show the beginning of the Kondo screening or the influence of the antiferromagnetic phase transition. In either case, the measurement in the still lower-temperature region is necessary to clarify the magnetic property and the ground state of the dilute cerium system.

The Kondo temperature of the dilute cerium system is considered to be lower than 1 K as suggested from this study. The change of the Kondo temperature from 24.4 K of $CeRu_2Si_2$ to lower than 1 K is mainly attributed to the volume change. From the comparison between the dilute uranium system $(U_xLa_{1-x})Ru_2Si_2$ and the dilute cerium system, it is suggested that the the Kondo temperature of the dilute uranium system, which CEF scheme is the non-Kramers doublet ground state and the singlet first-excited state, is less influenced by the volume change than that of the dilute cerium system which CEF scheme is the Kramers doublet ground state.

Bibliography

[1] S. Quezel, P. Burlet, J.L. Jacoud, L.P. Regnault, J. Rossat-Mignod, C. Vettier, P. Lejay, and J. Flouquet, J. Magn. Magn. Mater. **76-77**, 403 (1988).

[2] Y. Yamamoto, K. Marumoto, Y. Miyako, K. Nishiyama, and K. Nagamine, Hyperfine Interactions **20**, (1996).

[3] J.-M. Mignot, J.-L. Jacoud, L.-P. Regnault, J. Rossat-Mignod, P. Haen, P. Lejay, Ph. Boutrouille, B. Hennion, and D. Petitgrand, Physica B **163**, 611 (1990).

[4] M.J. Besnus, P. Lehmann, and A. Meyer, J. Magn. Magn. Mater. **63-64**, 323 (1987).

[5] L.C. Gupta, D.E. MacLaughlin, C. Tien, C. Godart, M.A. Edwards, and R.D. Parks, Phys. Rev. B **28**, 3673 (1983).

[6] P. Haen, J. Flouquet, F. Lapierre, P. Lejay, and G. Remenyi, J. Low. Temp. Phys. **67**, 391 (1987).

[7] M.J. Besnus, J.P. Kappler, P. Lehmann, and A. Meyer, Solid State Commun. **55.** 779 (1985).

[8] R. Djerbi, P. Haen, F. Lapierre, P. Lehmann, and J.P. Kappler, J. Magn. Magn. Matter. **76-77**, 260 (1988).

[9] T. Sakakibara, H. Amitsuka, D. Sugimoto, H. Mitamura, and K. Matsuhira, Physica B **186-188**, 317 (1993).

[10] K. Hiebl, C. Horvath, P. Rogl, and M.J. Sienko, J. Magn. Magn. Mater. **37**, 287 (1983).

[11] P. Lehmann, M.J. Besnus, J.P. Kappler, and A. Meyer, *Theoretical and Experimental Aspects of Valence Fluctuations and Heavy Fermions*, edited by L.C. Gupta and S.K. Malik (Plenum, N. Y., 1987) p. 425.

Chapter 7

Comparative study with the dilute praseodymium compound system $(Pr_xLa_{1-x})Ru_2Si_2$

7.1 Introduction

The magnetic measurements on the dilute praseodymium compound system $(Pr_xLa_{1-x})Ru_2Si_2$ ($x \leq 0.10$) have been performed to compare the single-site properties with those of the dilute uranium compound system $(U_xLa_{1-x})Ru_2Si_2$ ($x \leq 0.15$). The ground J multiplets of the dilute uranium and praseodymium ions are considered to be the same and the comparison between the dilute praseodymium and uranium systems is expected to show the difference of the nature between the $4f$ and $5f$ electrons. Furthermore, it is also expected to obtain the more information about the ground state of the dilute uranium system $(U_xLa_{1-x})Ru_2Si_2$ which shows the Kondo screening of uranium at low temperatures [1, 2].

The praseodymium and cerium ions are considered to have two $4f$ electrons and one $4f$ electron, respectively. However, the compound $PrRu_2Si_2$ is a ferromagnet with a Curie temperature of 17.8 K [3] in contrast with the paramagnetic heavy-fermion compound $CeRu_2Si_2$. There is the difference of the $4f$ electron number in the dilute praseodymium and cerium systems and the study for the influence of the f electron number will be useful to consider the formation of the heavy-fermion state.

7.2 Experimental results

7.2.1 Magnetic susceptibility

The magnetic susceptibilities of $(Pr_{0.02}La_{0.98})Ru_2Si_2$ and $LaRu_2Si_2$ single crystals along the c and a axes are shown in Fig. 7.1. It is noted that a large uniaxial magnetic anisotropy is observed for $(Pr_{0.02}La_{0.98})Ru_2Si_2$ as in $PrRu_2Si_2$ and in the dilute uranium system

$(U_xLa_{1-x})Ru_2Si_2$. The susceptibility of $(Pr_{0.02}La_{0.98})Ru_2Si_2$ along the c axis shows the Curie-Weiss behavior at high temperatures, while the susceptibility along the a axis is small and almost constant down to the lowest temperatures measured. The susceptibility of $LaRu_2Si_2$ is small and shows almost no temperature dependence. It shows a small constant negative and positive value in the field applied along the c and a axes, respectively, except for a small increase in the low-temperature region.

Figure 7.2 shows the magnetic susceptibilities of $(Pr_xLa_{1-x})Ru_2Si_2$ (x = 0.02, 0.05, and 0.10) along the c and a axes. The contribution of $4f$ electrons is obtained by subtracting the susceptibility of $LaRu_2Si_2$. These data are almost similar to each other, except for a small difference of the absolute value of the susceptibility at low temperatures.

7.2.2 Magnetization

Figure 7.3 shows the magnetization curves of $(Pr_{0.02}La_{0.98})Ru_2Si_2$ and $LaRu_2Si_2$ single crystals along the c and a axes at 4.2 K. The large magnetic anisotropy is observed for $(Pr_{0.02}La_{0.98})Ru_2Si_2$. The data of $(Pr_{0.02}La_{0.98})Ru_2Si_2$ along the c axis shows the tendency to saturation of the magnetization at 7 T, while the magnetization along the a axis is small and almost linear. The magnetization of $LaRu_2Si_2$ is negligibly small compared with that of $(Pr_{0.02}La_{0.98})Ru_2Si_2$. The magnetization curves of $(Pr_xLa_{1-x})Ru_2Si_2$ (x = 0.02, 0.05, and 0.10) along the c axis at various temperatures are shown in Fig. 7.4. The contribution of $4f$ electrons is obtained in the same way mentioned above. The data at 77 K and 300 K are almost linear up to 7 T in contrast with the data at 4.2 K. The absolute value of the magnetization per praseodymium atom has an error which is mainly caused by an inaccuracy of about 10 % coming from the nominal praseodymium concentration. Except for this error, the qualitative behavior of these data is understood that they show the single-site properties of the praseodymium ion.

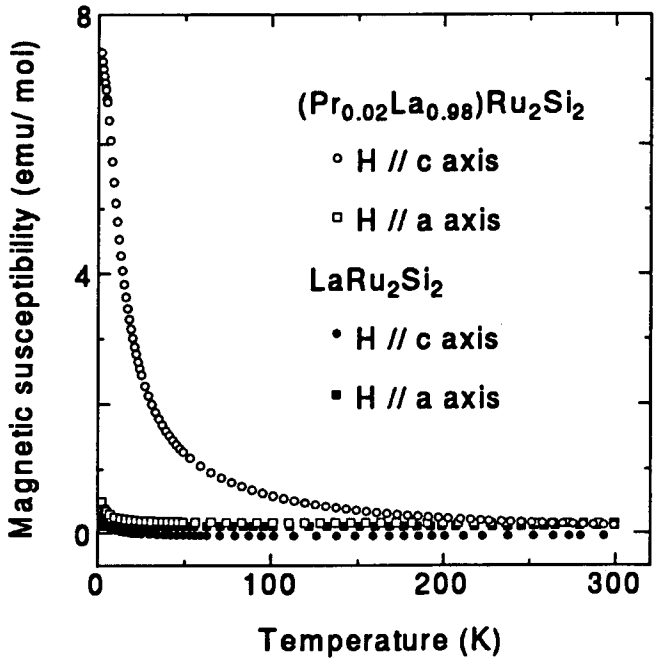

Figure 7.1: *Temperature dependence of the magnetic susceptibilities of* $(Pr_{0.02}La_{0.98})Ru_2Si_2$ *and* $LaRu_2Si_2$ *along the c and a axes.*

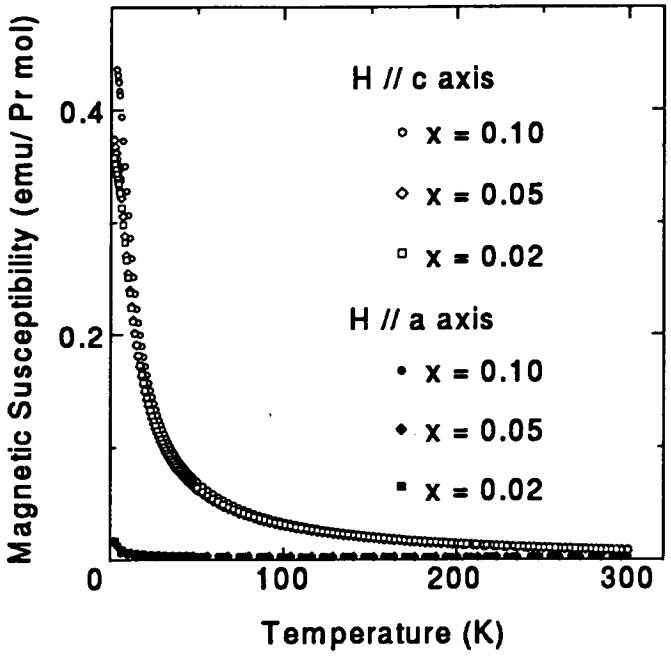

Figure 7.2: *Temperature dependence of the magnetic susceptibilities of* $(Pr_xLa_{1-x})Ru_2Si_2$ *(*$x = 0.02$*, 0.05, and 0.10) along the c and a axes.*

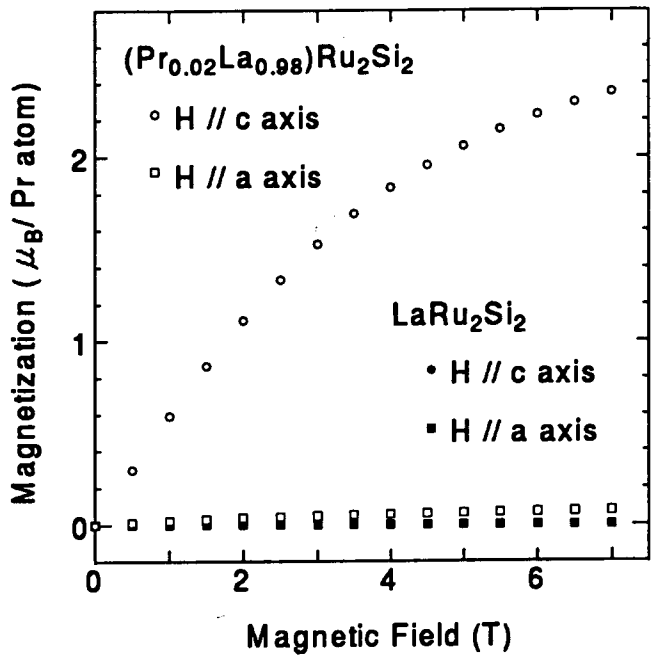

Figure 7.3: *Magnetization curves of $(Pr_{0.02}La_{0.98})Ru_2Si_2$ and $LaRu_2Si_2$ along the c and a axes at 4.2 K.*

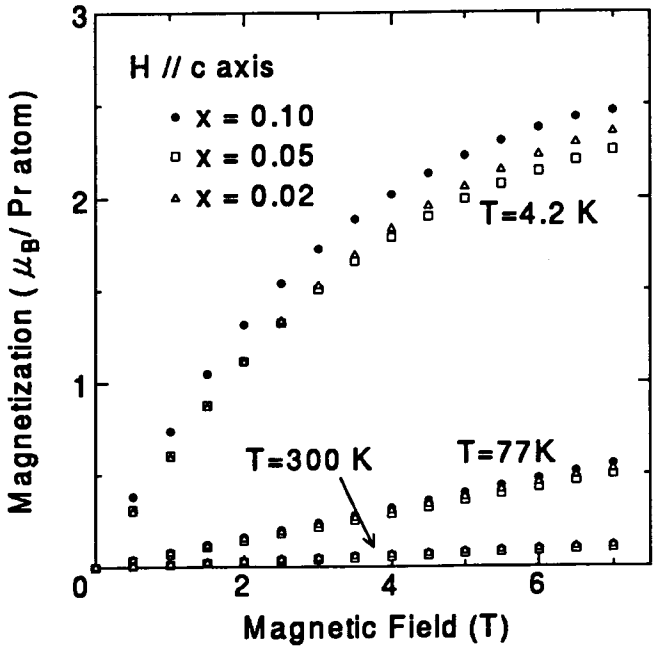

Figure 7.4: *Magnetization curves of $(Pr_xLa_{1-x})Ru_2Si_2$ (x = 0.02, 0.05, and 0.10) along the c axis at various temperatures.*

7.2.3 Specific heat

Figure 7.5 shows the specific heats of the $(Pr_xLa_{1-x})Ru_2Si_2$ (x = 0.02, 0.05, and 0.10) and $LaRu_2Si_2$ polycrystalline samples. No phase transition is observed in each sample down to 3 K. The lattice-specific heat is dominant at high temperatures and each sample shows same temperature dependence. The specific heat at low temperatures, however, shows the concentration dependence. The C/T vs T^2 plots of the specific heats for each praseodymium concentration are shown in Fig. 7.6. The broad peak is observed at around 7 K and its peak becomes remarkable as the praseodymium concentration increases.

Figure 7.7 shows the C_{4f}/T vs T plots of the electronic-specific heats of $(Pr_xLa_{1-x})Ru_2Si_2$ (x = 0.02, 0.05, and 0.10). The contribution of $4f$ electron is obtained from the total specific heat by subtracting the lattice part using the specific heat of $LaRu_2Si_2$. Although the absolute value of the data has the systematic error explained in subsection 5.2.3, the data are qualitatively in agreement with each other. The electronic-specific heat shows a broad peak of the Schottky anomaly at about 7 K. The C_{4f}/T value decreases steeply as temperature decreases and the enhancement for the γ value due to the f electrons is not observed.

The magnetic entropy is obtained by integrating the C_{4f}/T vs T plot. As shown in Fig. 7.8, its entropy is approaching to the value of $R\ln 2$ as temperature increases, which indicates that this dilute system has the twofold degeneracy of the CEF level at low temperatures.

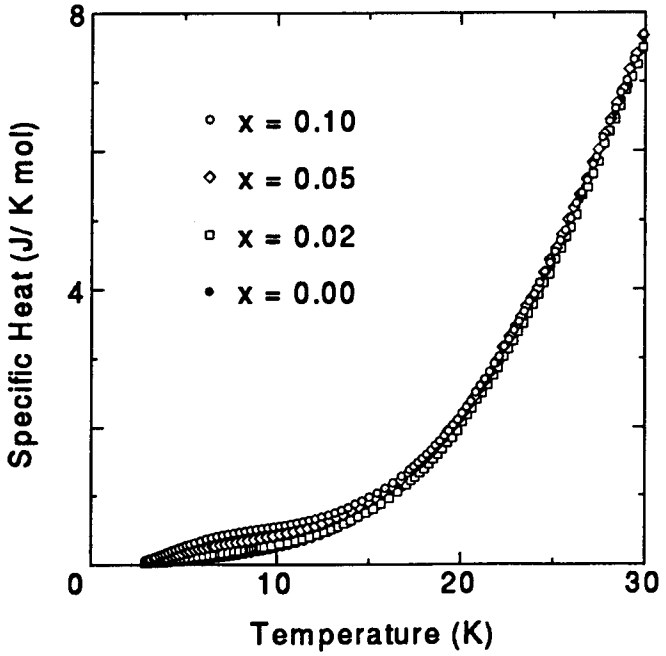

Figure 7.5: *Temperature dependence of the specific heats of $(Pr_xLa_{1-x})Ru_2Si_2$ (x = 0.02, 0.05, and 0.10) and $LaRu_2Si_2$.*

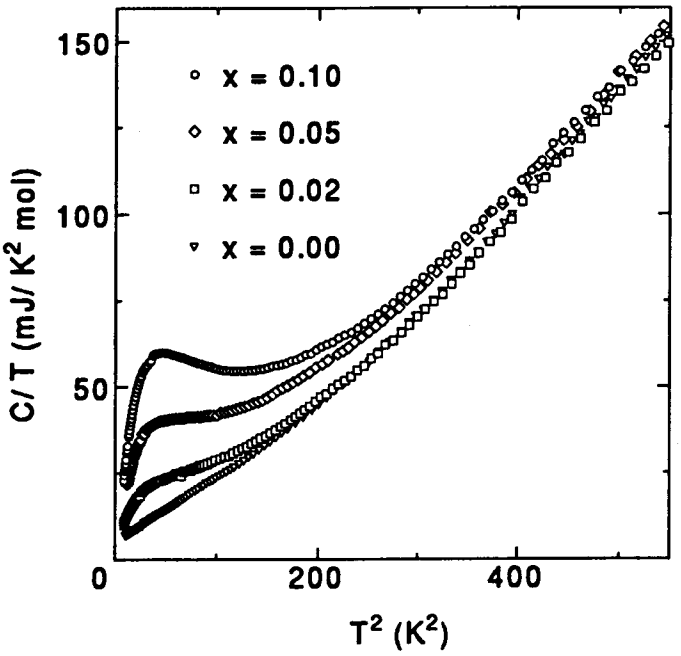

Figure 7.6: *C/T vs T^2 plots of the specific heats of $(Pr_xLa_{1-x})Ru_2Si_2$ (x = 0.02, 0.05, and 0.10) and $LaRu_2Si_2$.*

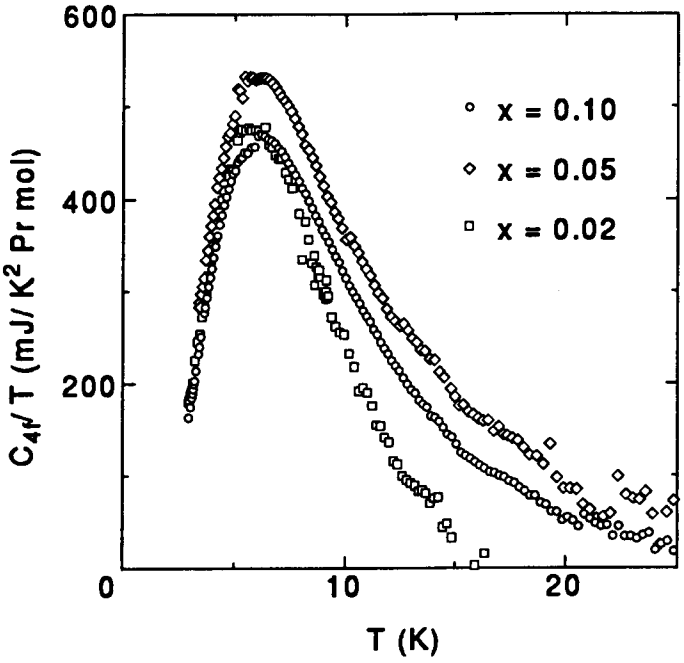

Figure 7.7: *C_{4f}/T vs T plots of the electronic-specific heats of $(Pr_xLa_{1-x})Ru_2Si_2$ (x = 0.02, 0.05, and 0.10).*

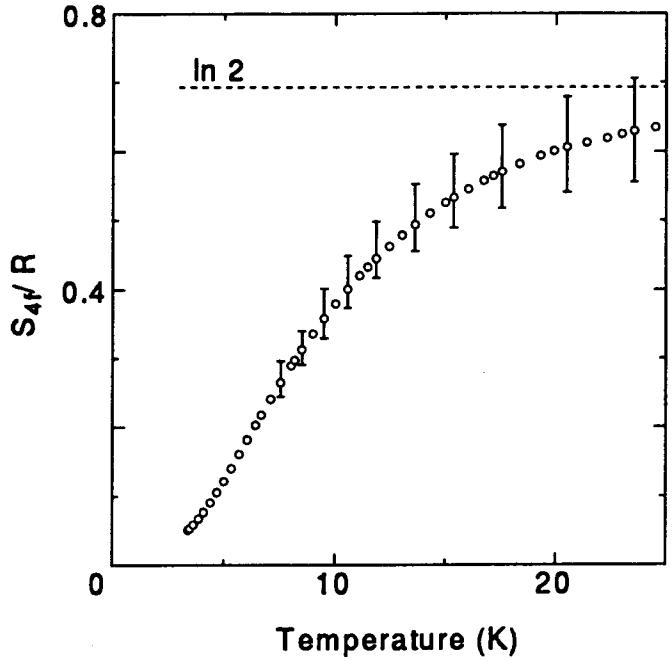

Figure 7.8: *Temperature dependence of the magnetic entropy of* $(Pr_{0.05}La_{0.95})Ru_2Si_2$.

7.3 Analysis and discussion

The analysis of the crystalline-electric-field (CEF) model is performed to explain the behaviors of the magnetic susceptibility, magnetization, and specific heat of the dilute praseodymium system.

The electronic configurations of praseodymium is the xenon (Xe) shell+$(4f)^3$+$(5d)^0$+$(6s)^2$. According to the earlier studies, it is suggested that praseodymium in $(Pr_xLa_{1-x})Ru_2Si_2$ is in a tri-valent state with two $4f$ electrons [4]. For praseodymium in the tri-valent state with $(4f)^2$, $^3H_4$ is the ground J multiplet with a ninefold degeneracy. The energy splitting of the J multiplet $^3H_4$ is shown in Fig. 5.15. The wave functions of the CEF eigenstate of the J multiplet $^3H_4$ are expressed in Eq. 5.4. The matrix elements are calculated from the eigenstates by using the operator J_z and J_x.

From the specific-heat data, it is suggested that the CEF ground and first-excited states are the singlets with the CEF splitting of 20 ± 1 K. As shown by the dashed line in Fig. 7.9, the singlet-singlet CEF model yields the good fitting in the whole range of the specific-heat measurement. The data are well fitted by this model especially in the low-temperature region. The γ value is estimated to be 7 ± 1 mJ/K^2 mol from the C/T vs T^2 plot shown in Fig. 7.6. This γ value is very small in contrast with that of the dilute uranium system. Therefore, $(Pr_xLa_{1-x})Ru_2Si_2$ does not show the Kondo screening as observed in the dilute uranium system at low temperatures.

The magnetic susceptibilities of $(Pr_xLa_{1-x})Ru_2Si_2$ (x = 0.02, 0.05, and 0.10) are well fitted by the CEF model. The dashed lines in Fig. 7.10 show the best fitting results to the

experimental data. The CEF splitting determined here is as follows. The ground and first excited states are the singlets. The CEF splitting is determined to be 20 ± 1 K from the specific-heat fitting. The wave functions of the ground and first-excited state are $\Gamma_{t1}^{(2)}$ and Γ_{t2} (or Γ_{t2} and $\Gamma_{t1}^{(1)}$), respectively. If the wave functions of the ground and first-excited state are replaced each other, the same fitting result is obtained by using the replaced wave functions. The definition of the wave functions is expressed in the paper of Nieuwenhuys [5]. This CEF analysis indicates that the doublet excited state must be located at more than 300 K above the singlet CEF ground state in order to make the susceptibility along the *a* axis small and independent of the temperature. The fitting calculation agrees quantitatively well with the data along the both axes in the whole-temperature range. The large magnetic anisotropy of the susceptibility and its temperature dependence in the whole-temperature range are well fitted by the CEF calculation.

The magnetization is calculated by using this singlet-singlet CEF model. As explained in subsection 5.3.1, the matrix element of the total Hamiltonian is diagonalized with the same parameters for the susceptibility fitting. The dashed lines in Fig. 7.11 show the calculated magnetization along the *c* axis at various temperatures. The CEF calculation result agree quantitatively well with the experimental data, except for a small difference of the absolute value of the magnetization at 4.2 K at around 7 T.

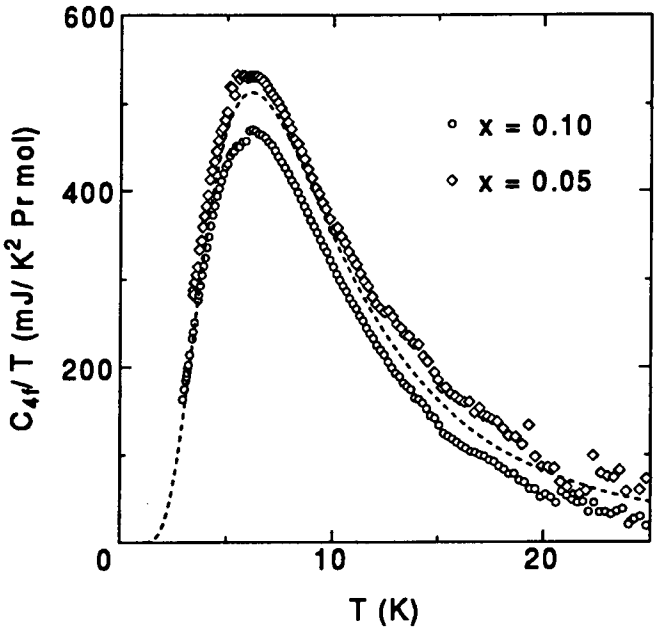

Figure 7.9: *C_{4f}/T vs T plots of the electronic-specific heats of $(Pr_xLa_{1-x})Ru_2Si_2$ ($x = 0.05$ and 0.10). The dashed line shows a theoretical curve of the temperature dependence of C_{4f}/T by using the CEF model.*

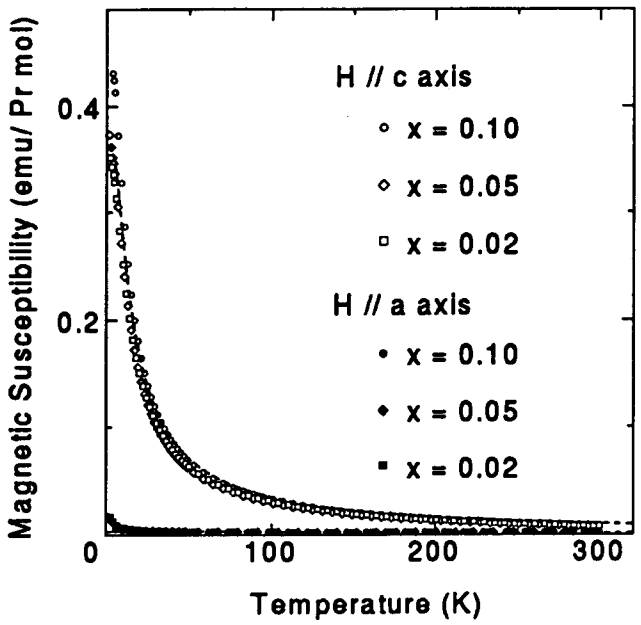

Figure 7.10: *Temperature dependence of the magnetic susceptibilities of* $(Pr_xLa_{1-x})Ru_2Si_2$ *(*x *= 0.02, 0.05, and 0.10) along the c and a axes. The dashed lines show the temperature dependence of the magnetic susceptibility calculated by the CEF model.*

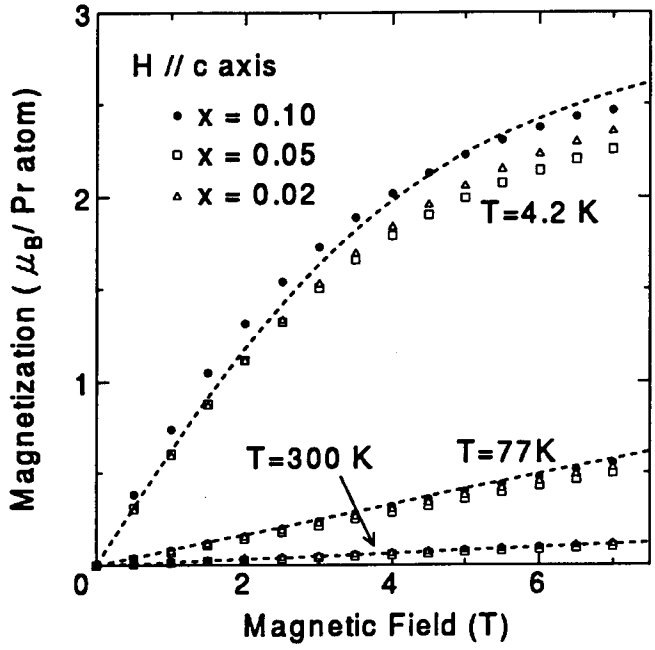

Figure 7.11: *Magnetization curves of* $(Pr_xLa_{1-x})Ru_2Si_2$ *(*x *= 0.02, 0.05, and 0.10) along the c axis at various temperatures. The dashed lines show the magnetization curves along the c axis at various temperatures calculated by the CEF model.*

7.4 Conclusion

We have analyzed the magnetic and thermodynamical properties of the dilute praseodymium compound system $(Pr_xLa_{1-x})Ru_2Si_2$ ($x \leq 0.10$) by the crystalline-electric-field (CEF) model. The large uniaxial anisotropy of the magnetic susceptibility and magnetization, the temperature dependence of the susceptibility, and the Schottky anomaly of the specific heat are well explained by the singlet-singlet CEF model with the CEF splitting of 20 ± 1 K. This means that the dilute praseodymium system is explained as the well localized f electron system.

The low-temperature behavior of the dilute praseodymium system is well explained by the CEF model. This good agreement is in contrast with the case of the dilute uranium compound system $(U_xLa_{1-x})Ru_2Si_2$ ($x \leq 0.15$) which shows the Kondo screening of uranium at low temperatures. The comparison between the dilute uranium and praseodymium systems suggests that the non-Kramers doublet-singlet crystal field splitting, not the singlet-singlet one, is necessary for the Kondo screening as observed in the dilute uranium system [6].

Bibliography

[1] K. Marumoto, T. Takeuchi, T. Taniguchi and Y. Miyako, Physica B **206-207**, 519 (1995).

[2] K. Marumoto, T. Takeuchi, and Y. Miyako, Phys. Rev. B **54**, 12 194 (1996).

[3] K. Hiebl, C. Horvath, P. Rogl, and M.J. Sienko, J. Magn. Magn. Mater. **37**, 287 (1983).

[4] T. Shigeoka, N. Iwata, and H. Fujii, J. Magn. Magn. Mater. **104-107**, 1229 (1992).

[5] G.J. Nieuwenhuys, Phys. Rev. B **35**, 5260 (1987).

[6] K. Marumoto, F. Takayama, and Y. Miyako, submitted to J. Magn. Magn. Mater.

Chapter 8

Transport properties of the lattice uranium compound system $U(Ru_{1-x}Rh_x)_2Si_2$

8.1 Introduction

As introduced in the previous sections, URu_2Si_2 and Rh-doped compound system $U(Ru_{1-x}Rh_x)_2Si_2$ have been studied extensively by the magnetic-susceptibility, magnetization, specific-heat, and neutron-scattering measurements [1, 2, 3, 4, 5, 6, 7]. The electrical resistivity of URu_2Si_2 shows the Cr-like anomaly at T_N. Its temperature dependence below T_N is fitted by using the formula appropriate for an energy-gap antiferromagnet with an additional T^2 term [8, 9, 10]. The Hall coefficient of URu_2Si_2 shows a relative broad maximum at around 50 K and a large jump at T_N. The large jump of the Hall coefficient is considered to be caused by the reconstruction of the Fermi surface due to a SDW phase transition [9, 11, 12]. However, the transport property of $U(Ru_{1-x}Rh_x)_2Si_2$ has not yet been studied sufficiently. In order to study this system from the viewpoint of the transport phenomenon, the electrical-resistivity and Hall-effect measurements have been performed on the $U(Ru_{1-x}Rh_x)_2Si_2$ ($x \leq 0.03$) single crystals. The study of the Rh-doping effect to the transport property of the $U(Ru_{1-x}Rh_x)_2Si_2$ system is expected to give more information about the phase transition.

8.2 Experimental results

8.2.1 Electrical resistivity

Figure 8.1 show the temperature dependence of the electrical resistivity of $U(Ru_{1-x}Rh_x)_2Si_2$ ($x = 0.02$ and 0.03) with the current parallel to the a and c axes. An large anisotropy is observed as in URu_2Si_2. The temperature coefficient $d\rho/dT$ is negative in the a axis down to about 70 K, while the resistivity parallel to the c axis show an almost flat

behavior down to about 70 K. Below about 50 K the resistivity decreases rapidly. These overall behavior are similar to those of URu_2Si_2 [8]. The room-temperature resistivities parallel to the a and c axes at 295 K and the maximum resistivities parallel to the a axis at around 70 K for the samples with $x = 0.02$ and 0.03 are listed in Table 8.1 together with those of URu_2Si_2 [8]. The room-temperature resistivities and the maximum resistivities at around 70 K tend to increase slightly as the Rh concentration increases.

	$x = 0.00$	$x = 0.02$	$x = 0.03$
$\rho_{I\parallel a}$ (R.T.) ($\mu\Omega$ cm)	330	361	398
$\rho_{I\parallel c}$ (R.T.) ($\mu\Omega$ cm)	170	178	196
$\rho_{I\parallel a}(T_{max})$ ($\mu\Omega$ cm)	406	451	501

Table 8.1: *Upper rows : Room-temperature (295 K) resistivities of* $U(Ru_{1-x}Rh_x)_2Si_2$ *(*x *= 0.00, 0.02, and 0.03) parallel to the a and c axes. Lower row : Maximum resistivities of* $U(Ru_{1-x}Rh_x)_2Si_2$ *(*x *= 0.00, 0.02, and 0.03) parallel to the a axis.*

The resistivities in the lower-temperature region are shown in Fig. 8.2. As seen in Fig. 8.2, the resistivity of $x = 0.02$ shows the anomaly related to the phase transition at 13 K. This result is consistent with that of the specific-heat measurement [6]. The data of $x = 0.03$ shows a slight winding anomaly at around 9 K. The phase-transition temperature is discussed in subsection 8.3.1. The magnitude of the anomaly is estimated by using the formula of $\Delta\rho = \rho_{max} - \rho_{min}$. The obtained values are listed in Table 8.2 together with those of URu_2Si_2. The value of $x = 0.02$ parallel to the c axis is much larger than that parallel to the a axis. As the Rh concentration increases, $\Delta\rho$ parallel to the a axis decrease drastically than that parallel to the c axis.

	$x = 0.00$ (a)	$x = 0.00$ (b)	$x = 0.02$
$\Delta\rho_{I\parallel a}$ ($\mu\Omega$ cm)	11.5	9.3	0.55
$\Delta\rho_{I\parallel c}$ ($\mu\Omega$ cm)	21.1	16.2	6.9

Table 8.2: *Magnitude of the anomalies of* $U(Ru_{1-x}Rh_x)_2Si_2$ *(*x *= 0.00 and 0.02) defined as* $\Delta\rho = \rho_{max} - \rho_{min}$. *The data (a) and (b) of* URu_2Si_2 *are taken from the Ref. [8] and [10], respectively.*

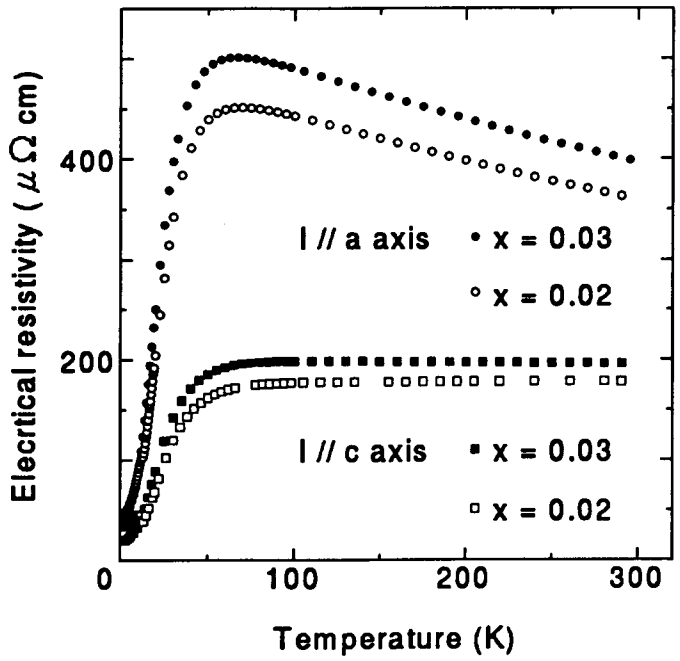

Figure 8.1: *Temperature dependence of the electrical resistivities of* $U(Ru_{1-x}Rh_x)_2Si_2$ *(*x *= 0.02 and 0.03) with the current parallel to the a and c axes.*

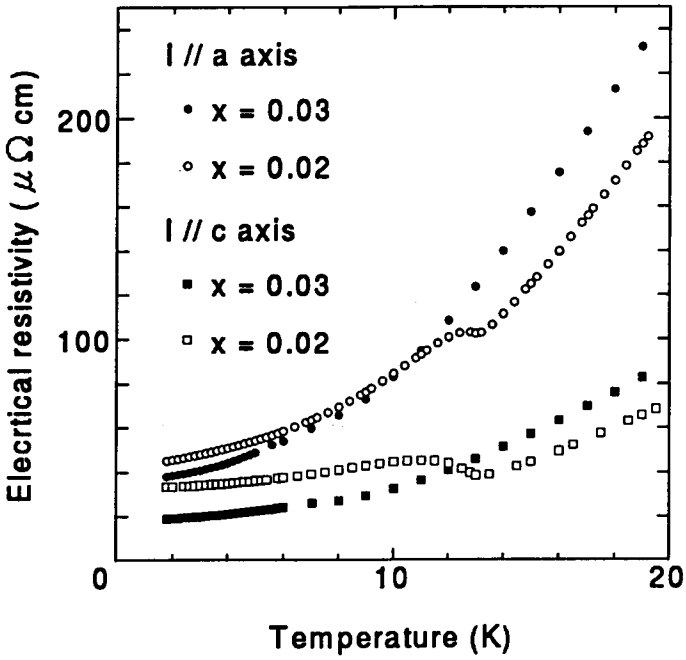

Figure 8.2: *Temperature dependence of the electrical resistivities of* $U(Ru_{1-x}Rh_x)_2Si_2$ *(*x *= 0.02 and 0.03) with the current parallel to the a and c axes in the low-temperature region.*

8.2.2 Hall effect

Figure 8.3 shows the Hall coefficient of $U(Ru_{1-x}Rh_x)_2Si_2$ (x = 0.00 and 0.02) single crystals with the magnetic field parallel to the c axis and the current parallel to the a axis. The sign of the Hall coefficient is positive as observed in all other heavy-fermion metals. As shown in Fig. 8.3, the Hall coefficients of x = 0.00 and 0.02 have a relative maximum at around 50 and 45 K, respectively. The maximum value of x = 0.02 is slightly larger than that of URu_2Si_2. The data in the low-temperature region are shown in Fig. 8.4. The phase-transition temperature T_N is determined as that where a sharp-bending point of the data appears. The values of T_N are obtained to be 17.3 and 13.0 K for the samples with x = 0.00 and 0.02, respectively. These values are consistent with those obtained from the specific-heat measurement [6]. At T_N, the Hall coefficient jumps sharply and then decreases slowly down to the lowest temperature measured. The data of URu_2Si_2 agree quantitatively well with that of the early studies [9, 11, 12].

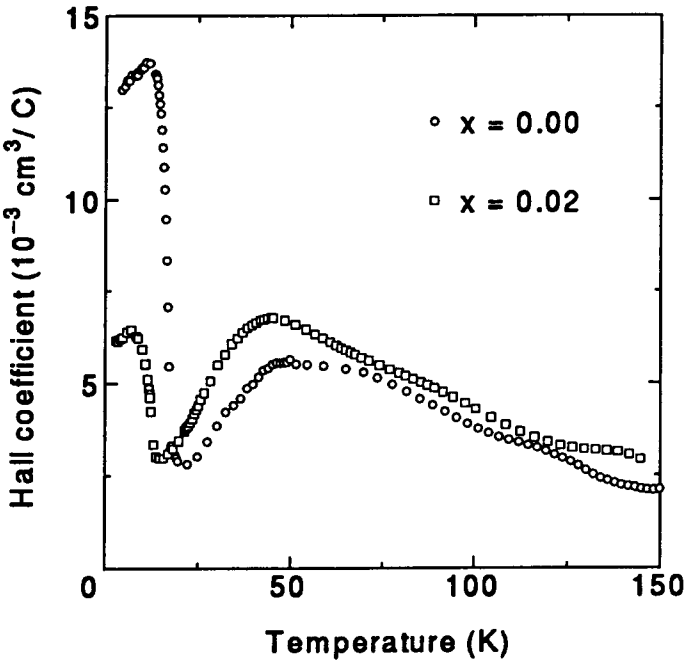

Figure 8.3: *Temperature dependence of the Hall coefficients of $U(Ru_{1-x}Rh_x)_2Si_2$ (x = 0.00 and 0.02) with the magnetic field parallel to the c axis and the current parallel to the a axis.*

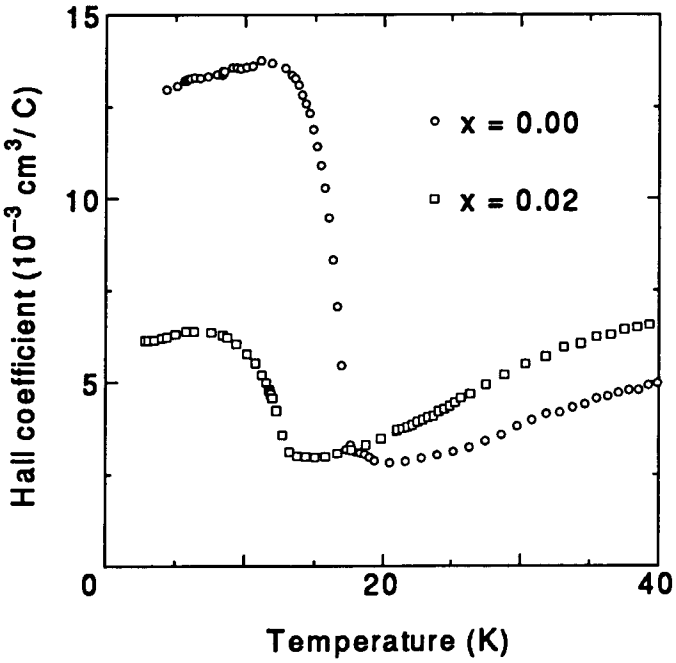

Figure 8.4: *Temperature dependence of the Hall coefficients of $U(Ru_{1-x}Rh_x)_2Si_2$ (x = 0.00 and 0.02) with the magnetic field parallel to the c axis and the current parallel to the a axis in the low-temperature region.*

8.3 Analysis and discussion

8.3.1 Electrical resistivity

The temperature dependence of the electrical resistivity of URu_2Si_2 below T_N has been fitted to a T^2 Fermi-liquid term plus an electron spin-wave scattering term which is considered to be applicable for an energy-gap (Δ) antiferromagnet. This formula is expressed as follows [8, 9, 10].

$$\rho(T) = \rho_0 + AT^2 + bT\left(1 + 2\frac{T}{\Delta}\right)\exp\left(-\frac{\Delta}{T}\right). \tag{8.1}$$

The temperature dependence just above T_N has been fitted to a T^2 Fermi-liquid term expressed as follows [8].

$$\rho(T) = \rho_0 + AT^2. \tag{8.2}$$

The spin-wave gap is considered to be obtained from the fitting of Eq. 8.1 to the electrical-resistivity data of the Rh-doped system $U(Ru_{1-x}Rh_x)_2Si_2$. However, the experimental results can not be fitted by Eq. 8.1 below T_N. Just above T_N, the electrical resistivity of $U(Ru_{1-x}Rh_x)_2Si_2$ (x = 0.02 and 0.03) is fitted by using Eq. 8.2. The fitting results to the data of x = 0.02 and 0.03 are shown in Fig. 8.5 and 8.6, respectively. The fitting parameters

	$x = 0.00$	$x = 0.02$	$x = 0.03$
$\rho_{0\ I\parallel a}$ ($\mu\Omega$ cm)		21	23
$A_{I\parallel a}$ ($\mu\Omega$ cm/K^2)	0.35	0.46	0.60
$\rho_{0\ I\parallel c}$ ($\mu\Omega$ cm)		11	13
$A_{I\parallel c}$ ($\mu\Omega$ cm/K^2)	0.126	0.151	0.198

Table 8.3: *Fitting parameters of* $\rho(T) = \rho_0 + AT^2$ *for the electrical resistivities of* $U(Ru_{1-x}Rh_x)_2Si_2$ *(*$x = 0.02$ *and* 0.03*). The fitting parameter for* URu_2Si_2 *are taken from Ref. [8].*

are listed in Table 8.3 together with those of URu_2Si_2 [8]. The value of the coefficient A tends to increase as the Rh concentration increases.

As determined in URu_2Si_2, the phase-transition temperature of $x = 0.02$ is determined to be 13 K where the resistivity shows the minimum. The phase-transition temperature of $x = 0.03$, however, can not be determined from the ρ vs T plot shown in Fig. 8.2. If phase-transition temperature is determined as that where the resistivity deviates from the $\rho_0 + AT^2$ fitting just above T_N, it is estimated to be 8.5 ± 0.5 K from the ρ vs T^2 plot shown in Fig. 8.6. If this estimation is applied to the data of $x = 0.02$, it gives the almost same phase-transition temperature as that determined from the minimum of the resistivity. The detailed phase diagram of $U(Ru_{1-x}Rh_x)_2Si_2$ ($x \leq 0.03$) is obtained from these results and the early study [1] as shown in Fig. 8.7. The anomaly of the resistivity at T_N is weakened as the Rh concentration increases and seems to be disappeared at $x = 0.04 \sim 0.05$.

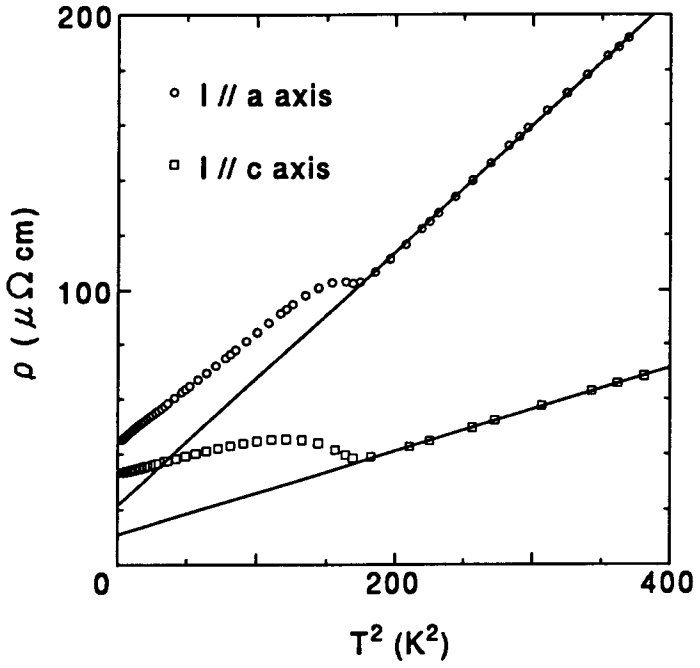

Figure 8.5: *ρ vs T^2 plot of the electrical resistivity of $U(Ru_{0.98}Rh_{0.02})_2Si_2$ with the current parallel to the a and c axes.*

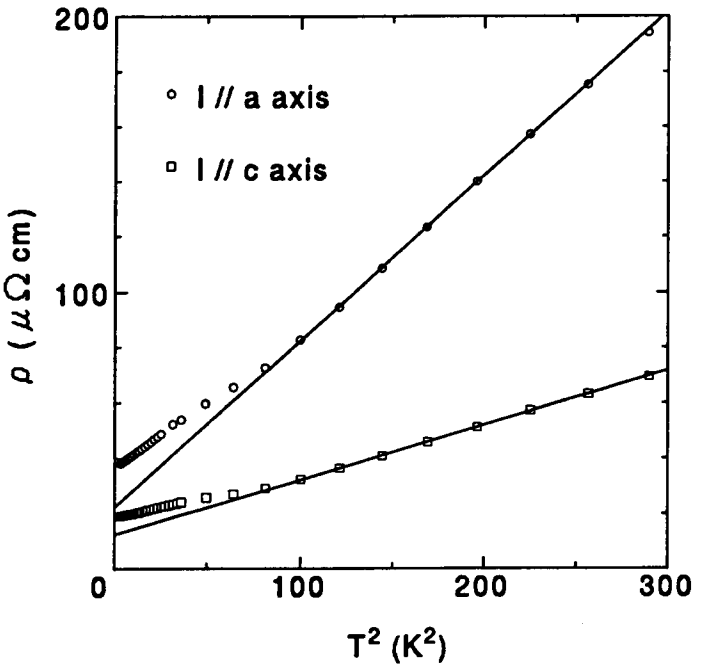

Figure 8.6: *ρ vs T^2 plot of the electrical resistivity of $U(Ru_{0.97}Rh_{0.03})_2Si_2$ with the current parallel to the a and c axes.*

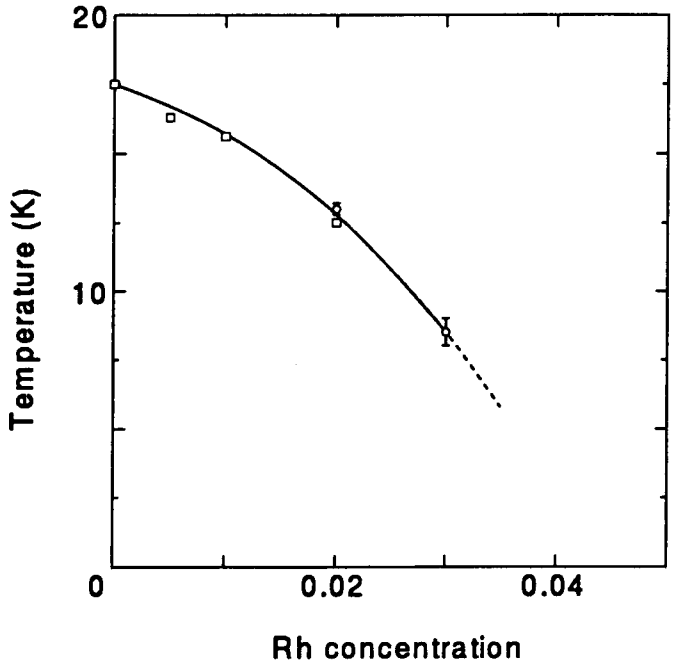

Figure 8.7: *Rh-concentration dependence of the phase-transition temperature T_N. The data of □ are take from Ref. [1].*

8.3.2 Hall effect

The temperature dependence of the Hall coefficient of URu_2Si_2 above T_N has been described mainly by two formulas. One formula is the empirical *ansatz*

$$R_H(T) = R_0 + 4\pi\,\chi(T)\,R_s, \tag{8.3}$$

where R_0 and R_s are the temperature independent ordinary and extraordinary Hall coefficient [11]. Another formula has been derived by Fert and Levy [13] and is expressed as follows [9].

$$R_H(T) = R_0 + \gamma\,\tilde{\chi}(T)\,\rho_m(T), \tag{8.4}$$

where $\tilde{\chi}(T)$ is the reduced susceptibility $\tilde{\chi}(T) = \chi(T)/C_{CW}$ with $C_{CW} = N\mu_{eff}^2/3k_B$, and ρ_m is the magnetic resistivity; *i.e.*, $\rho_m(T) = \rho_{TOT}(T) - \rho_{el-ph}(T) - \rho_0$. γ takes on two different value in two different limit.

$$T \gg T_K \qquad \gamma_1 = -\frac{5}{7} g\mu_B k_B^{-1} \sin\delta_2 \cos\delta_2 \tag{8.5}$$

$$T_{coh} \leq T \leq T_K \qquad \gamma_2 = -\frac{5\pi}{21} g\mu_B k_B^{-1} \frac{\sin(2\delta_3 - \delta_2)\sin\delta_2}{\sin^2\delta_3}. \tag{8.6}$$

The δ_i are the phase shift in the $l = i$ channel where l is the orbital-angular momentum of the conduction electron, T_K is the Kondo temperature, and T_{coh} is the coherent temperature. T_{coh} is approximately equal to T_{max} where the resistivity shows a maximum. The relative

broad maximum of the Hall coefficient of URu_2Si_2 has been qualitatively fitted by Eq. 8.3 and 8.4.

As seen in Fig. 8.3, the relative broad maximum of the Hall coefficient of $U(Ru_{1-x}Rh_x)_2Si_2$ increases and shifts slightly to the lower temperature as the Rh concentration increases. These behavior can be explained qualitatively by using Eq. 8.3 and 8.4, because the broad maximum of the electrical resistivity and magnetic susceptibility of $U(Ru_{1-x}Rh_x)_2Si_2$ ($x \leq 0.03$) increases and shifts slightly to the lower temperature when the Rh concentration increases as shown in Fig. 8.1 and the earlier work [6]. The contribution of the extraordinary Hall effect to the total Hall coefficient is considered to be increased as the Rh concentration increases.

On the other hand, the jump in the Hall coefficient of URu_2Si_2 at T_N has been attributed to a reconstruction of the Fermi surface due to a spin-density wave. The jump in the Hall coefficient has been explained by the change of R_0 in the simple one-band model. More extended analysis about the change of R_0 is tried in this subsection as follows.

The simple one-band model, *i.e.*, $R_0 = 1/nq$, is extended to a generalized multi-band model

$$R_0 = \frac{\sum_i n_i q_i \mu_i^2}{\left(\sum_i n_i q_i \mu_i\right)^2}, \tag{8.7}$$

where n_i, q_i, and μ_i are the concentration, electric charge, and mobility of the carrier in the i-th band, respectively. μ_i is defined as $\mu_i = q_i \tau_i / m_i$, where m_i and τ_i are the effective mass and mean-free time (relaxation time) of the carrier in the i-th band. If the number of the hole and electron conduction band are n and m respectively, Eq. 8.7 is modified as follows.

$$R_0 = \frac{\sum_{k=1}^{n} n_{hk} \mu_{hk}^2 - \sum_{l=1}^{m} n_{el} \mu_{el}^2}{e\left(\sum_{k=1}^{n} n_{hk} \mu_{hk} + \sum_{l=1}^{n} n_{el} \mu_{el}\right)^2}, \tag{8.8}$$

where the lower indices of h and e denote the hole and electron band and e is the electric-charge unit.

R_0 of URu_2Si_2 above T_N has been derived by extrapolating the high-temperature data on the graph of $\chi(T)\,\rho(T)$ versus $R_H(T)$ to $\chi\rho = 0$. It is negative and estimated to be $(-1.18 \pm 0.37) \times 10^{-3}$ cm^3/C [9]. The extraordinary Hall coefficient in Eq. 8.4 is considered to be small compared with R_0 at low temperature, because the term of $\gamma\,\tilde{\chi}(T)\,\rho_m(T)$ decreases as $\rho_m(T)$ decreases in the low-temperature region. Therefore, R_0 of URu_2Si_2 and $U(Ru_{0.98}Rh_{0.02})_2Si_2$ below T_N is assumed to be $R_H(T = 0)$. By fitting a straight line to R_H below T_N, $R_H(T = 0)$ is estimated to be 12.5×10^{-3} and 5.8×10^{-3} cm^3/C from the data of URu_2Si_2 and $U(Ru_{0.97}Rh_{0.03})_2Si_2$, respectively. The obtained result for URu_2Si_2 is almost the same as that in the previous work [9].

R_0 changes the sign from negative to positive at T_N as temperature decreases. The Fermi surface of URu_2Si_2 has been considered to have a gap below T_N due to the nesting of a spin density wave as mentioned in the Introduction. The dramatic change of R_0 may be explained as follows. The typical spin-density-wave antiferromagnetism was observed in chromium (Cr). As mentioned in the review of chromium [14], the SDW at T_N ($\simeq 311$ K) is caused by the nesting of the $3d$ electron and hole bands at the Fermi surface. The

Hall coefficient of Cr, however, does not show a sharp jump at T_N[15] in contrast with that of URu_2Si_2. The small anomaly in the Hall coefficient of Cr at T_N may be understood qualitatively by using Eq. 8.8. The nesting bands with the electron and hole are overlapped each other at the fair part of the Fermi surface. Therefore, these bands may be considered to have almost the same energy-dispersion curve and the same mobility of the carrier as suggested in Ref [14]. If the i-th hole and j-th electron bands occur the nesting at the Fermi surface and these carrier mobility are almost the same, *i.e.*, $\mu_{hi} = \mu_{ej}$, the changes of $n_{hi}\mu_{hi}^2$ and $n_{ej}\mu_{ej}^2$ due to the nesting are considered to be almost the same. As understood from Eq. 8.8, this change does not contribute to a large change of R_0 at T_N. From the experimental data in the Hall coefficient, the comparison between Cr and URu_2Si_2 suggests that the kind of the nesting band is different with each other. The nesting bands of URu_2Si_2 may be suggested as the electron bands, not the electron and hole bands as in Cr, because the sign of R_0 changes from negative to positive.

The nesting condition is very sensitive to the shape of the Fermi surface as reported in Cr [14]. A few percent substitution of vanadium (V) to Cr changes dramatically the Néel temperature. The jump in the Hall coefficient of $U(Ru_{1-x}Rh_x)_2Si_2$ ($x \leq 0.02$) at T_N decrease rapidly as the Rh concentration increases. This experimental result suggests that the 4*d* bands of Ru or Rh contribute the nesting of the Fermi surface.

8.4 Conclusion

We have studied the transport properties of the lattice uranium compound system $U(Ru_{1-x}Rh_x)_2Si_2$ ($x \leq 0.03$). The experimental data of the electrical resistivity show a broad maximum at around 70 K. This broad maximum increases as the Rh concentration increases. The phase transition temperature is determined by using the ρ vs T^2 plot. The anomaly of the resistivity at T_N decreases as the Rh concentration increases and seems to be disappeared at $x = 0.04 \sim 0.05$. The fitting coefficient A of the T^2 term to the resistivity just above T_N increases as the Rh concentration increases. This increase may cause the increase of the broad maximum of the resistivity.

The temperature dependence of the Hall coefficient above T_N and the Rh-concentration dependence of the relative broad maximum of the Hall coefficient are qualitatively understood by the extraordinary Hall coefficient derived by the previous studies. The jump in the Hall coefficient decreases dramatically as the Rh concentration increases. This experimental result suggests that the 4*d* bands of Ru or Rh contribute the nesting of the Fermi surface. The jump in the Hall coefficient is qualitatively understood by the change of the ordinary Hall coefficient. From the comparison of the anomaly of the Hall coefficient between Cr and $U(Ru_{1-x}Rh_x)_2Si_2$ at T_N, it is suggested that the nesting bands of $U(Ru_{1-x}Rh_x)_2Si_2$ are electron bands, not the electron and hole bands as in Cr.

Bibliography

[1] H. Amitsuka, K. Hyomi, T. Nishioka, Y. Miyako, and T. Suzuki, J. Magn. Magn. Mater. **76-77**, 168 (1988).

[2] H. Amitsuka, T. Sakakibara, and Y. Miyako, J. Magn. Magn. Mater. **90-91**, 517 (1990).

[3] Y. Miyako, S. Kawarazaki, H. Amitsuka, C.C. Paulsen, and K. Hasselbach, J. Appl. Phys. **70**, 5791 (1991).

[4] S. Kawarazaki, T. Taniguchi, H. Iwabuchi, Y. Miyako, H. Amitsuka, and T. Sakakibara, Phys. Lett. A **160**, 103 (1991).

[5] Y. Miyako, T. Kuwai, T. Taniguchi, S. Kawarazaki, H. Amitsuka, C.C. Paulsen, and T. Sakakibara, J. Magn. Magn. Mater. **108**, 190 (1992).

[6] Y. Miyako, H. Amitsuka, S. Kawarazaki, T. Taniguchi, and T. Sikama, *Physical Properties of Actinide and Rare Earth Compounds*, JJAP Series 8, (Jpn. J. Appl. Phys., Tokyo, 1993) p. 230.

[7] Y. Miyako, *Transport and Thermal Properties of f-Electron Systems* (Plenum, New York, 1993) p. 187.

[8] T.T.M. Palstra, A.A. Menovsky, and J.A. Mydosh, Phys. Rev. B **33**, 6527 (1986).

[9] A.LeR. Dawson, W.R. Datars, J.D. Garrett, and F.S. Razavi, J. Phys.: Condens. Matter **1**, 6817 (1989).

[10] S.A.M. Mentink, T.E. Mason, S. Süllow, G.J. Nieuwenhuys, A.A. Menovsky, J.A. Mydosh, and J.A.A.J. Perenboom, Phys. Rev. B **53**, R6014 (1996).

[11] J. Schoenes, C. Schönenberger, J.J.M. Franse, and A.A. Menovsky, Phys. Rev. B **35**, 5375 (1987).

[12] Y. Ōnuki, T. Yamazaki, I. Ukon, T. Omi, k. Shibutani, T. Komatsubara, I. Sakamoto, Y. Sugiyama, R. Onodera, K. Yonemitsu, A. Umezawa, W.K. Kwok, G.W. Crabtree, and D.G. Hinks, Physica B **148**, 29 (1987).

[13] A. Fert and P.M. Levy, Phys. Rev. B **36**, 1907 (1987).

[14] E. Fawcett, Rev. Mod. Phys. **60**, 209 (1988).

[15] Y. Furuya, J. Phys. Soc. Jpn. **40**, 490 (1976).

Published works

1. K. Marumoto, T. Takeuchi, T. Taniguchi and Y. Miyako: "Screening of the localized spin of the uranium atom in $LaRu_2Si_2$", Physica B **206-207**, 519 (1995).

2. K. Marumoto, T. Takeuchi, and Y. Miyako: "Kondo screening of uranium in the dilute system $(U_xLa_{1-x})Ru_2Si_2$", Phys. Rev. B **54**, 12 194 (1996).

3. Y. Yamamoto, K. Marumoto, Y. Miyako, K. Nishiyama, and K. Nagamine: "μSR study of the magnetic ordering in $Ce_{1-x}La_xRu_2Si_2$", Hyperfine Interactions **20**, (1996).

4. Y. Miyako, T. Takeuchi, T. Taniguchi, S. Kawarazaki, K. Marumoto, R. Hamada, Y. Yamamoto, M. Ocio, P. Pari, and J. Hammann: "Spin density wave accompanied by anisotropic energy gap opening", J. Phys. Soc. Jpn. **65**, Suppl. B pp. 12 (1996).

5. Y. Miyako, T. Takeuchi, T. Taniguchi, S. Kawarazaki, K. Marumoto, R. Hamada, Y. Yamamoto, M. Sato, Y. Tabata, H. Tanabe, M. Ocio, P. Pari, and J. Hammann: "Spin density wave and heavy electrons in $Ce(Ru_{1-x}Rh_x)_2Si_2$ and $Ce_{1-x}La_xRu_2Si_2$", Physica B, to be published in 1997.

6. K. Marumoto, F. Takayama, and Y. Miyako: "Crystal field splitting of praseodymium in the dilute system $(Pr_xLa_{1-x})Ru_2Si_2$", submitted to J. Magn. Magn. Mater.

7. K. Marumoto, T. Takeuchi, Y. Miyako, M. Ocio, P. Pari, and J. Hammann: "Electrical resistivity of the dilute uranium compound system $(U_xLa_{1-x})Ru_2Si_2$", submitted to J. Magn. Magn. Mater.

Acknowledgments

The author wishes to express his sincere gratitude to Professor Yoshihito Miyako for his valuable suggestions, enlightening discussions, and continuous encouragement during the present work. He would like to thank Professor Shuzo Kawarazaki and Dr. Toshifumi Taniguchi for their advices on this study.

He would like to thank Dr. Tetsuya Takeuchi for his many helpful guidances on the measurements and his many useful discussions on this study.

He would like to thank Professor Koichi Kindo for his guidance to use the high-field magnet system.

He also would like to thank Dr. Hiroshi Amitsuka and Dr. Tomohiko Kuwai for their cooperation in the sample preparation of the dilute uranium compound.

Finally, the author wishes to thank all members of Miyako laboratory.